MID-INFRARED NANOPHOTONICS WITH HYPERBOLIC PHONON POLARITONS

FRANCISCO JAVIER ALFARO MOZAZ

2020

THESIS SUPERVISORS:

RAINER HILLENBRAND

ALEXEY Y. NIKITIN

This PhD thesis has been conducted in CIC NanoGUNE BRTA

by

Francisco Javier Alfaro Mozaz

CONTENTS

List of Abbreviations

AFM	Atomic Force Microscope
FDTD	Finite Difference Time Domain
FEM	Finite Element Method
FT	Fourier Transform
FTIR	Fourier Transform Infrared Spectroscopy
HA	Hole Array
h-BN	hexagonal Boron Nitride
HP	Hyperbolic Polariton
HPhP	Hyperbolic Phonon Polariton
HSM	Hyperbolic Surface Mode
HSP	Hyperbolic Surface Polariton
HVM	Hyperbolic Volume Mode
HVP	Hyperbolic Volume Polariton
LO	Longitudinal Optical
LSP	Localized Surface Polariton
mid-IR	mid-Infrared
MHM	Metal-Hyperbolic material-Metal
OA	Optical Axis
PC	Photonic Crystal
PhP	Phonon Polariton
Q	Quality factor
RPA	Random Phase Approximation
s-SNOM	scattering-type Scanning Near-Field Optical Microscope
SEM	Scanning Electron Microscop
SiO_2	Silicon Dioxide
SPhP	Surface Phonon Polariton

SPP	Surface Plasmon Polariton
TE	Transverse Electric
THz	Terahertz
TM	Transverse Magnetic
TO	Transversal Optical
vdW	van der Waals

Summary

The study of light and its interaction with materials started millennia ago in Egypt and Mesopotamia with the development of the first quartz lenses. Since then, our ever-increasing understanding of the optical phenomena has led to the classic and quantum electrodynamic theories, and to a variety of technological developments that have conceded us an unprecedented control of the flow of light. However, due the diffractive nature of light, squeezing and controlling light in dimensions smaller than the free-space wavelength is a fundamental challenge. Controlling light at the subwavelength scale could help to develop ultra-small and sensitive sensors, small footprint photonic circuits, and enable sub-diffraction-limited optical imaging. In the mid-infrared (mid-IR) spectral region –located at frequencies between 400 and 4000 cm^{-1}– subwavelength optics research could lead to applications in molecular sensing since many biological molecules have distinct absorption spectra at these frequencies. Moreover, mid-IR subwavelength optics could allow a higher control of the thermal emission and absorption of materials, since warm objects (300-1000 K) emit radiation mostly in this spectral range.

Polaritons provide a way of controlling light at the subwavelength scale. Polaritons are electromagnetic modes that arise from the interaction of light with dipolar excitations in a material (such as free carriers in metals, bound charges in polar materials, or electron-hole pairs in semiconductors). A particular type of polariton is a surface polariton, an electromagnetic mode that propagates at the interface between two materials (commonly one with positive and the other with negative permittivity), and which field strength decays exponentially away from the interface. Metals at visible and infrared frequencies have a negative permittivity arising from the coherent oscillations of free carriers (plasmons). Hence, surface plasmon polaritons (SPPs) are supported at metal/dielectric interfaces. Both the wavelength of a SPP and the extension of its evanescent field in the perpendicular direction are shorter than the free-space wavelength, allowing the control of light well below the free-space diffraction limit. Furthermore, a subwavelength-size metallic particle can sustain another type of polariton, a localized surface plasmon polariton (LSP). When resonantly excited, a LSP convert the incident electromagnetic radiation onto strongly enhanced and confined electromagnetic fields. SPPs and LSPs have been intensely studied in metals at visible and infrared frequencies for subwavelength optics applications. However, metals are hampered by the high damping rate of the free electrons, which limit its applicability to subwavelength optics at mid-IR frequencies. A pathway to achieve low-loss

subwavelength optics at mid-IR is the use polar crystals (such as silicon carbide). Polar crystals can exhibit negative permittivity in their Reststrahlen bands (spectral ranges where the reflectivity of a polar crystal is very high), located at mid-IR and THz frequencies, where light couples to lattice vibrations (phonons) forming phonon polaritons. The damping rate of phonons in polar crystals can be smaller than that of free electrons in a metal by up to one order of magnitude, suggesting that surface phonon polaritons can exhibit superior characteristics than surface plasmon polaritons in the mid-IR. Harnessing surface and localized phonon polaritons thus promises infrared radiation localization, routing and manipulation at subwavelength scales with small losses.

The recent emergence of van der Waals (vdW) materials has greatly expanded the library of materials sustaining polaritons. Due to the variation of material types, different polaritonic modes in vdW materials have been discovered, such as plasmon polaritons in graphene (at mid-IR and THz frequencies), exciton polaritons in molybdenum diselenide (at visible and near-IR wavelengths), and phonon polaritons in hexagonal boron nitride (at mid-IR frequencies). van der Waals materials are characterized by an anisotropic crystalline structure, consisting of strong in-plane covalent bonds and weak out-of-plane van der Waals forces. As a consequence, vdW materials can be easily exfoliated into thin films, facilitating the fabrication of high-quality nanostructures. Moreover, the anisotropic bonding can cause an anisotropic polaritonic response, leading to elliptical, hyperbolic or biaxial polaritonic dispersion.

Hexagonal boron nitride (h-BN) has recently emerged as a particularly interesting vdW material for mid-IR nanophotonics. h-BN is a polar crystal that sustains phonon polaritons in its two Reststrahlen bands in the mid-IR. In these bands, due to its anisotropic crystal structure, only one of the components of its uniaxial permittivity tensor has a negative sign. As a consequence, the propagation of light through h-BN is in the form of hyperbolic phonon polaritons. Its isofrequency surface, $\boldsymbol{k}(\omega_0)$, forms a hyperboloid in reciprocal space, allowing short-wavelength and highly-directional polariton propagation. Moreover, the hyperbolic phonon polaritons sustained by h-BN are long lived (with lifetimes up to more than one picosecond), higher than the typical lifetime of plasmon polaritons in metals.

Hyperbolic phonon polaritons in h-BN thin films have been explored theoretically and experimentally. Also, LSP resonances in h-BN nanocones have been reported. However, many particularly interesting nanostructures made of h-BN have not been investigated. In this thesis we study two fundamental nanophotonic

structures made of h-BN, namely, nanorod antennas and polaritonic crystals. Nanorod antennas can be pictured as a truncated polaritonic waveguides that are resonant when the polaritonic mode fulfills the Fabry-Pèrot condition. We employ this picture in the analysis of h-BN nanorod antennas sustaining hyperbolic phonon polaritons. A polaritonic crystal, analogous to a photonic crystal, is a periodically patterned structure made of a material that support polaritons, where the period of the pattern is similar to the polariton wavelength. We study a two-dimensional polaritonic crystal fabricated of a thin h-BN slab, in which the relevant polaritonic mode is a hyperbolic phonon polariton confined to the thin film.

Chapter 1 provides an introduction aimed to contextualize the results presented later on in this thesis. First, we describe some of the materials commonly used for nanophotonics, noble metals and polar crystals, highlighting the characteristics of its surface polaritons in different frequency ranges, particularly in the mid-IR frequency range. We then introduce novel vdW materials (*e.g.* graphene and h-BN), which sustain long-lived and short-wavelength polaritons in the mid-IR frequency range. The last part of the chapter introduces optical antennas and polaritonic crystals based on conventional –isotropic– materials, which sustain localized and surface polariton resonances, respectively.

In Chapter 2 we examine the characteristics of hyperbolic polaritons in h-BN, which behave differently from polaritons in isotropic materials. In particular, we study Hyperbolic Volume Polaritons (HVPs) that propagate through bulk h-BN. We introduce Hyperbolic Surface Polaritons (HSPs), which are confined to h-BN/dielectric interfaces, when the h-BN atomic layers are perpendicular to the interface. Furthermore, we discuss the characteristics of the polaritonic modes sustained by thin h-BN films as well as the modes confined to the edges of h-BN flakes, denominated Hyperbolic Volume Modes (HVMs) and Hyperbolic Surface Modes (HSMs), respectively.

In Chapter 3 we study nanorod antennas made of h-BN. Nanorod antennas are one of the fundamental building blocks in nanophotonics, capable of concentrating light at very small volumes at certain resonant frequencies, these being controlled by the dimensions of the antenna. The h-BN antennas are experimentally studied via infrared nanospectroscopy and infrared nanoimaging. We unveil resonances with high quality factors ($Q \sim 100$) which we assign to Fabry-Pèrot resonances of a hybrid HSM by theoretical analysis. By nanoimaging, an unconventional transverse mode structure is revealed, caused by the hyperbolic character of this hybrid HSM.

Finally, in Chapter 4, we study a basic structure for nanophotonics, a polaritonic crystal. We design and fabricate a two-dimensional hole array made of h-BN, measure it by far-field spectroscopy and nanoimaging and investigate it by numerical and analytical methods. The studied h-BN polaritonic crystal is capable of concentrating light in volumes 10^{-5} times smaller than the free-space wavelength volume, thus being orders of magnitude smaller than conventional photonic crystals. The ultraconfined Bloch modes of the h-BN polaritonic crystal are observed by near-field imaging. The calculated band structure formed by these Bloch modes has a remarkably flat dispersion band. The flat dispersion leads to both angle- and polarization-independent sharp Bragg resonances, as verified by far-field spectroscopy and theoretical modelling.

In conclusion we study nanostructures made of h-BN, exhibiting hyperbolic phonon polaritons with remarkable low losses in the mid-IR. The description and understanding of the properties of these fundamental structures will be of the utmost importance for the design of hyperbolic waveguides, extremely thin mid-IR omnidirectional absorbers and thermal emitters, and nanostructures for phonon-enhanced infrared absorption spectroscopy.

Sumario

El estudio de la luz y su interacción con la materia comenzó hace milenios, en Egipto y Mesopotamia, con la fabricación de las primeras lentes de cuarzo. Desde entonces, nuestra comprensión de los fenómenos ópticos ha llevado al desarrollo de las teorías electrodinámicas clásica y cuántica, así como a una amplia variedad de tecnologías que nos han concedido un control sin precedentes del flujo de la luz. Sin embargo, debido a la naturaleza difractiva de la luz, comprimir y controlar la luz en dimensiones más pequeñas que la longitud de la onda en el vacío (óptica subdifraccional) continúa siendo un complejo desafío. La óptica subdifraccional ayudaría al desarrollo de sensores ultrasensibles y pequeños, circuitos fotónicos miniaturizados, y permitiría realizar imágenes ópticas no limitadas por la difracción de la luz. En el rango del infrarrojo medio, localizado en las frecuencias entre 400 y 4000 cm-1, la investigación en óptica subdifraccional podría ser aplicada a sensores moleculares, dado que muchas biomoléculas tienen espectros de absorción distintivos en estas frecuencias. Además, la óptica subdifraccional en el infrarrojo medio permitiría un mayor control de la emisión térmica y la absorción de los materiales, dado que los objetos "calientes" (a temperaturas entre los 300 y los 1000 K) emiten radiación principalmente en este rango de frecuencias.

Los polaritones proveen de una vía para el control subdifraccional de la luz. Los polaritones son modos electromagnéticos que surgen de la interacción de la luz con excitaciones dipolares en un material (como cargas libres en metales, cargas ligadas en materiales polares, o pares electrón-hueco en semiconductores). Un tipo particular de polaritón es un polaritón de superficie, un modo electromagnético que se propaga en la interfaz entre dos materiales (comúnmente uno con permitividad positiva y otro con permitividad negativa), y cuyo campo electromagnético decae exponencialmente en dirección perpendicular a la interfaz. En el rango visible e infrarrojo, los metales poseen permitividad negativa, originada por la oscilación coherente de las cargas libres en el metal (llamadas plasmones). Como consecuencia, los plasmón-polaritones de superficie (SPPs) se propagan en interfaces entre metales y dieléctricos. La longitud de onda de un SPP y la extensión de su campo electromagnético en la dirección perpendicular a la interfaz son menores que la longitud de onda en el vacío. Además, una partícula metálica de dimensiones menores que la longitud de onda exhibe otro tipo de polaritones, plasmón-polaritones localizados (LSPs). Cuando es excitado resonantemente, un LSP convierte la radiación electromagnética incidente en intensos campos electromagnéticos confinados alrededor de la partícula. Los SPPs

y LSPs han sido intensamente estudiados en metales a frecuencias en el rango visible e infrarrojo, para aplicaciones en óptica subdifraccional. Sin embargo, los metales están limitados por el gran coeficiente de amortiguación de los electrones libres, que restringe su aplicación en óptica subdifraccional en el infrarrojo medio. Una manera de lograr óptica subdifraccional en el infrarrojo medio es el uso de cristales polares (como el carburo de silicio). Los cristales polares pueden poseer permitividad negativa en sus bandas *Reststrahlen* (regiones del espectro electromagnético donde la reflectividad del material polar es muy alta), donde la luz puede acoplarse con vibraciones de la red cristalina (fonones) formando fonón-polaritones. El coeficiente de amortiguación de los fonones en un cristal polar puede ser hasta dos órdenes de magnitud menor que el de electrones en metales, lo que sugiere que los fonón-polaritones de superficie pueden exhibir mejores características que los plasmón-polaritones de superficie en el infrarrojo medio. El uso fonón-polaritones (de superficie y localizados) es una prometedora vía para localizar, canalizar y manipular luz en el infrarrojo medio en escalas subdifracionales con pocas pérdidas.

Recientemente, la aparición de los materiales de van der Waals (vdW) ha expandido enormemente la librería de materiales que exhiben polaritones. Debido a la gran variedad de materiales vdW descubiertos, distintos polaritones han sido descubiertos, plasmón-polaritones en grafeno (en frecuencias de terahercios y en el infrarrojo), excitón-polaritones en molibdeno de diselenio (en el visible e infrarrojo cercano) y fonón-polaritones en nitruro de boro hexagonal (en el infrarrojo medio). Los materiales vdW se caracterizan por su estructura cristalina anisótropa, consistente en fuertes enlaces covalentes en el plano, y débiles enlaces vdW en la dirección perpendicular a las capas atómicas. Como consecuencia, los materiales vdW pueden ser exfoliados en capas finas de manera sencilla, facilitando la fabricación de nanoestructuras de alta calidad. Además, dado que los enlaces entre átomos son anisótropos, puede aparecer una respuesta polaritónica anisótropa, llevando a dispersiones polaritónicas elípticas, hiperbólicas o biaxiales.

El nitruro de boro hexagonal (h-BN) es un material especialmente interesante en óptica subdifracional en el infrarrojo medio. h-BN es un cristal polar que exhibe fonón-polaritones en sus dos bandas Reststrahlen en el infrarrojo medio. En estas bandas, debido a su estructura cristalina anisótropa, únicamente una de las componentes del tensor de permitividad (que es uniaxial) posee signo negativo. Como consecuencia, la propagación de luz a en nitruro de boro en forma de fonón-polaritones hiperbólicos. Su superficie de isofrecuencia, $\boldsymbol{k}(\omega_0)$, forma un hiperboloide en el espacio recíproco, permitiendo la propagación direccional de

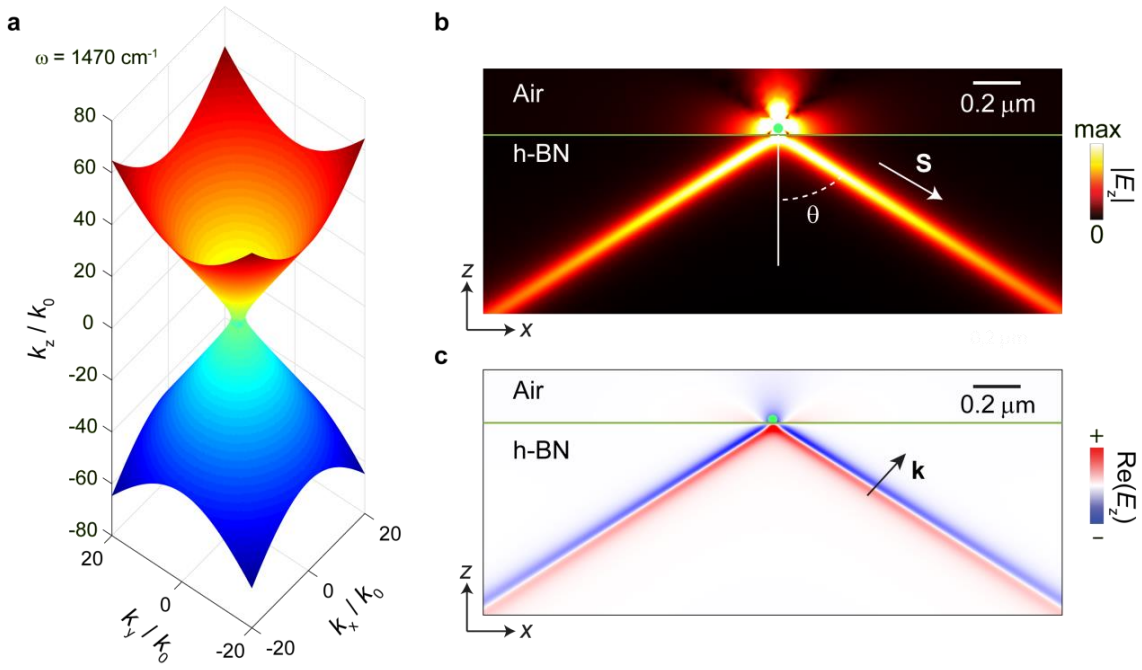

Figura s.1: Fonón-polaritones hiperbólicos de volumen en h-BN. **(a)** Superficie de isofrecuencia de los fonón polaritones hiperbólicos en h-BN, frecuencia $\omega = 1470\, cm^{-1}$. **(b)** Distribución de campo eléctrico inducida por una fuente puntual (dipolo eléctrico, punto verde en (**b**) y **(c)**) localizado en aire sobre un semiespacio de h-BN. El color en la imagen indica el valor absoluto del campo eléctrico vertical como función de x y z. **(c)** similar a **(b)**, donde el color indica $Re(E_z)$. $\theta = 57.4°$.

polaritones con pequeña longitud de onda. Además, los fonón-polaritones hiperbólicos en nitruro de boro presentan vidas medias muy altas (de más de un picosegundo), mayor que las de los plasmón-polaritones en metales.

Los fonón-polaritones en capas finas de h-BN han sido explorados teóricamente y experimentalmente, así como las resonancias localizadas en nanoconos hechos de h-BN.

Sin embargo, varias nanoestructuras básicas basadas en h-BN no han sido estudiadas. En esta tesis estudiamos dos de las nanoestructuras más fundamentales en fotónica: nanoantenas lineales y cristales polaritónicos. Las nanoantenas lineales pueden ser analizadas como guías de onda polaritónicas truncadas, que son resonantes cuando el modo polaritónico cumple la condición de Fabry-Pèrot. Las nanoantennas de h-BN son analizadas usando esta interpretación. Un cristal polaritónico, de manera análoga a un cristal fotónico, es una nanoestructura periódica que soporta polaritones, en la que el periodo del

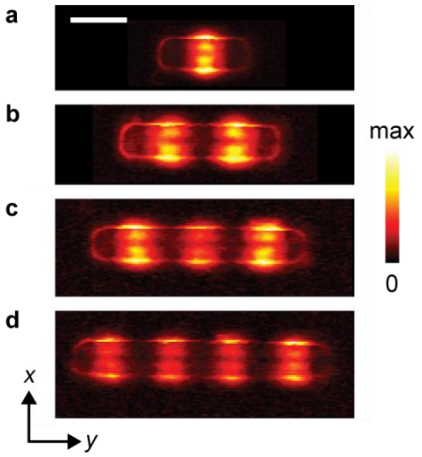

Figura s.2: Imagen infrarroja de campo cercano de antenas lineales de h-BN. Frecuencia de imagen, ω = 1,432 cm^{-1}. La anchura y altura de las nanoantenas es 230 nm and 64 nm, respectivamente. La longitud de cada nanoantena es **(a)** L = 746 nm. **(b)** L = 1.327 nm. **(c)** L = 1.713 nm. **(d)** L = 2.210 nm. Barra de escala, 500 nm

patrón es similar a la longitud de onda del polaritón. Estudiamos un cristal polaritónico bidimensional fabricado a partir de una capa fina de h-BN, cuyo modo polaritónico más relevante es un fonón-polariton hiperbólico confinado en la capa fina.

El Capítulo 1 consiste en una introducción que contextualiza los resultados presentados en esta tesis. Primero, describimos los materiales usados comúnmente en nanofotónica, metales nobles y cristales polares, destacando las características de sus polaritones de superficie en distintos rangos de frecuencias, particularmente en el infrarrojo medio. Después introducimos varios novedosos materiales vdW (*e.g.* grafeno y nitruro de boro), que poseen polaritones en el infrarrojo medio con longitudes de onda pequeñas y largas vidas medias. En la última parte del capítulo introducimos antenas ópticas y cristales polaritónicos basados en materiales convencionales (isótropos), que exhiben, respectivamente, resonancias polaritónicas localizadas y de superficie.

En el Capítulo 2 examinamos las características de los polaritones hiperbólicos en h-BN, cuyo comportamiento es muy diferente al de sus contrapartidas en materiales isótropos. En particular estudiamos polaritones hiperbólicos de volumen (HVPs) que se propagan a través de nitruro de boro (Figura s.1). Introducimos los polaritones hiperbólicos de superficie (HSPs), que están confinados a la interfaz entre h-BN y un material dieléctrico, cuando las capas

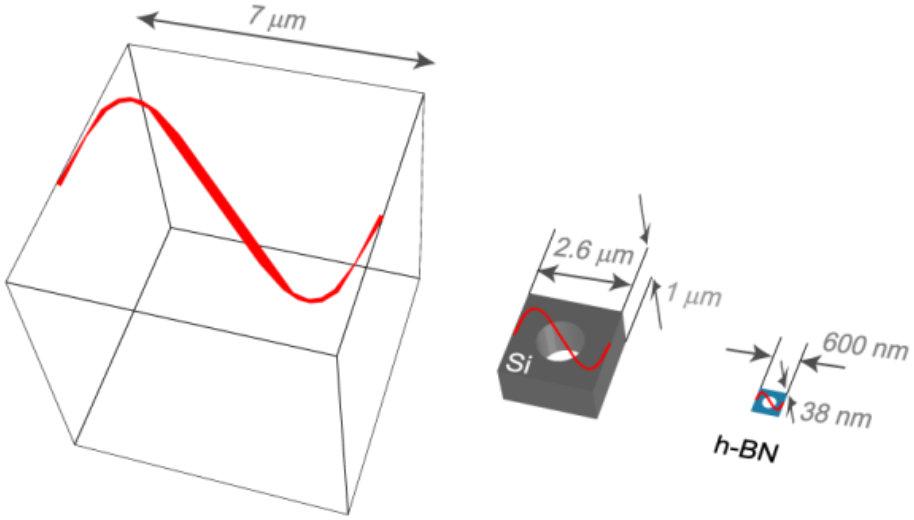

Figura s.3: Comparación del tamaño de celdas unidad. De izquierda a derecha: cubo cuyo lado corresponde a la longitud de onda de la luz en el vacío; tamaño típico de la celda unidad de un cristal fotónico de Silicio; dimensiones de la celda unidad del cristal polaritónico de h-BN estudiado en el Capítulo 4.

atómicas de nitruro de boro son perpendiculares a la interfaz. Además, discutimos las características de los modos polaritónicos que se propagan a través de capas finas de h-BN, así como los modos confinados a los bordes de las láminas de nitruro de boro, denominados modos de volumen hiperbólicos (HVMs) y modos de superficie hiperbólicos (HSMs), respectivamente.

En el Capítulo 3 estudiamos antenas lineales de nitruro de boro. Las antenas lineales son uno de los bloques fundamentales en nanofótonica, dado que pueden concentrar campos electromagnéticos en volúmenes muy pequeños en sus frecuencias de resonancia, las cuales están controladas por las dimensiones de las antenas. Las antenas de h-BN son estudiadas experimentalmente por medio de nanoespectrocopía y nanoimagen infrarroja (Figura s.2). Descubrimos resonancias con altos factores de calidad (Q ~ 100), que asignamos a resonancias de Fabry-Peròt de un modo HSM híbrido.

Finalmente, en el Capítulo 4, estudiamos otra estructura básica en nanofotónica, un cristal polaritónico. Diseñamos y fabricamos una red bidimensional de agujeros en una capa fina de h-BN, que es medida a través de espectroscopía de campo lejano y microscopía de campo cercano, y la investigamos con métodos numéricos y analíticos. Los cristales polaritónicos estudiados permiten concentrar la luz en un volumen 10^{-5} veces más pequeño que el volumen de una longitud de onda en el

espacio libre, varios órdenes de magnitud más pequeño que un cristal fotónico convencional (Figura s.3). Los modos Bloch ultraconfinados del cristal polaritónico son observados con microscopía del campo cercano. La estructura de bandas formada por estos modos Bloch posee una banda marcadamente plana. Esta dispersión plana causa resonancias Bragg espectralmente estrechas, y que son independientes del ángulo y de la polarización de la luz incidente, lo que es verificado por medio de espectroscopía de campo lejano y modelización teórica.

En conclusión, en esta tesis estudiamos nanoestructuras fabricadas a partir de h-BN, un material que exhibe fonón-polaritones hiperbólicos con pocas pérdidas en el infrarrojo medio. La descripción y el análisis de las propiedades de estas estructuras es de gran importancia para el diseño de guías de ondas hiperbólicas, emisores y captadores térmicos extremadamente miniaturizados, y de nanoestructuras para espectroscopia de absorción en el infrarrojo aumentada por fonones.

1. Introduction

In this chapter we briefly introduce surface polaritons in metals, polar crystals and in the van der Waals materials graphene and hexagonal boron nitride, and describe how these materials can confine light at the nanoscale at mid-IR frequencies, thereby overcoming the limitations of traditional dielectric materials. We also introduce optical antennas, which are nanophotonic devices that are capable of localizing optical fields at dimensions below the diffraction limit. Further, 2D polaritonic crystals are introduced, which are periodic structures made of a material sustaining polaritons. Due to the periodicity, the polariton dispersion forms a band structure.

1.1 Guided optical waves in planar structures

2D dielectric waveguides at visible frequencies

The ability to control and manage light at subwavelength scales is crucial for creating miniaturized optical circuits[1], designing novel biosensors[2,3], and to strongly enhance light-matter interactions[4]. However, conventional dielectric materials (typically having small permittivity values), widely used to guide light at visible frequencies, have limitations for localizing light at dimensions smaller than the wavelength of light in the material. In the following subsection we show this limitation in an exemplary system, a two dimensional (2D) slab waveguide.

A 2D slab waveguide made of a dielectric material guides light in the form of waveguide modes. A prototypical dielectric material is silica (SiO_2), commonly used in optical communication systems[5]. The permittivity of silica has a weak dependence on frequency, $\epsilon_{SiO_2} = \epsilon_{SiO_2}(\omega)$, in the visible and near-infrared frequencies[6]. At visible frequencies it can be adequately approximated as $\epsilon_{SiO_2} = 2.28$ (neglecting the very small losses of silica for simplicity). In Figure 1.1 we consider silica waveguides of different thicknesses, and a wavelength $\lambda_0 = 500$ nm, that corresponds to a greenish color. Light propagates along the waveguides in the form of waveguide modes[7,8]. These modes can be separated into transverse electric (TE) modes and transverse magnetic (TM) modes. In the case of the TE (TM) modes, their electric (magnetic) field is perpendicular to the propagation

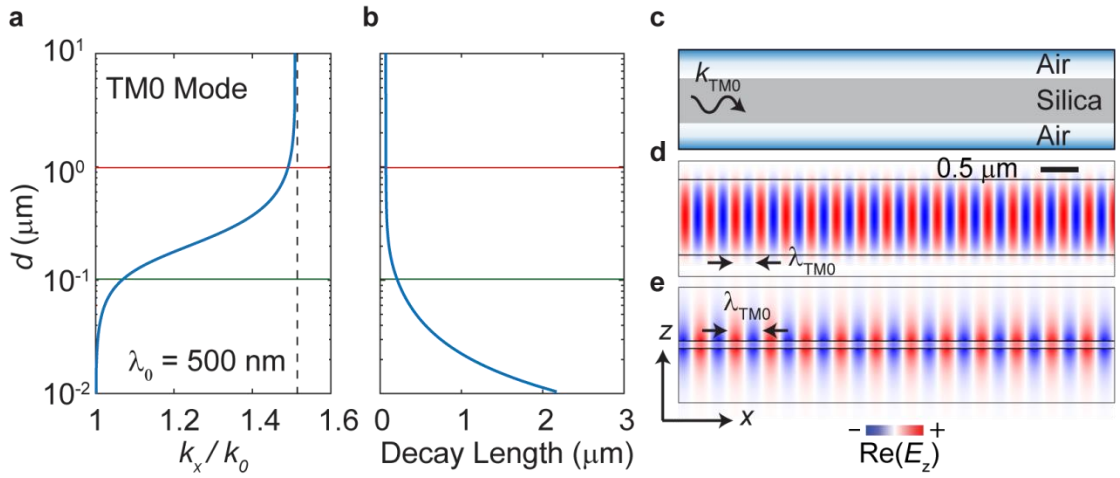

Figure 1.1: TM0 mode of a 2D dielectric waveguide. (a) Normalized wavevector of the TM0 mode as a function of the waveguide thickness. The asymptote at large d, $\sqrt{\epsilon_{SiO2}} \cdot k_0$, is marked by the dashed black line. **(b)** Transverse decay length of the TM0 mode as a function of the waveguide thickness, defined as the length at which the evanescent field strength outside the waveguide decays by a factor $1/e$. **(c)** Sketch of the silica waveguide surrounded by air. **(d)** Snapshot of the vertical component of the electric field, calculated for a waveguide of 1 μm thickness, marked by the solid red line in (a). **(e)** Same as **(d)**, for a waveguide of 0.1 μm thickness, marked by the solid green line in (a). $\lambda_0 = 500$ nm.

direction. Here we analyze the TM modes of the 2D slab waveguide; however, the conclusions are general and applicable to TE modes as well[8,9].

We analytically calculate[10] the normalized wavevector of the TM0 mode, $\frac{k_x}{k_0}$, as a function of the silica thickness, d, for a silica layer surrounded by air (Fig. 1.1). The free-space wavevector magnitude, k_0, is defined as $k_0 = \frac{2\pi}{\lambda_0}$ (with λ_0 the wavelength of light in free-space), and the wavevector of the TM0 mode in the propagation direction, k_x, is defined as $k_x = \frac{2\pi}{\lambda_{TM0}}$ (with λ_{TM0} the wavelength of the TM0 mode). For very small thicknesses, the normalized wavevector is close to one, and it increases as the thickness of the silica layer increases. For thicknesses larger than the wavelength of light in free-space, the TM0 mode wavevector tends to $\sqrt{\epsilon_{SiO_2}} \cdot k_0$, which corresponds to the wavevector of light propagating through bulk silica. Thus, the minimum wavelength of the mode is given by the wavelength of light in the material. The transverse confinement of the TM0 mode (in the direction perpendicular to the propagation direction) is analyzed in the following. A rough

estimate of the extension of the TM0 mode in the transverse direction, L_{TM0}, is given by the thickness of the waveguide plus the decay length of the TM0 mode above and below the waveguide (shown in Fig. 1.1b). For waveguides much thicker than the wavelength of light in free space, the decay length is a fraction of λ_0. However, as the waveguide thickness reduces, the decay length increases, being much larger than the free space wavelength for extremely thin waveguides. L_{TM0} is of the order of magnitude of the wavelength of light in free-space for $d \sim \lambda_0$, having a minimum at $d = 190$ nm, where $L_{\mathrm{TM0}} = 0.82\lambda_0$, (corresponding to 1.24 times the wavelength of light in bulk silica). For very thick ($d \gg \lambda_0$) and very thin ($d \ll \lambda_0$) waveguides, L_{TM0} is much larger than λ_0. To illustrate the transverse confinement of the mode (L_{TM0}) and the mode wavevector (k_{x}) as a function of the waveguide thickness, we calculate the field distribution of the TM0 mode propagating along the x-axis for two thicknesses, $d = 1$ μm and 0.1 μm (marked by red and green lines, respectively, in Fig 1.1a). We show a snapshot of the vertical component of the electric field, Re (E_{z}), in Fig. 1.1d and e. We note that due to the absence of losses in the calculation, the waveguide modes propagate without dissipation. For a waveguide of 1 μm thickness, the electric field of the mode is mainly confined inside the silica (Fig. 1.1d), and the fields rapidly decay with distance to the silica/air interface. However, for the thin waveguide ($d = \frac{\lambda_0}{5} =$ 0.1 μm) the electric field of the mode extends significantly into the surrounding medium[11] (Fig. 1.1e), as expected from the calculated transverse decay length shown in Fig. 1.1b. Moreover, the calculation also shows that the mode wavelength is reduced in thicker waveguides (compare Fig. 1.1d and e). The presented analysis illustrates that, in silica (and more generally in any low index dielectric material[5]) the transverse field confinement cannot be much smaller than the mode wavelength.

Surface plasmon polaritons in metals at visible frequencies

Subwavelength-scale light confinement in the visible spectral range is possible using metals. Metals, such as gold, silver, and copper can have a negative permittivity at visible and infrared frequencies[12]. The permittivity function of a metal at visible frequencies depends upon two main facts: (i) conduction electrons in the metal that can freely move through the material, and (ii) interband excitations that take place when the photon energy is higher than the bandgap energy of the metal[13]. The effect of the free electrons leads to a Drude-like permittivity function, whereas the interband excitations lead to additional contributions to the permittivity function (described by the Drude-Sommerfeld model). Here, for simplicity, we consider a metal with a permittivity in the visible

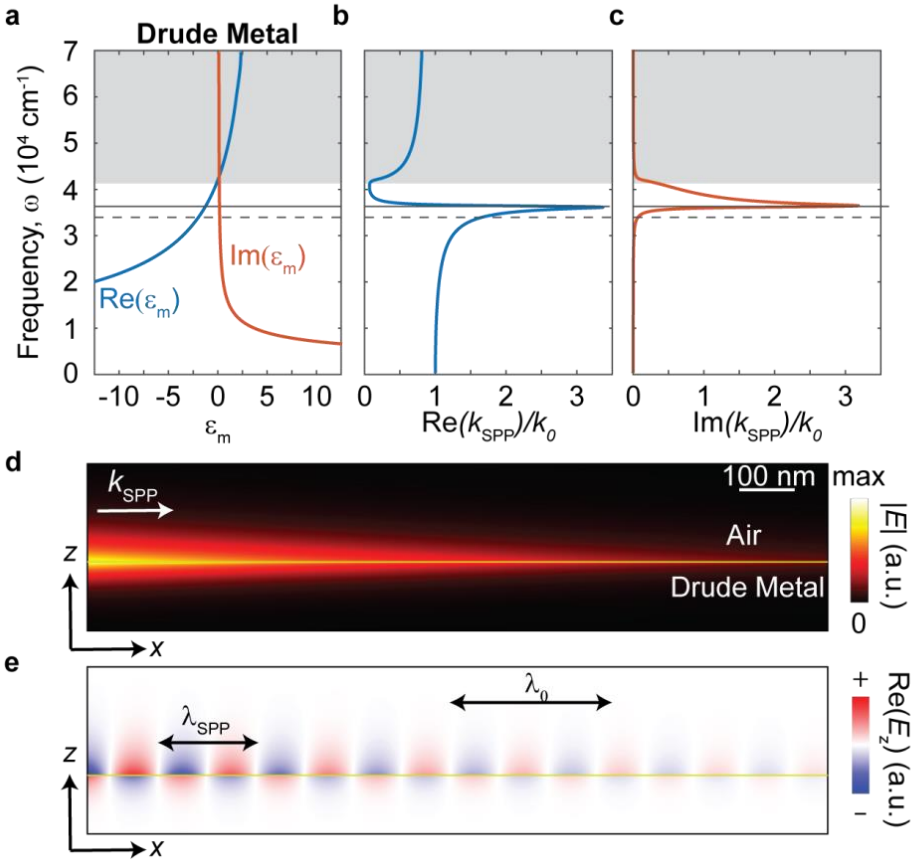

Figure 1.2: Surface plasmon polaritons in the Drude metal/air interface (a) Permittivity of the Drude metal. **(b)** Dispersion of the SPPs in the Drude metal/air interface. **(c)** Field amplitude of the SPP, propagating along the x-direction as a function of x and z. **(d)** Snapshot of the vertical component of the electric field of the SPP. The dashed line in **(a-c)** marks the frequency at which the fields distributions in **(d,e)** were calculated. The white background in (a-c) indicates the region where $\mathrm{Re}(\epsilon_\mathrm{m}) < 0$.

and infrared range described by a modified Drude model. The permittivity of the Drude metal is given by the formula:

$$\epsilon_\mathrm{m}(\omega) = \epsilon_\infty - \frac{\omega_\mathrm{p}^2}{\omega^2 + i\gamma\omega}, \quad (1.1)$$

where ϵ_∞ is the high frequency permittivity, that summarizes the effect of the interband transitions, ω_p is the plasma frequency of the metal, i is the imaginary unit and γ is the damping rate. The parameters we consider to exemplify a Drude metal are: $\epsilon_\infty = 2.95$, $\omega_p = 7.2 \cdot 10^4\ \mathrm{cm}^{-1}$ and $\gamma = 556\ \mathrm{cm}^{-1}$ (or $1.04 \cdot 10^{14}\mathrm{s}^{-1}$),

which describes the permittivity of gold at infrared frequencies. This permittivity function does not correctly describe gold at visible frequencies due to the effect of interband excitations[14,15]. However, the Drude model allows for an intuitive description of the optical properties of metals, and thus hereafter we refer to a metal with the previously described parameters as "Drude metal". The real and imaginary parts of the permittivity of the Drude metal are shown in Fig. 1.2a, illustrating that below a certain frequency (located at the near ultraviolet), the permittivity becomes negative.

An interface between a metal (with negative permittivity) and a dielectric can sustain surface plasmon polaritons (SPPs)[11,16,17], a particular type of polariton which is TM polarized and which propagates along the interface and decays exponentially in the direction perpendicular to the interface. The dispersion relation of SPPs $k_{\mathrm{SPP}}(\omega)$, normalized to the free-space wavevector, k_0 is given by[13]

$$\frac{k_{\mathrm{SPP}}(\omega)}{k_0(\omega)} = \sqrt{\frac{\epsilon_1 \epsilon_{\mathrm{m}}(\omega)}{\epsilon_1 + \epsilon_{\mathrm{m}}(\omega)}}, \qquad (1.2)$$

where ϵ_1 is the permittivity of the dielectric and ϵ_{m} the permittivity of the metal. When a Drude metal/air interface is assumed, the normalized wavevector of SPPs (Fig. 1.2b) is close to one at low frequencies (in the mid-IR and THz range). It increases with frequency up to several times the free-space wavevector of light (near the frequency where $\mathrm{Re}\,[\epsilon_{\mathrm{m}}(\omega)] = -\epsilon_1$, located at near-UV frequencies). At the frequency where $\mathrm{Re}\,[\epsilon_{\mathrm{m}}(\omega)] = -\epsilon_1$ (marked by a solid black line in Figure 1.2a-c) we find a transition from normal to anomalous SPP dispersion. For the latter, the group velocity, given by $v_{\mathrm{g,SPP}} = \frac{\partial k_{\mathrm{SPP}}}{\partial \omega}$, is negative, and the propagation distance is smaller than a wavelength. For frequencies above that of $\mathrm{Re}\,[\epsilon_{\mathrm{m}}(\omega)] = 0$, the SPP continuously transforms into the Brewster mode[13]. The field of the SPP supported by the metal-air interface at $\omega = 3.4 \cdot 10^4\ \mathrm{cm}^{-1}$ (a frequency where the SPP wavevector is significantly increased with respect to the free-space light wavevector) is shown in Figures 1.2d,e. It can be seen that the electric field is maximum at the interface and decays rapidly in the transverse direction (z-direction), with decay lengths L_{d} and L_{m} inside the dielectric and metal, respectively, given by:

$$L_{\mathrm{d}} = \frac{1}{k_0}\,\mathrm{Im}\left(\sqrt{\frac{\epsilon_1 + \epsilon_{\mathrm{m}}}{\epsilon_1^2}}\right), \quad L_{\mathrm{m}} = \frac{1}{k_0}\,\mathrm{Im}\left(\sqrt{\frac{\epsilon_1 + \epsilon_{\mathrm{m}}}{\epsilon_{\mathrm{m}}^2}}\right). \qquad (1.3)$$

For the frequency $\omega = 3.4 \cdot 10^4\ \mathrm{cm}^{-1}$ we obtain $L_\mathrm{d} = 35$ nm and $L_\mathrm{m} = 23$ nm. This calculation shows that the decay length is smaller in the metal than in the dielectric and that both of them are significantly smaller than the free-space wavelength ($\lambda_0 = 294$ nm). This property holds generally for SPPs[13] and is in contrast to waveguide modes in dielectrics (compare to Fig. 1.1).

The electromagnetic field of the SPP decays exponentially as it propagates (as shown in Fig. 1.2d) due to the ohmic losses in the metal, resulting in the heating of the material. For $\omega = 3.4 \cdot 10^4\ \mathrm{cm}^{-1}$, we find a propagation length, given by the formula $L_\mathrm{p} = \frac{1}{\mathrm{Im}(k_\mathrm{SPP})} = 14$ μm, which corresponds to several SPP wavelengths. A propagation length in the range of microns is common for SPPs in metals at visible frequencies[13,18]. Albeit the propagation length of SPPs can be enhanced by using more complicated geometries (up to the milimeter range)[19-22], it stands in stark contrast with the much longer propagation length of visible light in a dielectric waveguide[5,8,23], thus limiting the use of SPPs for long-range communication systems. Hence, SPPs in metals (such as gold, silver and copper) at visible frequencies can have small wavelengths ($\lambda_\mathrm{SPP} < \lambda_0$), high lateral confinement ($L_\mathrm{p} < \lambda_0$ and $L_\mathrm{m} < \lambda_0$), and propagation lengths in the order of dozens of microns.

Surface plasmon polaritons at mid-infrared frequencies

The mid-IR spectral band (400-4000 cm^{-1}) is a technologically important spectral region. For instance, a large number of biological molecules have their vibrational absorption resonances in the mid-IR spectral range. Each molecule possesses a unique absorption spectrum, called "spectral fingerprint", which can be used for molecular identification. For this reason, the mid-infrared region is well-suited for molecular sensing applications; and subwavelength optical devices could allow the direct detection minute quantities of analytes. Moreover, the mid-IR region covers the spectral range at which "warm" objects (300-1000 K)[24] emit thermal radiation (the radiation emitted by any finite-temperature body). Thus, mid-IR radiation is of vital importance for thermal emission control, monitoring and imaging[25]; and subwavelength optical structures could serve as thermal coatings[26-29] and spectrally selective thermal radiators[30,31].

In the mid-IR spectral range, the permittivity of metals (such as gold or silver[12]) has large negative values. As a consequence, SPPs at semi-infinite metal/dielectric interfaces have a wavevector similar to the free-space light wavevector (see Fig. 1.2b,c for the Drude metal), and subsequently large transverse decay lengths in the lateral direction[28,32]. For that reason, they are not suitable for developing subwavelength-scale mid-IR photonics. Nevertheless, there are several pathways

for the subwavelength control of mid-IR radiation. One possibility is to use geometries, different from a metal-dielectric interface, that sustain propagating surface polaritons. One of the most common structures are metal-insulator-metal (MIM) waveguides[33-36], that sustain SPP modes with subwavelength lateral confinement. Beyond MIM waveguides, transmission lines[37,38] and dielectric stripes on metallic surfaces[39] support propagating plasmonic modes with great lateral confinement. The plasmonic mode wavevectors can be significantly larger than k_0[37], with reported values around $3k_0$.

The use of doped semiconductors offers interesting opportunities for mid-IR subwavelength optics. For instance, heavily doped semiconductors with carrier densities around $n = 10^{19-21}$ cm^{-3} (such as Ge, Si, and III-V alloys[40,41]) can have its plasma frequency ω_p (Eq. 1.1) at mid-IR frequencies. As a consequence, the permittivities have small-negative values and thus can support SPPs (at a single interface) with large wavevectors[42] and lateral confinement[40].

The damping rate of free electrons in doped semiconductors, γ, is typically in the order[40,43,44] of $10^{13} - 10^{15} s^{-1}$. The damping rate influence the characteristics of the surface polaritons sustained by a material[45,46]. For instance, lowering the damping rate of a material enhances *e.g.* the lifetime and propagation length of the sustained SPPs. Hence, materials combining smaller damping rates and small negative-valued permittivities could exhibit surface polaritons with better characteristics than SPPs in doped semiconductors at mid-IR frequencies[43,47].

Surface phonon polaritons at mid-IR frequencies

Another type of materials, polar crystals such as SiC[48], GaAs[49] or Al_2O_3[50], can have negative permittivities in the mid-IR spectral range. The negative permittivity arises from the coherent oscillations of the lattice atoms of the polar crystal (optical phonons). The spectral range of negative permittivity is called Reststrahlen band and lies between the transverse optical (TO) phonon frequency and the longitudinal optical (LO) phonon frequency, both frequencies taken in the long phonon wavelength limit[51,52]. The permittivity function of the polar crystal at mid-IR frequencies, $\epsilon_p(\omega)$, can be described by a Lorentz oscillator model[51,53,54],

$$\epsilon_\mathrm{p}(\omega) = \epsilon_\infty \left(1 + \frac{\omega_\mathrm{LO}^2 - \omega_\mathrm{TO}^2}{\omega_\mathrm{TO}^2 - \omega^2 - i\omega\gamma}\right), \quad (1.4)$$

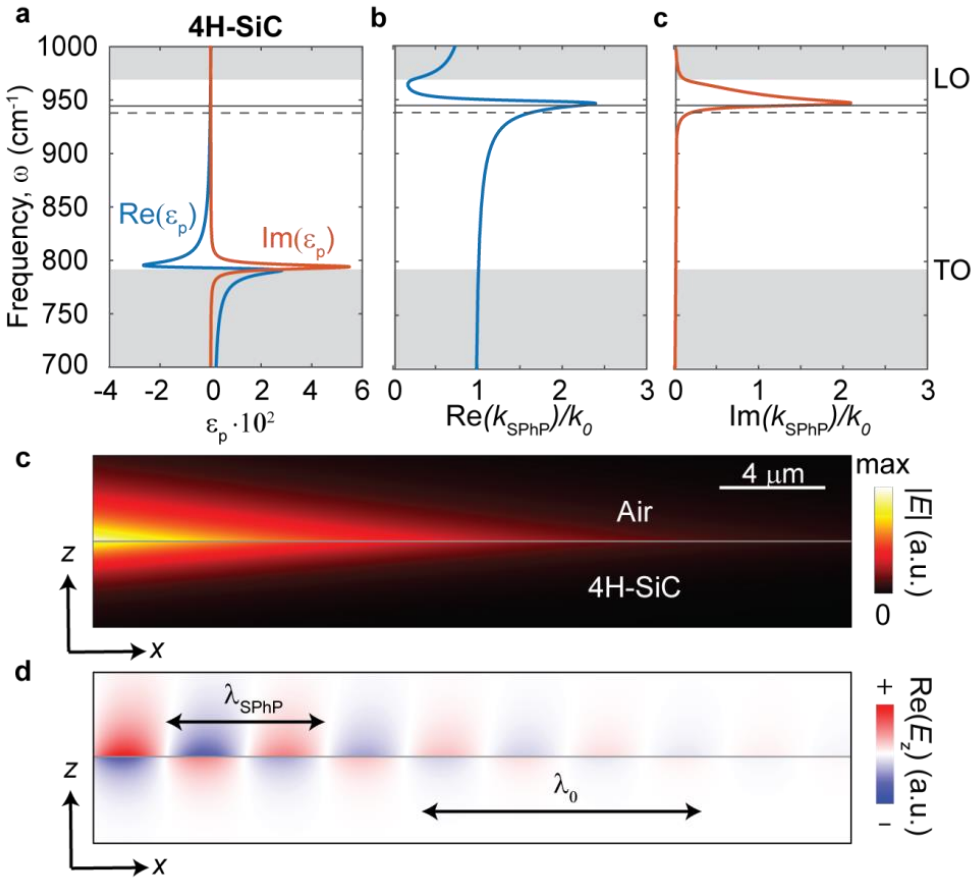

Figure 1.3: Surface Phonon Polaritons in 4H-SiC/Air interface (a) Permittivity of 4H-SiC in its Reststrahlen band in the mid-IR. **(b)** Dispersion of the surface phonon polaritons on a 4H-SiC/air interface. **(c)** Field amplitude of the SPhP as a function of x and z. **(d)** Snapshot of the vertical component of the electric field. The dashed line in **(a-c)** marks the frequency at which the fields in **(d,e)** were calculated. The solid black line in **(a-c)** marks the frequency where $Re(\epsilon_{4H-SiC}) = -1$. The white region in **(a-c)** represent the Reststrahlen band of 4H-SiC.

where ϵ_∞ is the high-frequency permittivity; ω_{LO} and ω_{TO} are the LO and TO phonon frequencies, respectively, i is the imaginary unit, and γ is the damping rate of polar phonons. An attractive feature of polar crystals is the typically small damping rate of polar phonons ($\gamma \sim 10^{12}\ s^{-1}$), up to two orders of magnitude smaller than that of free electrons in metals and doped semiconductors. The reduced damping rate of optical phonons could lead to surface polaritons with lower losses than those of plasmonic materials.

At frequencies inside the Reststrahlen band, surface phonon polaritons (SPhPs) exist. These electromagnetic modes (which are TM polarized) propagate at the interface between a polar crystal and a dielectric with a wavevector that is larger than the free-space photon wavevector. The dispersion relation of the SPhPs, normalized to the free-space wavevector k_0, is given by[13]:

$$\frac{k_{\mathrm{SPhP}}(\omega)}{k_0(\omega)} = \sqrt{\frac{\epsilon_1 \epsilon_{\mathrm{p}}(\omega)}{\epsilon_1 + \epsilon_{\mathrm{p}}(\omega)}}, \qquad (1.5)$$

where ϵ_1 is the permittivity of the dielectric and $\epsilon_{\mathrm{p}}(\omega)$ the permittivity of the polar crystal.

4H-SiC is a polar crystal that has a Reststrahlen band in the mid-IR[55] that we choose as a representative material. Its permittivity function is well described by the Lorentz permittivity model, Eq. (1.4), with the parameters[56]: $\epsilon_\infty = 6.7$, $\omega_{\mathrm{LO}} = 793\ \mathrm{cm}^{-1}$, $\omega_{\mathrm{TO}} = 969\ \mathrm{cm}^{-1}$, $\gamma = 4.76\ \mathrm{cm}^{-1}$ (or 7 ps.). The permittivity function of 4H-SiC is shown in Fig. 1.3a. The dispersion of SPhPs at the 4H-SiC/air interface, calculated using Eq. (1.5), is shown in Fig. 1.3b,c. The SPhPs exist in the range between the TO phonon, (where the SPhP wavevector is similar to the wavevector of light in free-space), up to the LO phonon frequency. SPhPs can possess wavevectors higher than the free-space wavevector (up to $2.5\mathrm{k}_0$ for 4H-SiC), differently from SPPs in metals at mid-IR frequencies (these having wavevectors close to k_0). Due to the small range of frequencies that the Reststrahlen band of polar crystals typically covers (see Fig. 1.3a for 4H-SiC), the permittivity function of a polar crystal is more dispersive than that of a typical plasmonic material[43,47]. Hence, SPhPs are also more dispersive than SPPs and, as a consequence, the group velocity of SPhPs (defined as $v_{g,\mathrm{SPhP}} = \frac{\partial \omega_{\mathrm{SPhP}}}{\partial k}$) is typically smaller than that of SPPs. The SPhP electromagnetic fields decay exponentially in the lateral direction (similar to the SPP fields) as seen in Fig. 1.3d,e. The SPhP decay lengths into the dielectric and polar material are given by:

$$L_{\mathrm{d}} = \frac{1}{k_0}\,\mathrm{Im}\left(\sqrt{\frac{\epsilon_1 + \epsilon_{\mathrm{p}}}{\epsilon_1^2}}\right), \qquad \text{and} \qquad L_{\mathrm{p}} = \frac{1}{k_0}\,\mathrm{Im}\left(\sqrt{\frac{\epsilon_1 + \epsilon_{\mathrm{p}}}{\epsilon_{\mathrm{p}}^2}}\right), \qquad (1.6)$$

respectively, with $\epsilon_{\mathrm{p}}(\omega)$ being defined in Eq. (1.4). For the frequency $\omega = 940\ \mathrm{cm}^{-1}$ ($\lambda_0 = 10.6\ \mu\mathrm{m}$, where the wavevector of the SPhP is well separated from the free-space wavevector), the SPhP decay length into 4H-SiC is $L_{\mathrm{p}} = 1.36\ \mu m$, and the decay length into air is $L_{\mathrm{d}} = 2.30\ \mu\mathrm{m}$, both being much smaller than λ_0. The

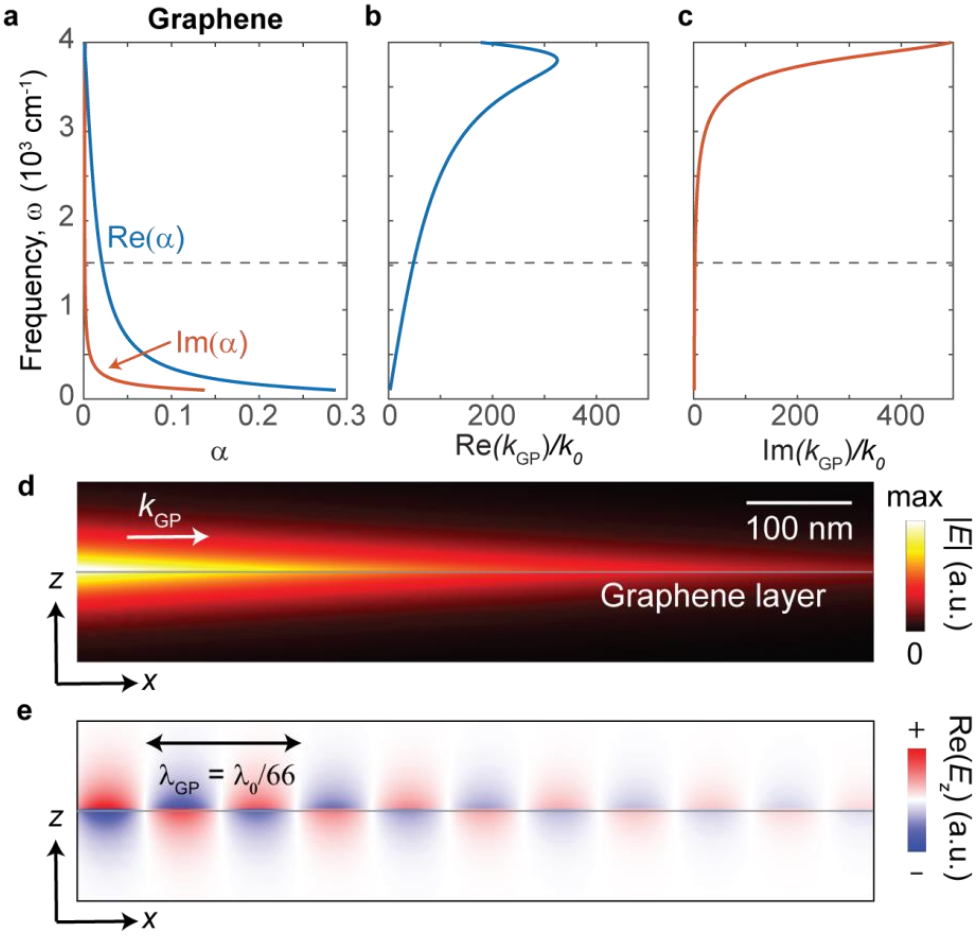

Figure 1.4: Ultraconfined graphene plasmons. (a) Normalized conductivity of graphene at mid-IR frequencies for a Fermi energy of 0.3 eV, a relaxation time of 0.05 ps, and a temperature of 300 K. **(b)** Real part of the normalized wavevector of the GPs. **(c)** Imaginary part of the normalized wavevector of the GPs. **(d)** Field amplitude distribution of a GP. **(e)** Snapshot of the vertical component of the electric field. The dashed line in **(a-c)** marks the frequency at which the fields in **(d,e)** were calculated.

propagation length of the mode at the same frequency is $L_{\text{prop}} = 44$ µm, which is 4.2 times the free-space photon wavelength or 7.9 times the SPhP wavelength. It is worth noting that although the damping rate of polar phonons in 4H-SiC is two orders of magnitude smaller than that of free electrons in doped semiconductors[40], the normalized propagation lengths of SPhPs in 4H-SiC are not much longer than those of SPPs in doped semiconductors[47]. This is related to the fact that the propagation length, L_{prop}, approximately depends on the damping rate, γ, and the group velocity, v_g, as[47] $L_{\text{prop}} \propto \frac{\gamma}{v_g}$.

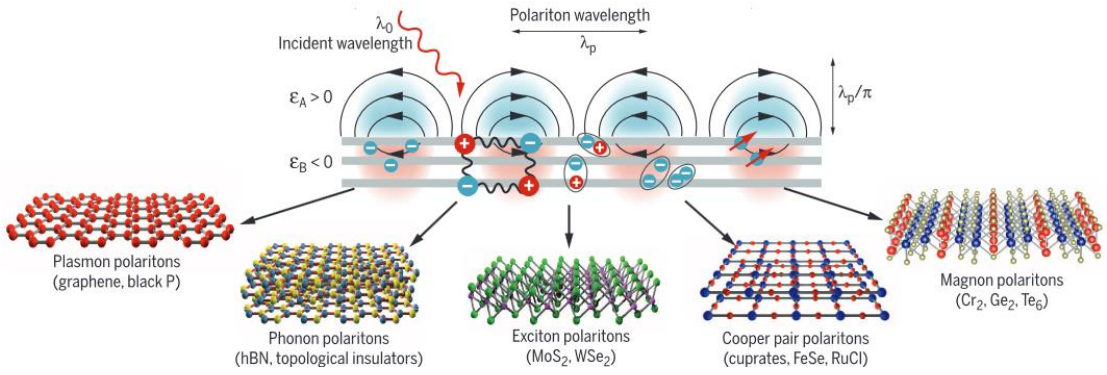

Figure 1.5: Summary of polaritons in vdW materials. Taken from Ref. [57].

Polaritons in vdW materials

Following the isolation of graphene by Geim and Novoselov in 2004[58], a huge research field has emerged, which aims on exploring the properties of atomically thin van der Waals (vdW) materials[59-64]. The initial excitement was caused by the interesting electronic properties of graphene[65] (such as a linear electronic band dispersion and large electron mobilities[66]) promising applications in nanoelectronics[67]. However, it was soon realized that its optical properties were equally interesting[68].

The conductivity of a graphene layer, $\sigma(\omega)$, can be obtained from the Random Phase Approximation[69] (RPA), and depends upon the temperature (T), the chemical potential (μ) and the scattering rate (τ). In the following we discuss the graphene conductivity and the resulting plasmons. The parameters we choose for calculating $\sigma(\omega)$ are similar to those of graphene fabricated by chemical vapor deposition[70]: $T = 300$ K, $\mu = 0.3$ eV, and $\tau = 0.1$ ps. The normalized conductivity, defined as $\alpha(\omega) = \frac{2\pi\sigma(\omega)}{c}$, of graphene at IR and THz frequencies is shown in Fig. 1.4a. Both $\mathrm{Re}(\alpha)$ and $\mathrm{Im}(\alpha)$ are positive and increase with frequency decrease, indicating that the interband contribution to the conductivity dominates in the mid-IR frequency region[69]. Interestingly, in this spectral region electromagnetic waves coupled to the graphene charge carriers (electrons or holes) oscillations exist: graphene plasmon polaritons (GPs)[71-73].

The dispersion relation of GPs (which are TM polarized) in a free-standing graphene layer[74] is given by

$$\frac{k_{GP}(\omega)}{k_0(\omega)} = \sqrt{1 - \frac{1}{\alpha^2(\omega)}}, \qquad (1.7)$$

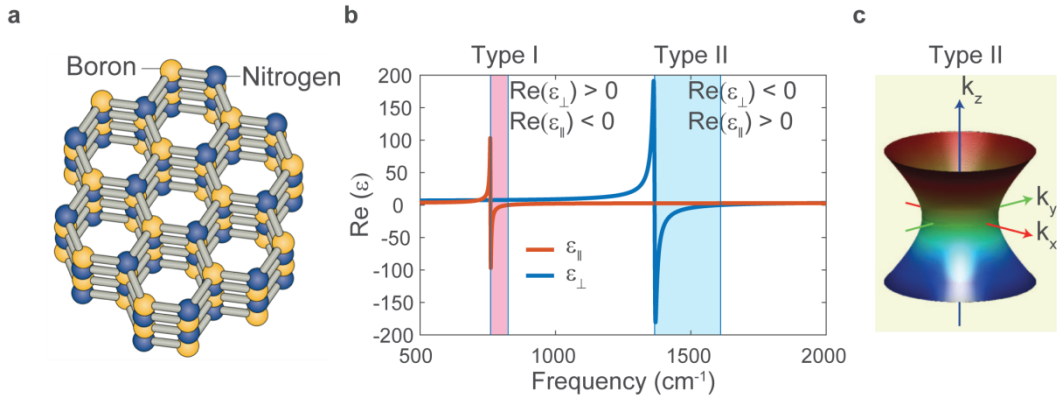

Figure 1.6: Hexagonal boron nitride. (a) Atomic structure of h-BN. **(b)** Permittivity functions of h-BN in the mid-IR spectral range. Red line represents $\mathrm{Re}(\epsilon_{\parallel}(\omega))$ and blue line represents $\mathrm{Re}(\epsilon_{\perp}(\omega))$. Colored spectral regions indicate the upper (red) and lower (blue) Reststrahlen bands. **(c)** Isofrequency surface of SPhP on h-BN in the Type II Reststrahlen band. **(a)** and **(c)** taken from Refs. [75], and [76], respectively.

and shown in Figure 1.4b. A fascinating characteristic of graphene plasmons (GPs) in the mid-IR spectral range is their ultra-small wavelengths (Figs. 1.4b,e), which can be tuned by applying an electrostatic potential[23,24]. The low losses (GPs can propagate several wavelengths[77], as shown in Fig. 1.4e) and exceptional lateral confinement of graphene plasmons (shown in Figs. 1.4d,e), along with its electrical tunability[71,72], has triggered the design of many devices promising biosensing applications[78] and ultrafast electrooptical elements[79].

Following the discovery of graphene, a great number of vdW materials with different physical properties were found. Due to their very different nature (metallic[27-29], semiconducting[30,31], insulating[80] and superconducting[81,82]) a large variety of polaritonic modes have been experimentally observed or theoretically predicted.

A summary of the different types of polaritons in van der Waals materials is shown in Figure 1.5. Conduction electrons coupled with light form plasmon polaritons in graphene[71] and black phosphorous[83,84] among others. The coupling of light with bound atomic charges forms phonon polaritons at mid-IR frequencies in h-BN[80,85] and MoO_3[86,87]. Exciton polaritons, arising from the coupling of light with bounded electron-hole pairs, appear in MoS_2 and WSe_2 at visible and near-IR frequencies[88]. Further, Cooper pair polaritons[89] and magnon polaritons[90] are expected to arise in high-TC superconductors and ferromagnetic materials,

respectively. Importantly, the strongly anisotropic crystal structure of vdW materials (in-plane covalent bonding and out-of-plane weak van der Waals bonding) can cause a highly anisotropic optical response. This optical anisotropy leads to so-called elliptic and hyperbolic polaritonic dispersion, which has been theoretically predicted[84,91,92] and experimentally observed[37,38,93] in many vdW materials.

Hexagonal boron nitride (h-BN) is a particularly interesting vdW material for mid-IR nanophotonics. h-BN is formed by boron and nitrogen atoms bonded covalently in the in-plane direction, forming a hexagonal structure (Figure 1.6a). Since the difference in electronegativity between boron and nitrogen is larger than 0.4 eV[94,95], the B–N bond is polar covalent. The adjacent sheets are bonded by weak van der Waals forces, as in the case of graphite[96]. Owing to the highly anisotropic crystalline structure of h-BN, the frequencies of the in-plane and out-of-plane normal lattice vibrational modes (optical phonons) are different. As a consequence, h-BN is an optically uniaxial material, with the optical axis perpendicular to the covalently bonded B-N layer (defined as parallel to the z-direction). The h-BN permittivity is then described by a diagonal tensor of components $\hat{\epsilon} = \mathrm{diag}(\epsilon_{xx}, \epsilon_{yy}, \epsilon_{zz})$, where $\epsilon_{xx} = \epsilon_{yy} = \epsilon_{\perp}$ and $\epsilon_{zz} = \epsilon_{\parallel}$.

Each of the permittivity tensor components can be described by a Lorentz oscillator model[80,85,97]:

$$\epsilon_j(\omega) = \epsilon_{\infty,j}\left(1 + \frac{\omega_{\mathrm{LO},j}^2 - \omega_{\mathrm{TO},j}^2}{\omega_{\mathrm{TO},j}^2 - \omega^2 - i\omega\gamma_j}\right), \quad (1.8)$$

with $j = \parallel, \perp$. The parameters are $\epsilon_{\infty,\parallel} = 2.95\ \mathrm{cm}^{-1}$, $\omega_{\mathrm{LO},\parallel} = 760\ \mathrm{cm}^{-1}$, $\omega_{\mathrm{TO},\parallel} = 825\ \mathrm{cm}^{-1}$, $\gamma_{\parallel} = 2\ \mathrm{cm}^{-1}$. $\epsilon_{\infty,\perp} = 4.9\ \mathrm{cm}^{-1}$, $\omega_{\mathrm{LO},\perp} = 1360\ \mathrm{cm}^{-1}$, $\omega_{\mathrm{TO},\perp} = 1610\ \mathrm{cm}^{-1}$, and $\gamma_{\perp} = 7\ \mathrm{cm}^{-1}$ (taken from Ref. 97). The h-BN permittivity functions, $\epsilon_{\parallel}(\omega)$ and $\epsilon_{\perp}(\omega)$, at infrared frequencies are shown in Fig. 1.6b. h-BN has two Reststrahlen bands in the mid-IR. These are designated as the *upper* ($\omega = 1360 - 1610\ \mathrm{cm}^{-1}$) and *lower* ($\omega = 760 - 825\ \mathrm{cm}^{-1}$) bands (Fig. 1.6b), originating from the in-plane and out-of-plane optical phonons[85], respectively. Within these bands, phonon polaritons can be supported. However, the sign of the permittivity components is different inside each of the two Reststrahlen bands, $\mathrm{Re}(\epsilon_{\parallel}) \cdot \mathrm{Re}(\epsilon_{\perp}) < 0$. For that reason, light can propagate through bulk h-BN within its Reststrahlen band.

Light propagating inside h-BN at frequencies within its Reststrahlen bands exhibit

peculiar characteristics. For example, the surface formed by the PhPs wavevectors in reciprocal space at a given frequency (called isofrequency surface[98]) forms a hyperboloid, as shown in Fig. 1.6c. This stands in stark difference to light propagating through an isotropic material, where the magnitude of the wavevector the same for all directions (the isofrequency surface being a sphere[10]). Due to its peculiar characteristics, the propagation of light through h-BN is studied in more detail in Chapter 2.

1.2 Optical Antennas

In analogy to its radiofrequency and microwave counterparts, an optical antenna[99] is a "device designed to convert free space propagating optical radiation to localized energy and vice versa". Optical antennas provide a unique opportunity for achieving enormous field enhancements, strong field localization and large absorption. Due to these characteristics, optical antennas find applications in high-resolution microscopy[100], light[101] and thermal[30] emission, coherent control of light[102], photovoltaics[53,54] and photocatalysis[103] among many others.

A small metallic sphere of radius R (with $R \ll \lambda_0$) can act as an optical antenna. Its polarizability, α_p, calculated in the quasistatic limit[13], is given by:

$$\alpha_\mathrm{p} = 4\pi R^3 \frac{\epsilon_\mathrm{m}(\omega) - \epsilon_\mathrm{d}}{\epsilon_\mathrm{m}(\omega) + 2\epsilon_\mathrm{d}}, \quad (1.9)$$

where $\epsilon_\mathrm{m}(\omega)$ is the permittivity function of the metal, and ϵ_d the permittivity of the surrounding medium. At the frequency where the condition $\epsilon_\mathrm{m}(\omega) = -2\epsilon_\mathrm{d}$ is fulfilled, the polarizability diverges, indicating a resonance. This resonance (also called *Fröhlich* resonance[104]) is an example of a *localized surface polariton resonance* (LSR), at which light drives resonantly the conduction electrons (in the case of a metallic sphere) to coherent oscillations.

To identify the nature of this resonance, we show the electric field amplitude around an metallic nanosphere (of $R = 10\,nm$) surrounded by air, when illuminated by a plane wave. The metal permittivity is described by a Drude

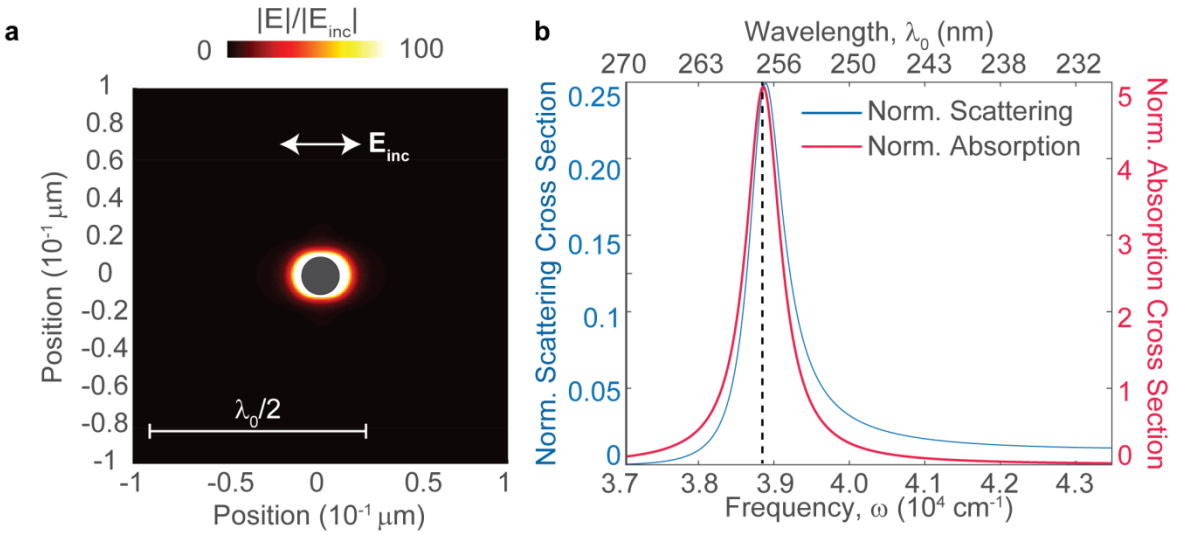

Figure 1.7: Localized surface polariton resonance of a metal nanosphere. (a) Electric field distribution at the LSR of a Drude metal nanosphere. The nanosphere is represented in dark grey. **(b)** Scattering and absorption cross-section normalized to the area of the nanoparticle as a function of the frequency of the incident plane-wave. Dashed line indicates the LSR resonance wavelength.

model (Eq. 1.1), with parameters $\epsilon_\infty = 2.95$, $\omega_p = 7.2 \cdot 10^4\ \mathrm{cm}^{-1}$ and $\gamma = 556\ \mathrm{cm}^{-1}$. At the resonance frequency ($\lambda_\mathrm{R} = 257$ nm), the field is localized near the nanosphere and strongly enhanced (Fig. 1.7a), and the absorption and scattering cross-sections have a maximum[13] (Fig. 1.7b).

Nanorods can also exhibit LSRs[105], thus acting as optical antennas. The longitudinal LSR of a nanorod can be excited by an incident light beam polarized along the longitudinal axis of the nanorod. The frequencies of the LSRs of the nanorod depend on its cross section and length, and on the substrate permittivity[84,85,105], and as a consequence can be tuned over a wide frequency range from the visible to the mid-IR[106,107]. Nanorod antennas play an important role in nanophotonics, being used for surface enhanced infrared absorption spectroscopy applications[107] and to control the angular emission of quantum dots[108,109], among others. In a simple picture, a LSR of the nanorod can be interpreted as a Fabry-Pèrot (FP) resonance of a plasmonic waveguide mode on the nanorod[105,110]. The FP resonance condition is given by

$$n\pi = \phi_1 + \phi_2 + k_\mathrm{m} L, \quad (1.10)$$

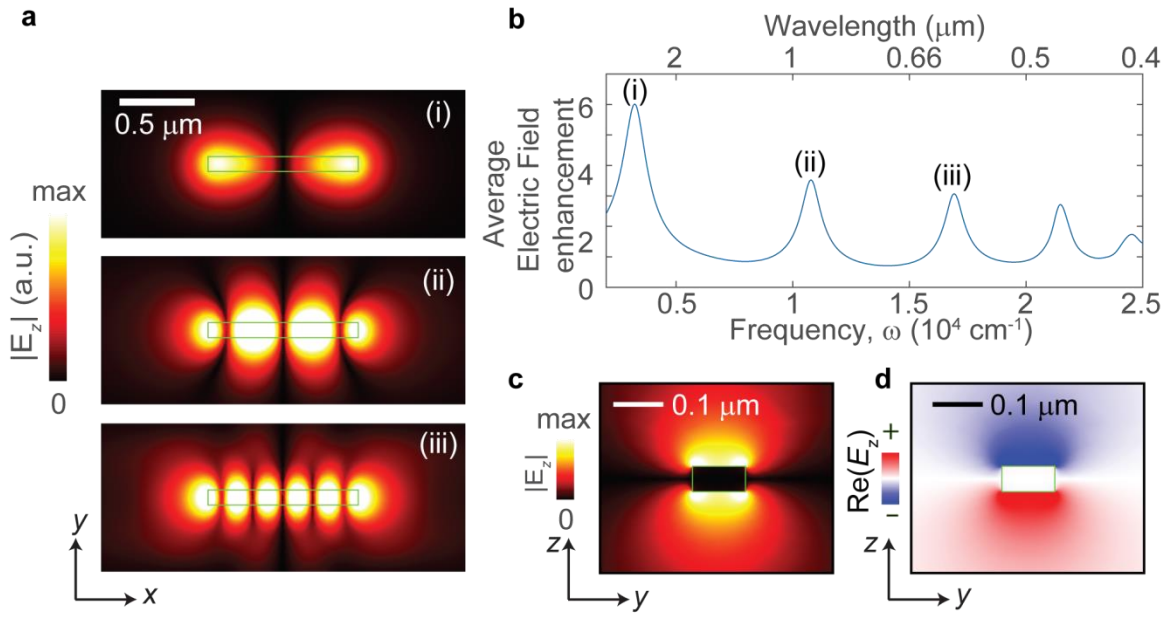

Figure 1.8: Localized resonances in metallic nanorod. (a) Near-field distributions at the resonances, marked as (i), (ii), (iii) in **(b)**, of a nanorod antenna made of a Drude metal. The green line indicates the antenna. **(b)** Calculated average electric field at the nanoantennas surface as a function of the frequency of the incident plane-wave. **(c)** Electric field distribution ($|E_z|$) of the plasmonic waveguide mode. **(d)** Snapshot of the vertical component of the electric field distribution of the plasmonic waveguide mode. **(c,d)** calculated at $\lambda_0 = 0.93$ μm.

where k_m is the wavevector of the plasmonic mode propagating through the nanorod, L is the length of the antenna, ϕ_1 and ϕ_2 are the reflection phases at each end of the nanorod, and n is the order of the FP resonance. Note that, in our study of h-BN antennas (Chapter 3), being h-BN an anisotropic polar crystal supporting phonon-polaritons, we will make use of the same notions of Fabry-Pèrot resonances of a waveguide mode to identify and analyze the modes supported by h-BN nanorod waveguides and antennas.

To analyze the characteristics of LSR in nanorod metallic antennas, we perform full-wave simulations of a micrometer long nanorod antenna of a Drude metal (Eq. 1.1, using the same optical parameters as the metallic nanosphere considered above) illuminated by a plane wave polarized along its longitudinal axis. Fig. 1.8b shows that at certain illuminating frequencies, the electric field around the antenna is greatly enhanced, indicating LSR resonances. At these resonances, the nanorod has large absorption and scattering cross sections[111-113]. Figure 1.8a shows the electric field distribution at each resonance, these having an increasing number of

near-field maxima (along the longitudinal axis) for decreasing illuminating wavelength. Using Eq. (1.10) we identify the peaks denoted as (i), (ii), and (iii), as the first, third and fifth order FP resonances, respectively. The field distribution of the plasmonic waveguide mode giving rise to the FP resonances is also shown in Fig. 1.8c,d. It can be shown that this mode arises from the hybridization of four corner modes propagating along each corner of the rectangular waveguide[21].

1.3 Planar periodic polaritonic structures

A periodic structure made of a material sustaining polaritons holds many similarities with the well-known photonic crystals (PCs) made of positive permittivity materials, that have been subject of intense and widespread research[114]. PCs are based on the interaction between optical waves and a material exhibiting periodicity on the scale of the wavelength of light. Due to the periodicity of the material, the propagation of the optical (bulk) waves within the material is modified. For example, spectral bands where light cannot propagate through the PC may appear under appropriate circumstances –a photonic bandgap[115]. However, one can consider surface, rather than bulk modes. If the surface is made of a material sustaining polaritons, the relevant optical mode will be a surface polariton. The required spatial periodicity can be introduced by *e.g.* corrugating the surface, or spatially changing its optical properties such as the permittivity. As in the bulk case, the periodicity will alter the propagation of surface polaritons.

We show an illustrative example of the effects of introducing a spatial periodicity on a planar system hosting polaritons in the mid-IR. The material we choose is graphene, using the same conductivity parameters as in Section 1.1 (the losses of graphene are reduced by an order of magnitude for simplifying the calculation). The conductivity of graphene is periodically modulated in the x-direction. Resonance perturbation theory[65-67] describes the optical response of modulated conductivity layers and can be applied even to strongly modulated systems such an array of graphene strips, with finite steps in the conductivity[116]. For the considered example, the perturbation consists on a sinusoidal modulation of the conductivity. For a given frequency ω_0,

$$\alpha(\omega_0, x) = \alpha(\omega_0)\,(1 + A \cdot \sin(k_l x)), \quad (1.11)$$

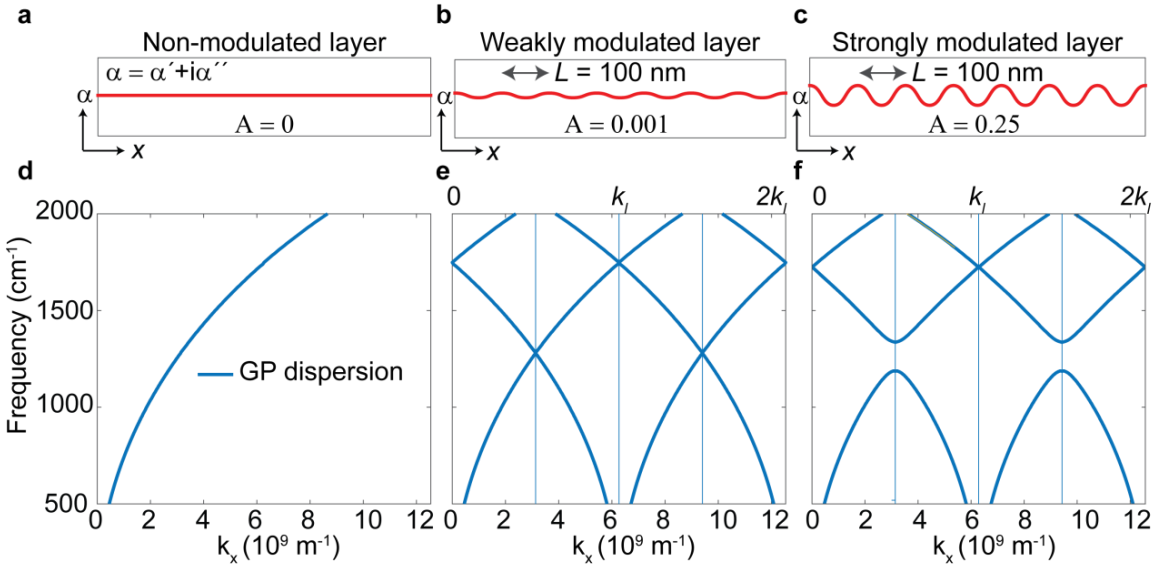

Figure 1.9: Band structure formation in a modulated conductivity layer of graphene. (a) Profile of the conductivity in non-modulated graphene. **(b)** Profile of the conductivity in the weakly modulated graphene. **(c)** Profile of the conductivity in the strongly modulated graphene. **(d)** Graphene plasmon dispersion in the unmodulated conductivity layer. **(e)** Folded GP dispersion of the weakly modulated conductivity layer. **(f)** Polaritonic band structure of a strongly modulated conductivity layer.

where $\alpha(\omega_0)$ is the conductivity calculated from the RPA, A is the strength of the modulation, and k_l the reciprocal wavevector, defined as $k_l = \frac{2\pi}{L}$, where L is the periodicity. We set the periodicity of the modulation to $L = 100\,nm$, the same order of magnitude as the graphene plasmon wavelength at mid-IR frequencies.

A small strength ($A \ll 1$) periodic modulation (Figure 1.9b) create copies of the original polariton dispersion at distances $k_p + k_l$ (with k_p the polariton momenta), without altering the original polariton dispersion (Figure 1.9e, showing the folded polariton dispersion). The modes sustained by the periodic conductivity layer satisfy the Bloch condition[52], and thus are called *polaritonic Bloch modes*. The efficient excitation of a polaritonic Bloch mode by an electromagnetic wave is called a *Bragg resonance*, and generally gives rise to a maximum in the EM wave absorption, transmission or reflection[117]. Upon increasing the strength of the modulation of the conductivity (set to $A = 0.25$ in Fig. 1.9c,f) we observe several effects (Figure 1.9f). First, the GP dispersion deviates from the dispersion of GP in a non-modulated layer. Further, at some crossing points of the original dispersion, band-gaps are opened, prohibiting the propagation of polaritons at those wavelengths (ω = 1180-1335 cm^{-1} in Fig 1.9f).

Polaritonic crystals can be periodic in two dimensions, instead of in one. For two dimensional polaritonic crystals the same notions of polaritonic Bloch modes and Bragg resonances hold to some extent[118]. Nonetheless, the band structure of a 2D polaritonic crystal is richer since the polariton dispersion folding and band structure formation occurs in two dimensions[117,119](*e.g* exhibiting intricate band structures[114], and offering the possibility of opening a complete band-gap for all wavevectors and polarizations[120]). For instance, the studied in Chapter 4 is periodic in two spatial dimensions: a 2D array of holes on an h-BN thin film. The Bloch resonances and Bragg modes of the polaritonic crystal will be theoretically studied by Resonance perturbation theory, and by numerical simulations of the band structure.

2. Surface and Volume modes in h-BN

In this chapter, we analyze the electromagnetic modes sustained by bulk h-BN and thin films of h-BN at frequencies inside its Reststrahlen bands. The knowledge of these modes is of critical importance for the study and design of different h-BN nanostructures, such as the linear antennas and the polaritonic crystals considered in next chapters. We show that light propagates through bulk h-BN in the form of Hyperbolic Volume Polaritons. Then, we demonstrate that a rather different polaritonic mode, which we call Hyperbolic Surface Polariton, can propagate along the h-BN/dielectric interface when the optical axis of h-BN lies along the h-BN-dielectric interface. Thin h-BN films, easily obtained by exfoliation, confine the Hyperbolic Volume (and Surface) Polaritons, that propagate as a discrete set of Hyperbolic Volume (and Surface) Modes. The characteristics of these modes, such as their dispersion, lifetime and propagation length are studied. Some of the results reported in this chapter have been published in "Optical Nanoimaging of Hyperbolic Surface Polaritons at the Edges of van der Waals Materials" by P. Li, I. Dolado et al, Nano Letters 17, 228-235 (2017).

2.1 Introduction

h-BN is an uniaxial polar crystal. In its Reststrahlen bands, located at mid-IR frequencies, the real part of the in-plane and out-of-plane components of the h-BN permittivity tensor have a different sign. As a consequence, the phonon polaritons in h-BN have hyperbolic dispersion (their isofrequency surface is a hyperboloid) and therefore are called hyperbolic polaritons (HPs). Due to their dispersion, HPs show fascinating properties, such as strong directionality and large wavevectors. This chapter is devoted to the study of light propagating through h-BN in the hyperbolic frequency ranges. The results, however, can be also applied to the analysis of HPs in other natural materials[91,92] or hyperbolic metamaterials[98]. The chapter is organized as follows. In Section 2 we analyze the propagation of light through infinite bulk h-BN (when no boundaries are present), where light propagates as hyperbolic volume polaritons (HVPs). In Section 3 we analyze the propagation of HVPs in thin h-BN films with nanometric thickness. We show that in thin films HVPs form discrete hyperbolic volume modes (HVMs). In Section 4 we analyze a different class of polaritons sustained by h-BN: hyperbolic surface

polaritons (HSPs). HSPs are surface waves that exist at the interface between h-BN and a dielectric material, when the optical axis of h-BN is parallel to the interface. Section 5 is devoted to the analysis of the waveguide modes originating from HSPs that propagate along the thin (with a typical thickness around 50 nm) lateral sidewalls of h-BN flakes, named hyperbolic surface modes (HSM).

2.2 Hyperbolic Volume Polaritons in h-BN

In a uniaxial material – with $\hat{\epsilon} = \text{diag}\,(\epsilon_\perp, \epsilon_\perp, \epsilon_\parallel)$ – where the anisotropy is so strong that the sign of the permittivity is different in different directions, $\text{Re}(\epsilon_\perp) \cdot \text{Re}(\epsilon_\parallel) < 0$, light propagates as the so-called hyperbolic volume polaritons (HVPs). These hyperbolic polaritons are the *extraordinary waves*[10] (TM polarized) supported by uniaxial materials, when the in-plane and out-of-plane permittivity tensor components have a different sign. The term *hyperbolic* comes from the shape of the HVPs isofrequency surface in reciprocal (wavevector) space[79,80]. For instance, the isofrequency surface of light in vacuum is given by $k_x^2 + k_y^2 + k_z^2 = \frac{\omega^2}{c^2}$, where ω is the frequency, c is the velocity of light, and $\boldsymbol{k} = (k_x, k_y, k_z)$ is the wavevector. Thus, it forms a sphere, indicating that light propagates isotropically. In contrast, the isofrequency surface of HVPs is given by[10,17]

$$\frac{k_x^2 + k_y^2}{\epsilon_\parallel} + \frac{k_z^2}{\epsilon_\perp} = \frac{\omega}{c} \qquad (2.1)$$

The solutions of Eq. (2.1) (for real $\epsilon_\parallel, \epsilon_\perp$) are open hyperboloids. For complex-valued $\epsilon_\parallel, \epsilon_\perp$ the isofrequency surfaces (that must be defined for the real values of the wavevector components) are more complicated. Nevertheless, assuming $|\text{Re}\,(\epsilon_\parallel)| \gg \text{Im}\,(\epsilon_\parallel)$ and $|\text{Re}\,(\epsilon_\perp)| \gg \text{Im}\,(\epsilon_\perp)$, we will stick to the same classification of the isofrequency surfaces as for purely real-valued $\epsilon_\parallel$, $\epsilon_\perp$.

In each of the Reststrahlen bands, the isofrequency surfaces are topologically different. Namely, when $\text{Re}(\epsilon_\perp) > 0$ and $\text{Re}(\epsilon_\parallel) < 0$ –as in the h-BN lower Reststrahlen band–, the isofrequency surface is a two sheet hyperboloid (Type I). In contrast, when $\text{Re}(\epsilon_\perp) < 0$ and $\text{Re}(\epsilon_\parallel) > 0$, the isofrequency surface is a one sheet hyperboloid (Type II) –as in the h-BN upper Reststrahlen band (Fig. 2.1a)–.

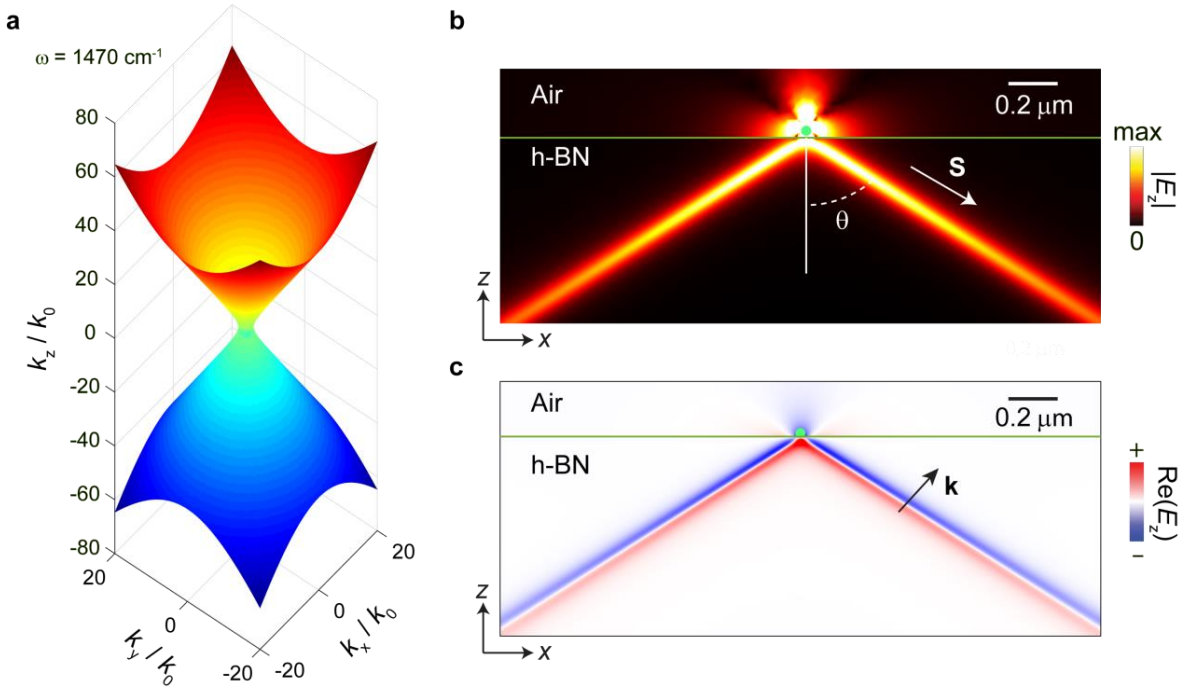

Figure 2.1: Propagation of HVPs through a semi-infinite h-BN crystal. **(a)** Isofrequency surface of HVPs in h-BN at $\omega = 1470\,cm^{-1}$. The dielectric permittivity tensor components are $\epsilon_{\parallel} = 2.75 + i \cdot 4 \cdot 10^{-4}$ and $\epsilon_{\perp} = -6.98 + i \cdot 0.4$. **(b)** Vertically oriented electric dipole source (green dot) over semi-infinite volume of h-BN. The colorplot shows $|E_z|$ as a function of x and z. **(c)** the color plot showing $\mathrm{Re}(E_z)$. $\theta = 57.4°$.

Remarkably, along the direction given by the asymptote of the hyperboloid, HVPs propagate with arbitrarily large wavevectors (and thus vanishing wavelengths). This unique property of hyperbolic polaritons allows channeling and confining light in extremely subwavelength volumes[81,82] and for enhanced dipole-dipole interactions[121], among other effects.

HVPs can be excited in h-BN by localized sources that generate strong near fields with large wavevectors. As an example we calculate the electromagnetic fields induced by a vertically oriented electric dipole located near the surface of a semi-infinite h-BN crystal, for a frequency inside the upper Reststrahlen band of h-BN, $\omega = 1470\ \mathrm{cm}^{-1}$. The isofrequency surface of HVPs is a one sheet hyperboloid as shown in Fig. 2.1a.

The HVPs launched by the dipole form a directional ray-like pattern (hereafter simply referred as hyperbolic ray[122]) inside h-BN, which propagates with a given angle θ with respect to the z-axis (color plot in Fig. 2.1b). The hyperbolic ray is

formed by HVPs with extremely large wavevectors that propagate with an angle given by[107,108] $\theta_{HR} = \arctan\sqrt{-\frac{\epsilon_\perp}{\epsilon_{||}}}$. Interestingly, the hyperbolic ray direction is parallel to the direction of the energy flow (Poynting vector, **S**), as shown in Fig. 2.1b. In contrast, the direction of the phase velocity (coinciding with the direction of the asymptote of the hyperboloid) is nearly perpendicular to the hyperbolic ray (and thus to the Poynting vector), as shown in Fig. 2.1c.

As a final remark, ordinary waves (TE polarized[17]) can also propagate through h-BN crystals in the Type I Reststrahlen band (TE waves can propagate through uniaxial media if the condition $\mathrm{Re}(\epsilon_\perp) > 0$ is fulfilled[17]). However, the wavevector magnitude of the TE waves[17], $|\boldsymbol{k_0}\sqrt{\epsilon_\perp}|$, is small compared to that of the HVPs.

Since hexagonal boron nitride is a vdW material, due to its weak interlayer coupling, thin nanometric slabs of h-BN can be easily exfoliated onto different substrates. This is a crucial advantage for the application of h-BN in nanophotonics, and opens a plethora of opportunities to fabricate nanodevices based on one[123] or multiple layers[124] of different vdW materials. Thus, it is of great interest to analyze the polaritonic modes sustained by thin h-BN films.

2.3 Hyperbolic Volume Modes in thin films

In this section we study the electromagnetic modes (HVMs) sustained by thin h-BN films. We consider films with the faces parallel to the h-BN atomic layers, so that the direction of the optical axis is perpendicular to the surfaces of the film. The HVMs in h-BN are, in principle, analogous to electromagnetic modes in dielectric waveguides[8]. In the first subsection we derive analytically the dispersion of HVMs in a three layer system consisting in a thin film of h-BN surrounded by two semi-infinite dielectric media. In the second subsection we analyze the field distribution, propagation length and lifetime of HVMs for frequencies inside the h-BN Reststrahlen bands.

2.3.1 Analytical derivation

Let us first consider an infinite (non-magnetic) uniaxial medium characterized by a dielectric permittivity tensor $\hat{\epsilon}$. We choose the coordinate system in such a way that the tensor is diagonal

$$\hat{\epsilon} = \begin{pmatrix} \epsilon_\perp & 0 & 0 \\ 0 & \epsilon_\perp & 0 \\ 0 & 0 & \epsilon_\parallel \end{pmatrix}. \qquad (2.2)$$

To mathematically describe the electromagnetic field inside the uniaxial medium, we can decompose it in the appropriate basis (for which we have to find the appropriate basis vectors). We will follow a standard procedure (used in other publications[125,126]), and represent the $\vec{\boldsymbol{E}}$ and $\vec{\boldsymbol{H}}$ fields in the uniaxial medium in the following form

$$\vec{\boldsymbol{E}} = E_0 \vec{\boldsymbol{e}} e^{i\vec{\boldsymbol{k}}\vec{\boldsymbol{r}} - i\omega t}, \qquad \vec{\boldsymbol{H}} = H_0 \vec{\boldsymbol{h}} e^{i\vec{\boldsymbol{k}}\vec{\boldsymbol{r}} - i\omega t}, \quad (2.3)$$

where $\vec{\boldsymbol{e}}$ and $\vec{\boldsymbol{h}}$ are the unknown basis vectors of the electromagnetic field in a uniaxial medium, E_0 and H_0 are the arbitrary field amplitudes, ω is the angular frequency, $\vec{\boldsymbol{k}}$ is the wavevector, and $\vec{\boldsymbol{r}}$ the position vector. Using Maxwell equations, $\vec{\nabla} \times \vec{\boldsymbol{E}} - \frac{1}{c}\frac{\delta \vec{\boldsymbol{B}}}{\delta t} = 0$ and $\vec{\nabla} \times \vec{\boldsymbol{H}} = \frac{1}{c}\frac{\delta \vec{\boldsymbol{D}}}{\delta t}$, we can exclude the magnetic field, and obtain the wave equation for the electric field,

$$\vec{\nabla} \cdot \left(\vec{\nabla} \cdot \vec{\boldsymbol{E}}\right) - \Delta \vec{\boldsymbol{E}} - \frac{\omega^2}{c^2}\left(\hat{\epsilon}\vec{\boldsymbol{E}}\right) = \boldsymbol{0}. \qquad (2.4)$$

Substituting into Eq. (2.4) the fields from (Eq. 2.3) we obtain the homogeneous linear system of equations for the three components of the unknown basis vectors.

$$\mathcal{M}\vec{\boldsymbol{e}} = \begin{pmatrix} \Delta_x & q_x q_y & i q_x q_z \\ q_x q_y & \Delta_y & \pm i q_y q_z \\ i q_x q_z & \pm i q_y q_z & \Delta_z \end{pmatrix} \begin{pmatrix} e_x \\ e_y \\ e_z \end{pmatrix} = 0, \quad (2.5)$$

where $k_0 = \frac{\omega}{c}$ is the free-space wavevector, $q_{x,y} = \frac{k_{x,y}}{k_0}$ are the normalized in-plane components of the wavevector, and q_z is the out-of-plane component of the normalized wavevector, introduced according to $k_z = \pm i q_z k_0$. The $+$ $(-)$ sign

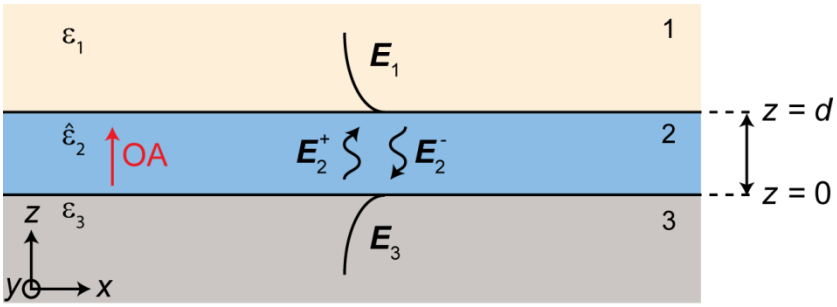

Figure 2.2: Schematics of the three layer system. The regions 1 and 3 are isotropic media of permittivities ϵ_1 and ϵ_3, respectively. Region 2 corresponds to the h-BN film of thickness d, with the optical axis parallel to the z-direction.

corresponds to the wave propagating along (opposite to) the z-axis. Δ_i is defined as

$$\begin{aligned}\Delta_x &= \epsilon_\perp - q_y^2 + q_z^2 \\ \Delta_y &= \epsilon_\perp - q_x^2 + q_z^2 \\ \Delta_z &= \epsilon_\parallel - q_x^2 - q_y^2.\end{aligned} \qquad (2.6)$$

The system in equation (2.5) has non-trivial solutions only when $\det \mathcal{M} = 0$, that gives the well-known Fresnel equation for the uniaxial medium[10,17]

$$q_z^2\left[\epsilon_\parallel(q_z^2+\epsilon_\perp^2) - (q_x^2+q_y^2)\,(\epsilon_\parallel+\epsilon_\perp)\right] + \epsilon_\perp\left(\epsilon_\parallel - q_x^2 - q_y^2\right)\left(\epsilon_\perp - q_x^2 - q_y^2\right) = 0. \qquad (2.7)$$

The Fresnel equation is quadratic equation in terms of the squared z-component of the wavevector, q_z. Its solutions, denoted as q_{ez}, q_{oz} read as

$$q_{o,ez}^2 = \frac{1}{2}\left\{\frac{\epsilon_\perp+\epsilon_\parallel}{\epsilon_\parallel}(q_x^2+q_y^2) - 2\epsilon_\perp\right\} \pm \frac{1}{2}\sqrt{D}. \qquad (2.8)$$

With D being

$$D = \left[2\epsilon_\perp + \frac{\epsilon_\parallel-\epsilon_\perp}{\epsilon_\parallel}(q_x^2-q_y^2)\right]^2 + 4\frac{(\epsilon_\parallel-\epsilon_\perp)^2}{\epsilon_\parallel^2}q_x^2q_y^2\,. \qquad (2.9)$$

The solution for the ordinary, q_{oz}, (extraordinary, q_{ez}) z-component of the wavevector is obtained choosing the plus (minus) sign in Eq. (2.8). Substituting Eq. (2.8) into the system (2.5) we find all the three components of the basis vectors $\vec{\boldsymbol{e}}$. We take into account that the z-components of the wavevectors (2.8) are reduced to the well-known expressions for the ordinary and extraordinary waves:

$$q_{oz}^2 = q^2 - \epsilon_\perp, \qquad q_{ez}^2 = \frac{\epsilon_\perp}{\epsilon_\parallel} q^2 - \epsilon_\perp , \quad (2.10)$$

where $q^2 = q_x^2 + q_y^2$ is the in-plane wavevector. Since Eq. (2.5) is homogeneous, one of the components must be fixed (to be q_z/q for the ordinary wave and q_y/q for the extraordinary wave, respectively). Without loss of generality, the y-component of the basis vector is fixed. The basis vectors are then

$$e_o = \frac{1}{q}\begin{pmatrix} -q_y \\ q_z \\ 0 \end{pmatrix}, \qquad e_e = \frac{1}{q}\begin{pmatrix} -q_x \\ q_y \\ \dfrac{\epsilon_\perp + q_{ez}^2}{\mp i q_{ez}} \end{pmatrix}, \quad (2.11)$$

where the factor $\frac{1}{q}$ stays for the normalization.

Having obtained the basis vectors, we can now derive the dispersion relation of HVM in an h-BN thin film of thickness d and permittivity $\hat{\epsilon} = \mathrm{diag}(\epsilon_\perp, \epsilon_\perp, \epsilon_\parallel)$ occupying the region $0 < z < d$ between two dielectric half-spaces with permittivities ϵ_1 (region "1", $z > d$) and ϵ_3 (region "3", $z > 0$).

First, we represent the electric field in the isotropic regions above and below the h-BN thin film. In these regions we can take the fields in the form of s- and p-polarized plane waves. Given the system is symmetric with respect to rotations around the z-axis, we can consider, without loss of generality, that the y-component of all the electric fields is 0. The p-polarized electric fields in the 1 and 3 regions read as:

$$E_{1,p} = \alpha_1 \frac{1}{q}\begin{pmatrix} q_x \\ 0 \\ \dfrac{q^2}{-i q_{1z}} \end{pmatrix} e^{i k_x x} e^{i k_{1z}(z-d)}, \quad (2.12)$$

$$E_{3,p} = \alpha_3 \frac{1}{q}\begin{pmatrix} q_x \\ 0 \\ \dfrac{q^2}{+i q_{3z}} \end{pmatrix} e^{i k_x x} e^{-i k_{3z} z}, \quad (2.13)$$

where $q_{1,3z} = \sqrt{q_x^2 - \epsilon_{1,3}} > 0$ is the out-of-plane component of the normalized wavevector. $\alpha_{1,3}$ are the unknown amplitudes of the fields. Since HVMs are formed by the extraordinary waves, inside the region 2 we need to consider only the extraordinary basis vector (which is p-polarized). The electric fields inside the h-BN thin film can be represented as

$$E_{2,p} = E_{2,p}^{+} + E_{2,p}^{-} = \left[\alpha_{2^-} \frac{1}{q} \begin{pmatrix} -q_x \\ 0 \\ \epsilon_\perp + q_{ez}^2 \\ \hline +iq_{ez} \end{pmatrix} e^{-ik_{ez}z} + \alpha_{2^+} \frac{1}{q} \begin{pmatrix} -q_x \\ 0 \\ \epsilon_\perp + q_{ez}^2 \\ \hline -iq_{ez} \end{pmatrix} e^{ik_{ez}z} \right] e^{ik_x x}, \quad (2.14)$$

where the basis vector e_e, given by Eq. (2.11), has been simplified taking into account that $q_y = 0$. $\alpha_{2^\pm}$ are the unknown amplitudes of the fields. To find the magnetic fields we use the Maxwell equation $\vec{\nabla} \times \vec{H} = \frac{1}{c}\frac{\delta \vec{D}}{\delta t}$. For a plane wave it reduces to $\vec{H} = \vec{q} \times \vec{E}$. The continuity equations for the electric and magnetic fields are:

$$\begin{matrix} E_{1,p,x}(z=d) = E_{2,p,x}(z=d) & \quad E_{2,p,x}(z=0) = E_{3,p,x}(z=0) \\ B_{1,p,y}(z=d) = B_{2,p,y}(z=d) & \quad B_{2,p,y}(z=0) = B_{3,p,y}(z=0) \end{matrix}. \quad (2.15)$$

The boundary conditions in Eq. (2.15) define a set of four linear equations:

$$\begin{gathered} \alpha_{2^+} e^{-ik_{ez}d} + \alpha_{2^-} e^{+ik_{ez}z} = \alpha_1 \\ \alpha_{2^+} + \alpha_{2^-} = \alpha_3 \\ \frac{\epsilon_\perp}{q_{2z}} \left(\alpha_{2^+} e^{-ik_{ez}d} + \alpha_{2^-} e^{+ik_{ez}z} \right) = -\frac{\epsilon_3}{q_{3z}} \alpha_1 \\ \frac{\epsilon_\perp}{q_{2z}} (\alpha_{2^+} + \alpha_{2^-}) = -\frac{\epsilon_3}{q_{3z}} \alpha_3. \end{gathered} \quad (2.16)$$

By solving the system of equations in Eq. (2.16) we obtain the dispersion relation of the HVMs in a thin film of h-BN

$$i \tan(k_{2z} d) = \frac{k_{2z} \epsilon_\perp (k_{1z} \epsilon_3 + k_{3z} \epsilon_1)}{\epsilon_1 \epsilon_2 k_{2z}^2 + \epsilon_\perp^2 k_{1z} k_{3z}}. \quad (2.17)$$

Equation (2.17), given by the transcendental expression, allows one to calculate the wavevector in the direction of propagation, k_x, as a function of the height of the waveguide, and the permittivities of the materials.

This equation simplifies in the quasistatic limit ($k_x \gg k_0$)[87,88]:

$$k_{x,n} = \frac{-i\sqrt{\frac{\epsilon_\parallel}{\epsilon_\perp}}}{d} \left[\arctan\left(i \frac{\epsilon_1}{\epsilon_\perp \pm \sqrt{\frac{\epsilon_\parallel}{\epsilon_\perp}}} \right) + \arctan\left(i \frac{\epsilon_3}{\epsilon_\perp \pm \sqrt{\frac{\epsilon_\parallel}{\epsilon_\perp}}} \right) + \pi n \right], \quad (2.18)$$

where $n = 0,1,2,\ldots$ is the mode index.

2.3.2 Hyperbolic Volume Modes in thin h-BN films

In this section, we study the electromagnetic modes sustained by h-BN thin films in the h-BN upper and lower Reststrahlen bands. For that, we make use of the quasistatic dispersion relation, given by Eq. (2.18). To describe the dispersion of the hyperbolic volume modes, Mn, in h-BN thin films, we choose a 40 nm thick h-BN film (typical thickness of exfoliated thin films). The film thickness is thus two orders of magnitude smaller than the wavelength of light in free space. We calculate the dispersion of the HVMs (Figure 2.3a) for frequencies inside both the Type I Reststrahlen band (760-825 cm^{-1}) and Type II Reststrahlen band (1360-1614 cm^{-1}). In each Reststrahlen band, the h-BN thin film support a set of hyperbolic volume modes (HVMs), denoted as Mn, being n the mode index (Eq. 2.18). The spatial distribution of the vertical component of the electric field for the M0, M1 and M2 modes at ω = 1420 cm^{-1} is shown in Fig. 2.3c-e. Each mode Mn has n+1 nodes in the vertical direction so that, for instance, the M0 mode has only one node. As observed in Fig. 2.3c-e, the lateral confinement increases for higher mode indices n, while the wavelength of the mode decreases. In contrast to dielectric waveguides[8] the higher the mode index n, the larger the wavevector, (see Fig. 2.3a). The latter is much larger than k_0, $|Re(k_{Mn,x})| \gg k_0$ in both Reststrahlen bands. The dispersion of the modes follows a different trend in the upper and lower Reststrahlen band. Namely, in the Type II Reststrahlen band (ω =1360-1610 cm^{-1}), the wavevector of the Mn modes has its minimum value near the TO phonon frequency and it increases with frequency, reaching an asymptote at the LO phonon frequency. In contrast, in the Type I Reststrahlen band (ω =760-825 cm^{-1}) the trend is the opposite: the highest values of the wavevectors are reached near TO phonon frequency, and its magnitude decreases with frequency, reaching its minimal value at the LO phonon frequency. Moreover, as it has been proved experimentally[127], the phase velocity of the HVMs, $v_{\mathrm{ph,M}n} = \omega/k_{\mathrm{M}n}$, in the Type I band is negative and thus, the sign of the real part of the wavevector of the Mn modes is negative (we represent the absolute value of the wavevector in Fig. 2.3a for compactness). On the contrary, the group velocity, $v_{g,\mathrm{M}n} = \frac{\partial \omega}{\partial k_{\mathrm{M}n}}$, is positive in both Reststrahlen bands[127], and very small compared to the speed of light in free space (with measured values of[127] $v_{g,\mathrm{M0}} = 0.003 \cdot \mathrm{c}$).

In spite of their large momenta, HVMs can be excited in nanoimaging experiments[128] by a tip of an scattering-type scanning near-field optical microscope (s-SNOM)[128] (localized source) which provides sufficiently large momenta.

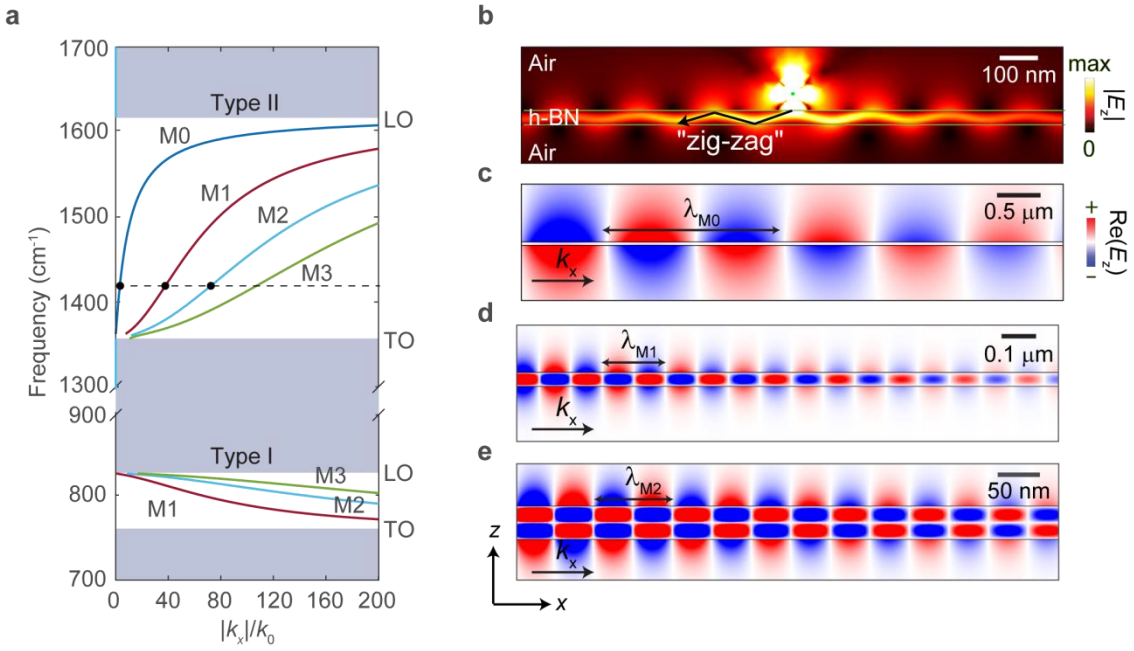

Figure 2.3: HVMs in thin h-BN films. (a) Dispersion of the HVMs in the upper and lower Reststrahlen bands of h-BN in the mid-IR, for a $d = 40$ nm thickness film surrounded by air, $\epsilon_{1,3} = 1$. The sign of the wavevector of the modes in the lower Reststrahlen band is negative. We represent the absolute value of the wavevector for compactness. **(b)** Dipole source (green dot) launching the HVMs of a thin film, forming a characteristic "zig-zag" pattern, for the same system as **(a)**. **(c-e)** Vertical component of the electric field of the **(c)** M0, **(d)** M1, and **(e)** M2 modes, propagating from left to right. Note the different scale in each panel. The frequency in **(b-d)** is marked by a dashed line in **(a)**, $\omega = 1420\ \mathrm{cm}^{-1}$.

Similarly to the tip, HVMs can be excited by other localized sources. a metallic antenna on top of h-BN[129], a metallic edge over the h-BN surface[127] or a wrinkle on the surface of h-BN[130]. To visualize the excitation of the HVMs by a localized source, we simulate the distribution of the electric field induced by a vertically oriented dipole over the h-BN slab (Fig. 2.3b). Near the dipole the field distribution shows a "zig-zag" pattern. The "zig-zag" pattern results from the superposition of many excited Mn modes[131], but can also be seen as the reflections of the hyperbolic ray from bottom and top interfaces of the slab (since the angles of the zigzag coincides with the angle $\theta_{\mathrm{HR}} = \arctan\sqrt{-\frac{\epsilon_{\perp}}{\epsilon_{||}}}$ defining the hyperbolic ray). Because the higher order modes decay faster than the lower order ones, the "zig-zag" pattern fades away far from the dipole; and for long distances, only the lower modes with small wavevectors and long propagation lengths remain.

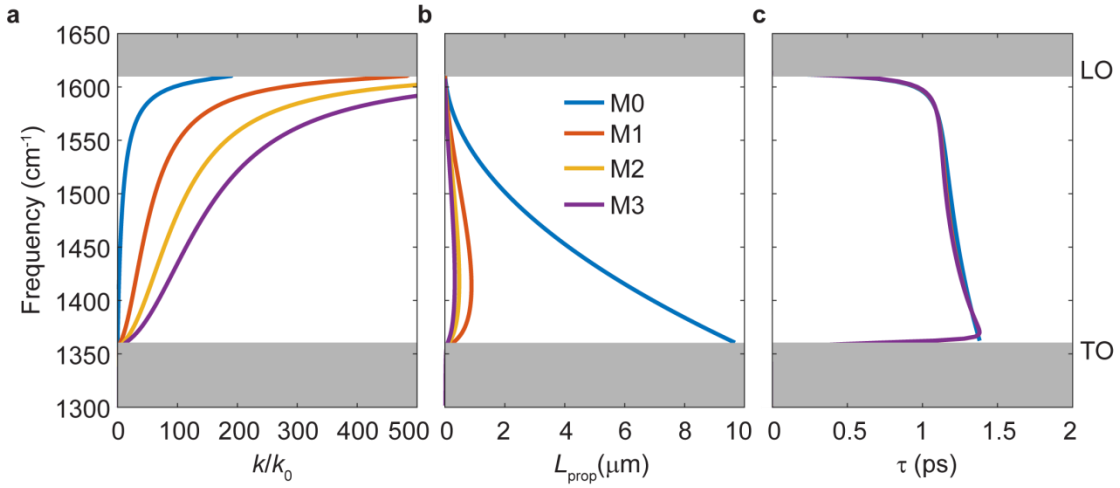

Figure 2.4: Propagation length and lifetime of the HVMs (a) Dispersion curves of the M0, M1, M2 and M3 modes in the upper Reststrahlen band. **(b)** Propagation lengths. **(c)** Lifetimes. Note that the different curves superimpose in **(c)**. The grey regions indicate the frequencies outside the h-BN upper Reststrahlen band. Thickness of h-BN, d = 50 nm. The h-BN layer is surrounded by air.

In Figure 2.4 we analyze the propagation lengths and lifetimes of the HVMs in the upper Reststrahlen band. Figure 2.4a shows the dispersion of the four analyzed volume modes, (from M0 to M3), with momenta up to $k = 500 \cdot k_0$. The calculated propagation lengths of the modes, defined as $L_{prop} = \frac{1}{k''_{x,\mathrm{M}n}}$ (where $k''_{x,\mathrm{M}n}$ is the imaginary part of the propagation constant $k_{x,\mathrm{M}n} = k'_{x,\mathrm{M}n} + ik''_{x,\mathrm{M}n}$), is shown in Fig. 2.4b. The propagation length of the M0 mode monotonically increases with decreasing frequency, reaching a maximal value of 10 microns (while for frequencies higher than 1550 cm^{-1} it propagates less than a micron). The rest of the modes propagate less than one micron for all frequencies, thus indicating their weak contribution into the near-field images in the experiments. The lifetime of a HVM, defined as $\tau_{\mathrm{M}n} = \frac{L_{prop,\mathrm{M}n}}{v_{g,\mathrm{M}n}}$ (where $v_{g,\mathrm{M}n} = \frac{\partial \omega}{\partial k_{\mathrm{M}n}}$ is the group velocity) has similar values for all modes as shown in Fig. 2.4c. The lifetime of the HVMs is remarkably large (around 1 ps). Indeed, its lifetime is larger than the lifetime of plasmons in metals[16] and graphene[77] and is comparable with the lifetime of SPhPs in other polar materials such as SiC[56], although being smaller than the lifetime of the recently discovered PhPs in MoO_3[87]. The lifetime of HVMs in h-BN can be further increased by isotopically enriching h-BN[132]. As seen from Fig. 2.4c the lifetime of the modes Mn, $\tau_{\mathrm{M}n}$, is rather constant as a function of frequency,

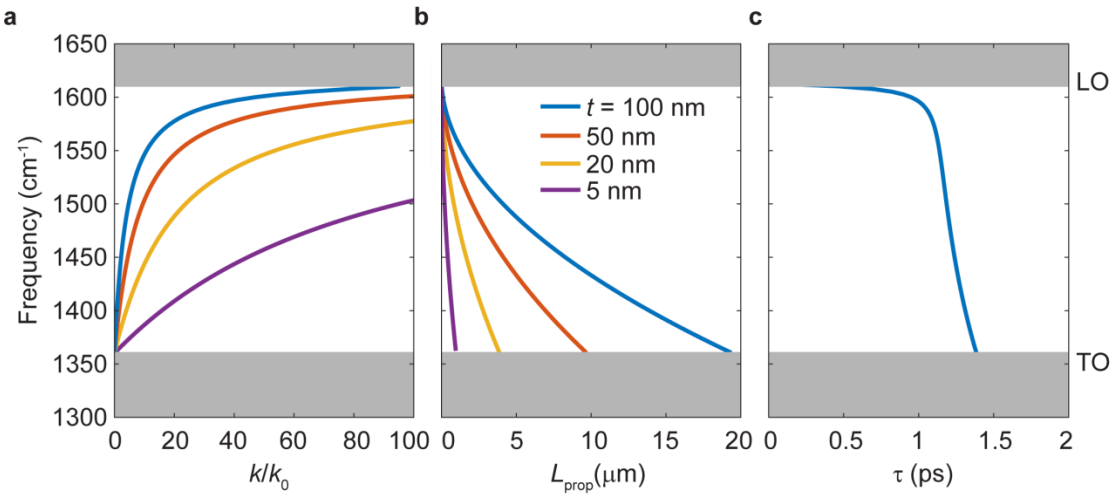

Figure 2.5: M0 mode properties as a function of h-BN thickness(a) Dispersion curves of the M0 mode in the upper Reststrahlen band for h-BN thicknesses d = 5, 20, 50 and 100 nm. **(b)** Propagation lengths. **(c)** Lifetimes. The grey regions indicate the frequencies outside the h-BN upper Reststrahlen band. Note that the different curves superimpose in **(c)**. h-BN thickness, d = 50 nm. The h-BN layer is surrounded by air.

indicating that the dispersions of the propagation lengths, L_{prop}, and the group velocity , v_g, compensate each other. As demonstrated later on (Section 4.9), the lifetime of the M0 mode in h-BN is approximately proportional to $1/\gamma_\perp$, where $\gamma_\perp$ is the damping rate in the x- and y-directions in the Drude-Lorentz model of h-BN permittivity, Eq. (1.7), and thus constant with respect to the frequency.

Importantly, the mode dispersion of HVMs is strongly dependent on the h-BN thickness, d. Figure 2.5a shows the dispersion of the M0 mode, for different thicknesses d. As seen from the figure, the wavevector magnitude $k_{x,\mathrm{M0}}$ increases with the decrease of d, for any given frequency. This dependence is consistent with Eq. (2.18), in which the wavevector $k_{x,\mathrm{Mn}}$ depends upon the h-BN thickness as $k_{x,\mathrm{Mn}} \propto \frac{1}{d}$. On the other hand, the propagation length of the M0 mode decreases with the decrease of d, as observed in Fig. 2.5b. At the same time, the lifetime of the M0 mode, (shown in Fig. 2.5c) is virtually independent upon d in the shown frequency range.

The first observation of HVM M0 in h-BN by nanoimaging experiments[80] in thin flakes of h-BN confirmed its high wavevectors and long lifetimes. Subsequent experiments also allowed for the detection of the higher order modes[123](M1 and

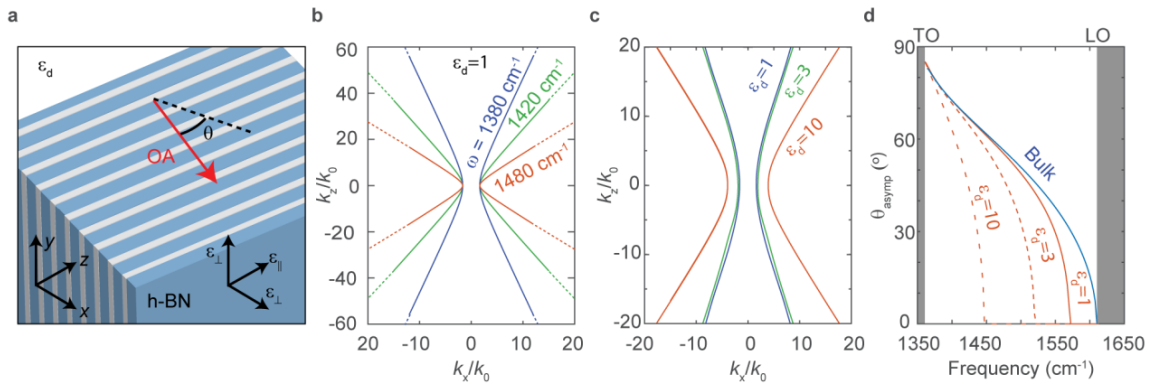

Figure 2.6: Hyperbolic Surface Polaritons on h-BN-air interfaces (a) Sketch of the system. The layered atomic structure of h-BN is indicated by the alternating blue and white colors. **(b)** Isofrequency curve of the HSPs for different frequencies. Dashed lines are guides to the eye. **(c)** Isofrequency curve of the HSPs for different dielectric permittivities. (**d)** Asymptote angle of bulk HVPs and HSPs as a function of frequency, and dielectric surroundings for the case of HSP.

M2), with larger wavevectors and smaller propagation lengths (thus, these experiments being more challenging)

2.4 Hyperbolic Surface Waves at h-BN-air interfaces

An interface between an isotropic material and a uniaxial crystal (with the optical axis parallel to the interface) can support surface waves. These waves, called Dyakonov surface waves[133], were originally studied by Dyakonov for an interface between an isotropic and a uniaxial material with real and positive elements of the permittivity tensor. Since the parametric range in which Dyakonov surface waves exist is rare for natural materials, the experimental evidence of Dyakonov surface waves took around two decades. Finally, these waves were observed in artificial metamaterials[134].

Another representative of the "Dyakonov surface waves family" called Hyperbolic Surface Polaritons (HSPs), are surface waves at an interface between a dielectric and a material hyperbolic material[108,109]. In this section we illustrate HSPs

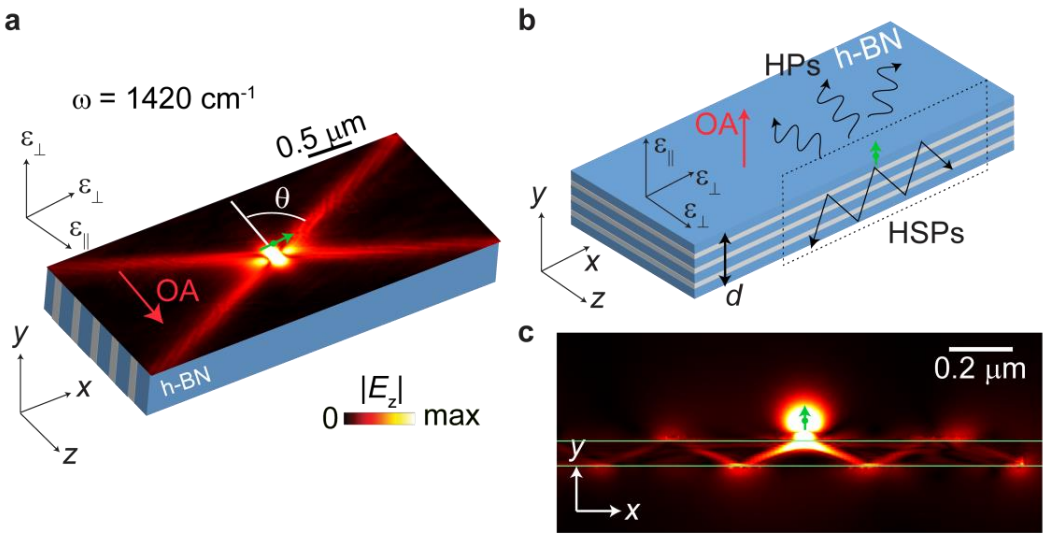

Figure 2.7: Launching of HSPs at the interface between h-BN and air (a) Electric dipole source (green dot and arrow) launching hyperbolic surface polaritons at the interface between h-BN and air, at a frequency $\omega = 1420\ \mathrm{cm}^{-1}$. The OA is oriented parallel to the surface (red arrow). Color plot indicates $|E_z|$. **(b)** Schematics showing the launching of HSPs and HVPs by an electric dipole located near the edge of the thin film with a thickness d = 100 nm. The OA is oriented in the y-direction. The dotted rectangle indicates the plane near the edge of the flake where the fields in **(c)** were calculated. **(c)** Zig-zag pattern created due to the launching of HSPs by a dipole source at the edges of the h-BN flake. Color plot represents $|E_z|$. The green dot and arrow represents the dipole source. The layered atomic structure of h-BN is indicated in **(a)** and **(b)** by the alternating blue and white colors.

supported at an interface of an h-BN crystal, in case the interface is parallel to the optical axis.

The sketch of the studied system is shown in Figure 2.6a. The isotropic dielectric occupies the half-space $y > 0$, while h-BN occupies the half-space $y < 0$. The optical axis (OA) of h-BN is parallel to the interface between the two materials (parallel to the x-direction, indicated by the red arrow in Fig. 2.6a). The dispersion of the hyperbolic surface waves is described by the following equation[135]

$$(q_d + q_2)(q_s + q_o)(\epsilon_d q_o + \epsilon_\perp q_e) = (\epsilon_\parallel - \epsilon_d)(\epsilon_d - \epsilon_\perp)q_o, \qquad (2.19)$$

where $q_o = \sqrt{q_x^2 + q_z^2 - \epsilon_\perp}$, $q_d = \sqrt{q_x^2 + q_z^2 - \epsilon_d}$, and $q_e = \sqrt{q_z^2 + \frac{\epsilon_\parallel}{\epsilon_\perp} q_x^2 - \epsilon_\parallel}$. Eq. (2.19) does not have solutions for the case of $\epsilon_\parallel < 0$, and thus HSPs *cannot* exist in the

Type I Reststrahlen band of h-BN. Nevertheless this condition is fulfilled in the Type II Reststrahlen band. The HSP isofrequency curve in the Type II Reststrahlen band is an open hyperbola, as shown in Figure 2.6b. HSPs thus can comprise waves with very large wavevectors that are confined to certain specific directions along the interface[136]. The opening angle of the hyperbola strongly depends upon frequency (Fig. 2.6b), being more acute for higher frequencies, as $|Re(\epsilon_\perp)|$ becomes smaller. On the other hand, the position of the vertex of the hyperbola strongly depends on ϵ_d (Fig. 2.6c). In contrast to HVPs in bulk h-BN, the angle formed by the hyperbolic rays formed by HSPs with high wavevectors depends also on the permittivity of the isotropic dielectric, ϵ_d, as it is observed in Figure 2.6c. This dependence is given by

$$\theta_{\text{asymp},HSP} = \frac{\pi}{2} - \text{asin}\sqrt{\frac{\epsilon_d^2 + |\epsilon_\perp|\epsilon_\parallel}{|\epsilon_\perp|(\epsilon_\parallel + |\epsilon_\perp|)}}. \quad (2.20)$$

The angle $\theta_{\text{asymp},HSP}$ is shown in Figure 2.6d as a function of the frequency for different ϵ_d (red, solid and dashed lines), along with the angle of the asymptote of the HVPs in bulk h-BN, given by $\theta_{\text{asymp},HVP} = \arctan\sqrt{-\frac{\epsilon_\perp}{\epsilon_{||}}}$ (blue solid line). We observe that, at a given frequency, the angle of the asymptote for HVPs is always larger than the angle of the asymptote of HSPs. Moreover, the angle $\theta_{\text{asymp},HSP}$ decreases with the increase of ϵ_d. The cutoff frequency of the HSPs (the highest frequency at which the HSPs exist) is given by the condition $\epsilon_d = -\epsilon_\perp$ (differently from HVPs where the cut-off is given by the condition $\epsilon_\perp = 0$), and takes place when $\theta_{\text{asymp},HSP}$ becomes zero.

To visualize the propagation of HSPs we perform full-wave simulations of the electromagnetic fields created by a point dipole placed in air near the surface of h-BN. Differently from Section 2.3, the surface of h-BN has a high in-plane anisotropy, since the h-BN OA is parallel to the surface (parallel to the z-direction). The dipole source, oriented parallel to the surface, launches HSPs that propagate away forming highly confined and directional rays, bounded to the surface (Figure 2.7a). This directional rays comprise HSPs with high wavevectors, hence, propagating with an angle $\theta \approx \theta_{\text{asymp},HSP} = 68º$. Note that the dipole source also launches HVPs (Section 2.2) that propagate inside the h-BN crystal forming a cone[137], which are not shown in the images for clarity.

In exfoliated h-BN films the optical axis is perpendicular to the faces of the film. In this case, as discussed above, h-BN films do not support HSPs (unless the flake is nanostructured into a metasurface[138]). Nevertheless, at the lateral sides of the flakes

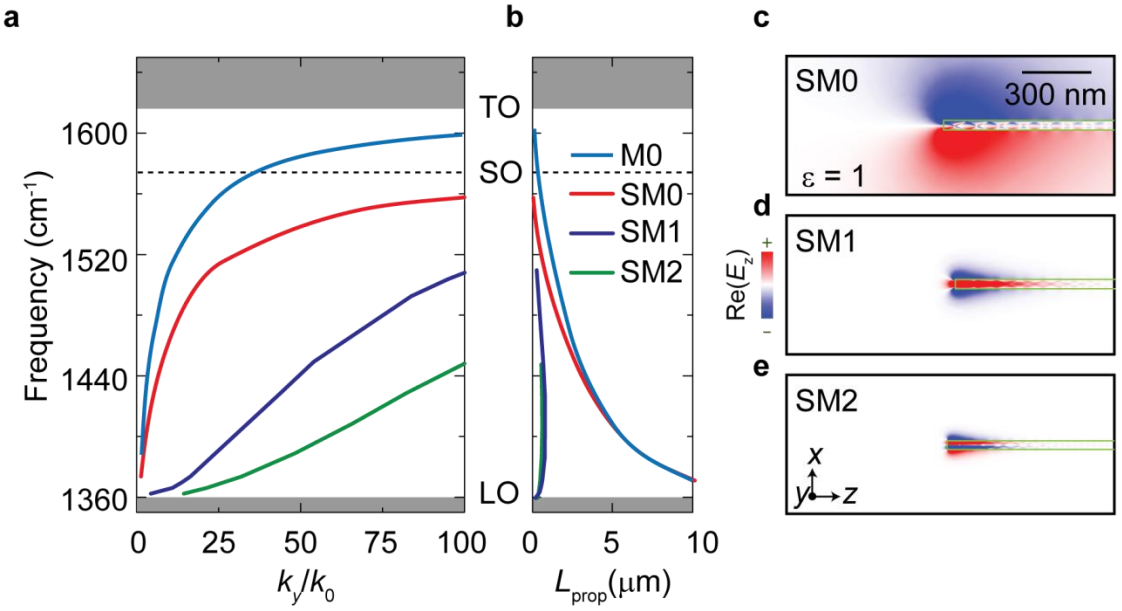

Figure 2.8: Hyperbolic surface modes at the edges of h-BN flakes. (a) Dispersion or the M0 mode in a slab of h-BN, and dispersion of the modes SM0, SM1 and SM2 modes at the edges of an h-BN flake of thickness $d = 40$ nm surrounded by air. White background indicates the upper Reststrahlen band of h-BN. **(b)** Propagation length of the M0, SM0, SM1 and SM2 modes. **(c-e)** Real part of the vertical component of the electric field for a plane perpendicular to the propagation direction of the **(c)** SM0, **(d)** SM1 and **(e)** SM2 modes at a frequency $\omega = 1420\, cm^{-1}$. The h-BN flake contour is marked by the green lines.

the optical axis is parallel to the surface (Fig. 2.7b), and thus can support HSPs. Due to the nanometric thickness of the slab, the directional HSPs excited by a localized source experience multiple reflections at the bottom and top corner of the slab, forming a "zig-zag" pattern confined to the edge of the slab, as shown in Fig. 2.7c. This "zig-zag" pattern can be decomposed as a sum of different HSP modes confined at the edges of h-BN, which we will analyze in the next section.

2.5 Hyperbolic Surface Modes at the edges of h-BN

The "zig-zag" pattern confined h-BN flake edges (Fig. 2.7c) can be described as a superposition of guided modes confined to the h-BN flake edge. These modes are

called Hyperbolic Surface Modes (HSM), and denoted as SMn, being n the index of the mode. There is no available analytical solution for HSMs, differently from HVMs, so our study will rely on numerical calculations. The calculated field distribution of the SM0, SM1 and SM2 modes is shown in Fig 2.8c-e, and evidences the confinement of the modes to the edge of the thin film. In general, the distribution of E_z of the SMn mode has n+1 nodes in the vertical direction.

For instance, the SM0 mode distribution of E_z has one node in the vertical direction. as observed in Figs. 2.8c-e. Moreover, the confinement of the SMn modes to the h-BN flake edge increases for higher mode indices n. The dispersion curves of the modes shown in Fig. 2.8a indicate that HSMs in thin films have wavevectors much higher than the wavevector of light in free space, that is, they are deeply subdiffractional. The wavevector of the modes increases with frequency, and approaches asymptotically a frequency, denoted as SO, where the condition $\epsilon_\perp = -\epsilon_{air} = -1$ is fulfilled. At this frequency, HSMs ceases to exist[137], differently from HVMs which exist up to the LO phonon frequency (see section 2.3.2). Further, for the same mode order n, the dispersion of an HSM is steeper than the dispersion of an HVM, and hence the group velocity of HSMs is smaller than that of hyperbolic volume modes[137]. As observed in Fig. 2.8a, higher order HSMs possess higher wavevectors, and interestingly, HSMs (as the SM0 in Fig. 2.8a) have higher wavevectors than HVMs of the same order (as the M0 in Fig. 2.8a), thus being promising candidates for improving the subwavelength confinement of light.

At a given frequency, the propagation length of the HSMs, defined as $L_{\mathrm{prop}} = \frac{1}{k''_{x,\mathrm{SM}n}}$, is smaller the higher the mode index of the HSM (Fig. 2.8b). Similar to HVMs, the propagation length reduces monotonically with frequency. Moreover, for the considered thickness (which is similar to typical experimental thicknesses), the propagation length of the lowest mode, SM0, vastly exceeds the propagation length of higher order surface modes, thus anticipating that the SM0 mode will be prominently excited in nanoimaging experiments. The propagation length of the SM0 mode is similar to the propagation length of the fundamental volume mode M0, as shown in Fig. 2.8b.

HSMs were firstly observed by polaritonic interferometry[71] (Fig. 2.9a), in thin flakes of h-BN over a SiO_2 substrate[137]. In this kind of experiments, the metallized tip of a scattering type scanning near-field optical microscope (s-SNOM) is illuminated by an infrared beam (E_{inc}), that converts the incident light into strongly enhanced and confined near fields at the tip apex[139] (of radius around 30nm). The tip, thus, acting similar to the dipole source in Figs. 2.3 and 2.7, launches hyperbolic surface modes SMn and hyperbolic volume modes Mn along

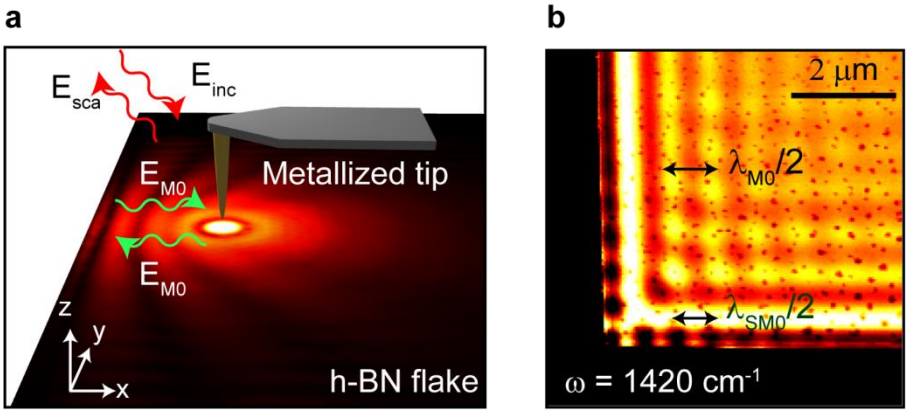

Figure 2.9: (a) Polariton interferometry scheme illustration. The metallized tip acts as a hot-spot for launching polaritons (being the M0 mode the most prominently excited at the tip position considered), which propagate toward the edge of the flake, and gets reflected back, giving rise to a standing wave pattern that can be visualized in the color plot. **(b)** Near-field imaging of an h-BN flake, showing the M0 (bright fringes at the center of the h-BN flake) and SM0 modes (dark spots at the edges of the h-BN flake). (b) is taken from Ref. [137].

the h-BN flake (Fig. 2.9a illustrates the launching of the M0 mode by the illuminated tip). Upon reflecting at the edges of the h-BN flake, these modes reach the tip again. The launched and reflected waves interfere, creating a standing wave pattern (Fig. 2.9a). modulating the field below the tip, and hence the light scattered by the tip (E_{sca}),), that is measured by a detector placed in the far-field[71]. Due to the interference between the launched and edge-reflected waves, the spacing between fringes in the nanoimaging experiments corresponds to half of the wavelength of the polaritonic mode (as Fig. 2.9b). By performing nanoimaging experiments, the hyperbolic surface mode SM0[137] was observed for the first time (see Fig. 2.9b), confirming its short wavelength, long lifetime and high spatial confinement, and anticipating its potential usefulness for the design of nanostructured devices, such as nanoantennas sustaining high-Q resonances.

3. Linear antennas made of h-BN

In this chapter, we analyze phonon polaritonic Fabry-Perot resonances in linear antennas made of a natural hyperbolic material, hexagonal boron nitride. Infrared nanospectroscopy and nanoimaging experiments reveal sharp resonances with large quality factors around 100, exhibiting atypical modal near-field patters that have no analogue in conventional linear antennas. By performing a detailed mode analysis, we assign the antenna resonances to a single waveguide mode originating from the hybridization of two hyperbolic surface modes that propagate along the lateral sides of the h-BN waveguide. Our work establishes the basis for the understanding and design of linear waveguides, resonators, sensors and metasurface elements based on hyperbolic materials and metamaterials. This chapter essentially presents the results published in the article "Nanoimaging of resonating hyperbolic polaritons in linear boron nitride antennas" by F.J. Alfaro-Mozaz et al, Nat. Comms. (2017) 8, 15624.

3.1 Introduction

Polaritons (quasiparticles resulting from the coupling of photons and oscillating charges[140]) in nanostructured materials enable strong confinement and enhancement of electromagnetic fields at extreme subwavelength-scale dimensions[141]. Typically, propagating and localized surface plasmon polaritons – collective oscillations of electromagnetic fields coupled to free electrons in metal and semiconductor surfaces[1,9,10]– have been employed. A promising alternative, which is by far less considered yet, are surface phonon polaritons in polar crystals[14,96,115]. These quasiparticles –resulting from the coupling of electromagnetic fields and crystal lattice vibrations– exist from mid-IR to THz frequencies in the so-called Reststrahlen band (defined as the region between the transversal and longitudinal optical phonon frequencies, TO and LO, respectively), where the real part of the crystals` dielectric permittivity is negative. They offer significantly improved field enhancements and quality factors compared to plasmons[14,96,116]. At mid-IR frequencies, they have been studied, for example, in SiC[56], quartz[142] and MoO_3[87], and could find applications in thermal emission control[48,117,118] and sensing[119,120].

The emergence of van der Waals materials opens novel opportunities for polariton-based photonic technologies[124]. Particularly, hexagonal boron nitride (h-BN) exhibit mid-IR phonon polaritons with remarkably low losses[28,88,121], while high-quality single crystalline layers are easy to prepare by exfoliation. Furthermore, due to their layered crystal structure (uniaxial anisotropy), the permittivity tensor ϵ is diagonal, with $\epsilon_{zz} = \epsilon_{\parallel}$

and $\epsilon_{xx} = \epsilon_{yy} = \epsilon_{\perp}$ being the components parallel and perpendicular to the anisotropy axis, respectively. As explained in Chapter 2, when $\mathrm{Re}(\epsilon_{\parallel}) \cdot \mathrm{Re}(\epsilon_{\perp}) < 0$ phonon polaritons propagate inside the material and exhibit a hyperbolic dispersion[98,143], *i.e.* the isofrequency surface of the HVPs wavevector $\boldsymbol{q}(\omega) = (q_x, q_y, q_z)$ is a hyperboloid. h-BN has two Reststrahlen bands, where one of the permittivity components is negative. In the lower Reststrahlen band (760-825 cm^{-1}) the real part of the out-of-plane permittivity $\mathrm{Re}(\epsilon_{\parallel})$ is negative (Type I hyperbolic dispersion), while in the upper Reststrahlen band (1360-1614 cm^{-1}) the real part of the in-plane permittivity $\mathrm{Re}(\epsilon_{\perp})$ is negative (Type II hyperbolic dispersion). The hyperbolic polaritons[18,22] can propagate with negative phase velocity and slow group velocity[127], showing extreme mode confinement in thin slabs[28,81,121] and nanotubes[144]. High quality factors of phonon polariton resonances (up to 283) in h-BN nanocones have been reported in Ref. 121, promising that phononic antennas made of hyperbolic materials could have strong application potential for IR nanophotonics. In this chapter, we analyze linear waveguide antennas –the most canonical type of antennas, and basic building block in many nanophotonic devices– made of h-BN.

The chapter is organized as follows. In Section 3.2, we describe the fabrication of the h-BN linear antennas by electron beam lithography. In Section 3.3 we describe the nanospectroscopy and nanoimaging setup used to study the antennas. Section 3.4 describes the infrared nanospectroscopy results of a representative antenna, which reveal resonances of high quality factors of about 100. In Section 3.5 we interpret the resonances via a detailed analysis of the waveguide modes sustained by an h-BN waveguide with rectangular cross-section. We find that, surprisingly, the resonances are governed by hyperbolic surface modes (Dyakonov polaritons[108,124-127]) rather than hyperbolic volume modes. Section 3.6 shows near-field images of the antennas and discusses the puzzling near-field patterns observed in the experiments. The chapter finishes with conclusions and outlook (Section 3.7).

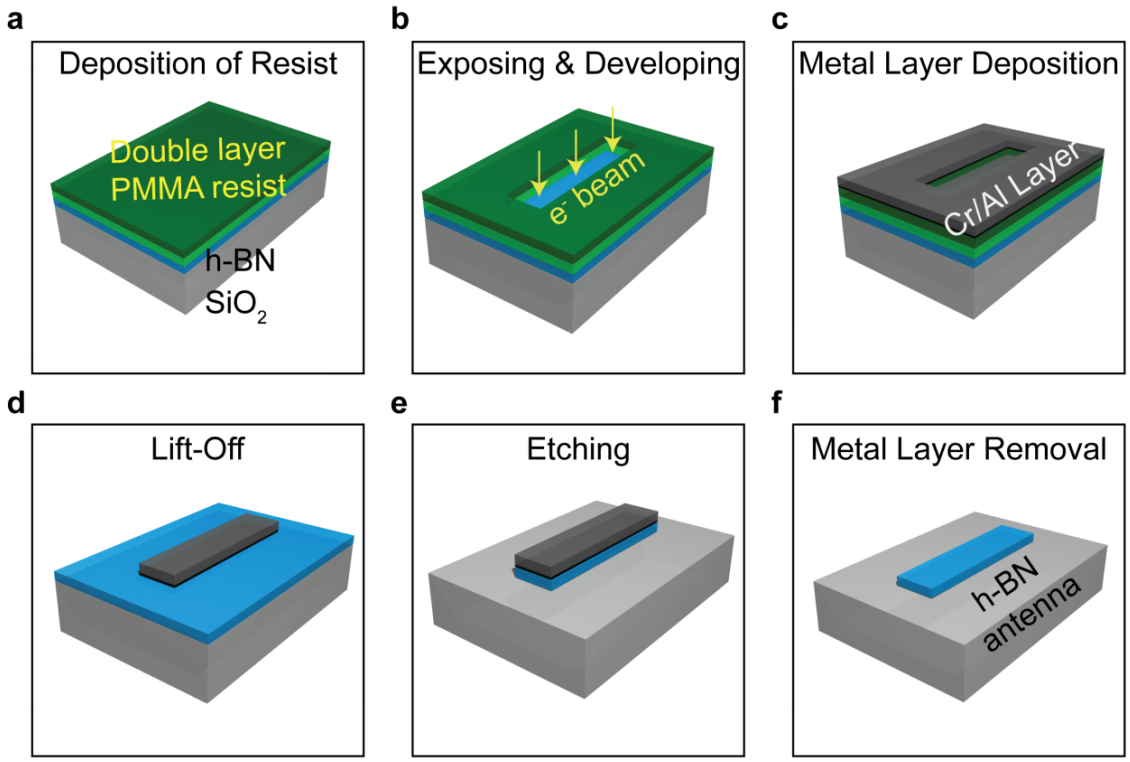

Figure 3.1: Sketch of the of the h-BN antennas fabrication process. The chronology develops from (a) to (f).

3.2 Fabrication of the h-BN antennas

The fabrication of the antennas was performed by Irene Dolado and Saül Vélez at CIC NanoGUNE BRTA.

First, large and homogeneous h-BN flakes were isolated and transferred onto a 250 nm thick SiO_2 layer on Si. To that end we first performed mechanical exfoliation of commercially available h-BN crystals (HQ graphene Co, N2A1) using blue Nitto tape (Nitto Denko Co., SPV 224P). Then, we performed a second exfoliation of the h-BN flakes from the tape onto a transparent Polydimethyl-siloxane (PDMS) stamp. High-quality flakes with large areas and required thickness were identified (via both optical inspection and atomic force microscope (AFM) characterization of h-BN flakes on the stamp) and then transferred onto a Si/SiO2 (250 nm) substrate using the deterministic dry transfer technique[128,129].

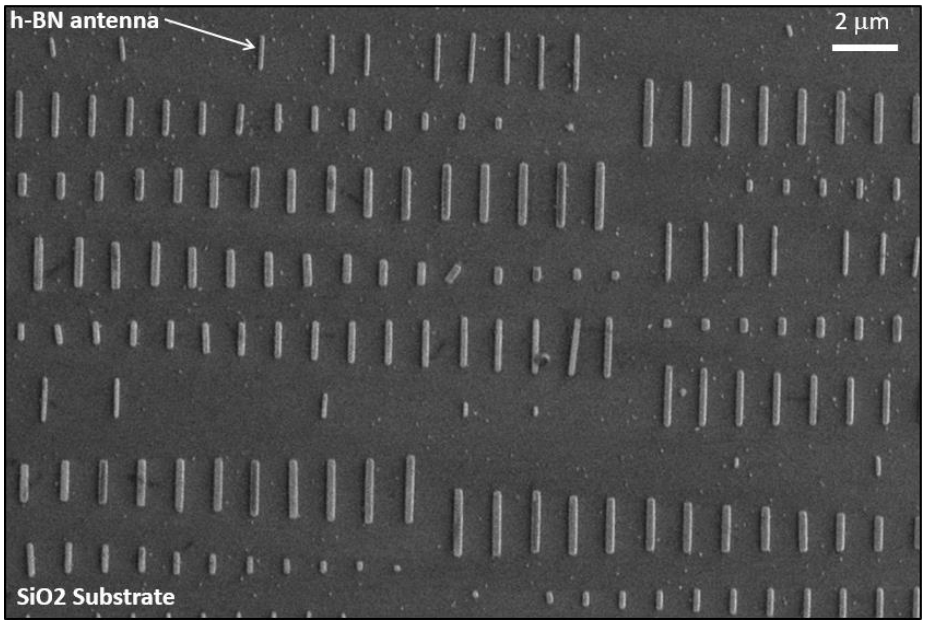

Figure 3.2: Top view scanning electron microscope image of a representative array of h-BN antennas fabricated on a SiO_2 substrate.

Once the flakes were transferred to the SiO_2/Si substrate, the antennas were fabricated as illustrated in Figure 3.1. First, a double layer PMMA 495 A4/950 A2 (positive-tone resist) was spin-coated onto the sample (Fig. 3.1a, the double layer represented by the bright and dark green layers). Then the h-BN antennas were defined via high resolution electron beam lithography, where the area of the antenna was exposed to the electron beam. Afterwards, the sample was immersed in Methyl isobutyl ketone (MIBK) for 1 minute and rinsed in isopropyl alcohol to remove the resist (Fig. 3.1b).

After the development procedure, a metal mask was deposited by electron-beam evaporation of chromium (3 nm) followed by thermal evaporation of aluminum (40 nm), as depicted in Fig. 3.1c. The lift-off of the PMMA layer was done in acetone (Fig. 3.1d), and was followed by chemical etching in a SF6/Ar 1:1 plasma mixture at 20 sccm flow, 100mTorr pressure and 100 W power for 30 sec (Fig. 3.1e). A commercially available reactive ion etching system (RIE OXFORD PLASMALAB 80 PLUS) was used for this process. Finally, the metal mask was removed by immersing the sample in chromium etchant (Sigma-Aldrich Co., 651826) for 20 min. Afterwards, the sample was rinsed in deionized water and dried using a N_2 gun (Fig. 3.1f). The fabricated array of antennas containing different widths and lengths is shown in the Scanning Electron Microscope (SEM) images, Figs. 3.2 and 3.3.

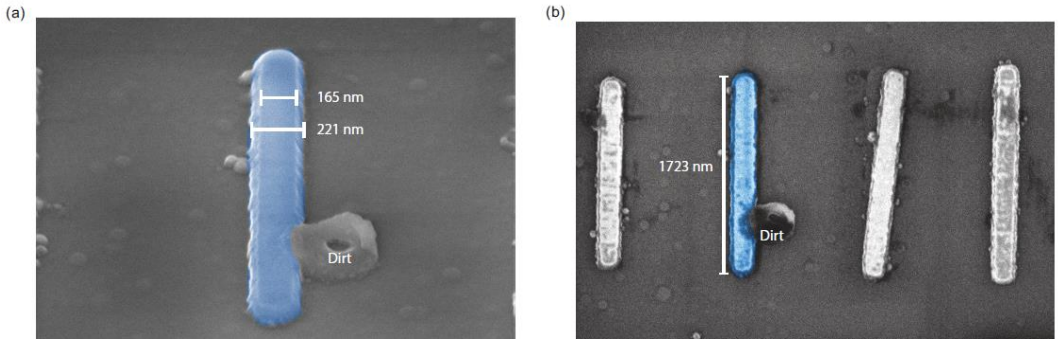

Figure 3.3: Scanning electron microscope (SEM) image of an h-BN antenna. (a) SEM image with the sample being tilted by 48º relative to the surface normal, to better recognize its transverse cross-section. The blue colored h-BN antenna is the one studied in Section 3.4. Note that the ring-like dirt particle next to the antenna was deposited after the near-field measurements shown in Section 3.4. **(b)** Top-view SEM image of the antenna shown in panel **(a).**

3.3 IR nanoimaging and nanospectroscopy setup

3.3.1 Concept

For infrared nanoimaging and nanospectroscopy we used a scattering-type scanning near-field optical microscope (s-SNOM). It is equipped with a Fourier transform spectrometer, which allows for nanoscale Fourier transform infrared (nano-FTIR) spectroscopy of the antennas. The nanoimaging and nanospectroscopy concept is illustrated in Fig. 3.4. The metallic scanning probe tip (cantilevered standard Pt-coated silicon tip) of the s-SNOM is illuminated from the side with a p-polarized infrared beam of electric field E_{inc}. Acting as an infrared antenna, the tip concentrates the incident field into a nanoscale spot at the apex. This nanoscale "hot spot" acts as a local source for launching hyperbolic phonon-polaritons in the h-BN antennas. The HPs are reflected at the ends of the antennas, giving rise to FP resonances. The strongly enhanced near fields caused by these resonances are imaged and spectrally analyzed by recording the field scattered by the tip, E_{s}.

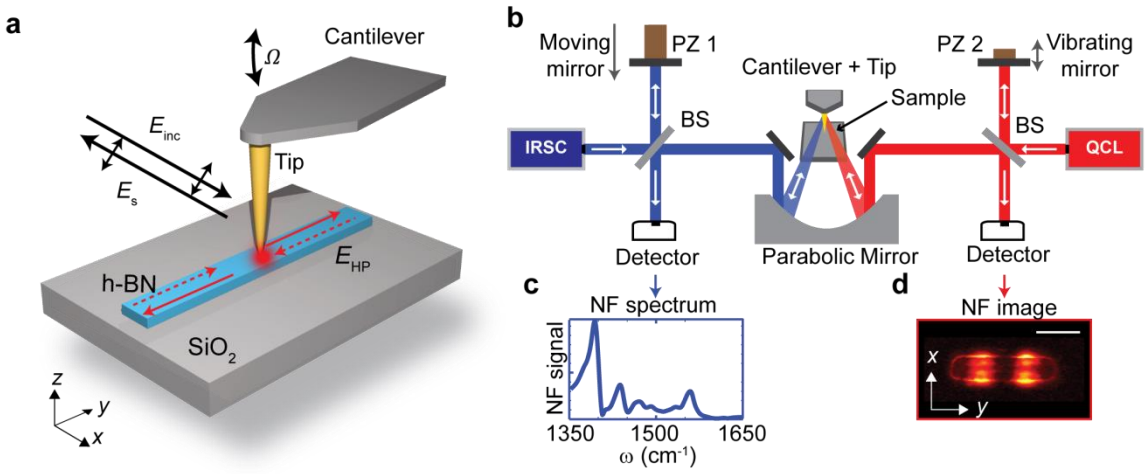

Fig. 3.4: Infrared nanoimaging and nanospectroscopy of linear h-BN antennas. **(a)** Illustration of a metallic cantilevered tip probing a linear antenna of h-BN. The tip oscillates with frequency Ω to allow complete background suppresion. **(b)** Schematics of the s-SNOM/nano-FTIR set-up. For nano-FTIR spectroscopy, we illuminate the tip with a broadband laser (Infrared supercontinuum, IRSC). The backscattered light is analysed with an asymmetric Fourier transform spectrometer (left). BS, beamsplitter, PZ1, piezo-actuated moving mirror. For s-SNOM nanoimaging, we illuminate the tip with a frequency-tunable QCL. The backscattered light is detected with a Michelson interferometer (right)- PZ2, piezo-actuated vibrating mirror. **(c,d)** Examples of the spectra and images taken, respectively. Scale bar in **(d)**, 500 nm

For nanoimaging, we illuminated the tip with the monochromatic infrared light of a frequency-tunable quantum cascade laser (QCL) and recorded the amplitude of the tip-scattered field with a pseudo-heterodyne Michelson interferometer as a function of tip position (right side in Fig. 3.4b). For nano-FTIR spectroscopy, the broadband infrared

radiation from a laser supercontinuum was used for illuminating the tip. The tip-scattered light, E_s , was recorded with an asymmetric Fourier transform spectrometer (left side in Fig. 3.4b, colored in blue). The recorded spectra were normalized to a gold reference, $E_{s,Au}$, yielding near-field amplitude spectra, $\left|\frac{E_s}{E_{s,Au}}\right|$, at a fixed tip position (point spectroscopy, Fig. 3.4c). By recording point spectra as a function of the tip position, we obtained spectral line scans.

3.3.2 Technical details

The nano-FTIR setup is based in a conventional s-SNOM microscope. The metallic tip of an Atomic Force Microscope (AFM) and the sample are illuminated with a broadband mid-infrared laser supercontinuum (spanning 1,200–1,700 cm^{-1}, average power of 1 mW), which is generated by difference frequency generation using a Femtofiber pro IR and a Supercontinuum Infrared laser from Toptica (Germany). Fourier transform spectroscopy is accomplished as follows. The tip-scattered signal is analyzed with an asymmetric Fourier transform spectrometer (left side in Fig. 3.4b), which is based on a Michelson interferometer. In contrast to conventional FTIR spectroscopy techniques, tip and sample are located in one of the interferometer arms[36]. The detector signal is demodulated at a frequency 4Ω (where Ω is the oscillation frequency of the tip) for effective background suppression. An interferogram is measured by recording the demodulated detector signal as a function of the position of the reference mirror, d, at a fixed tip position. Subsequent Fourier transform of the recorded interferogram yields the complex-valued near-field point spectrum, $E_s(\omega)$. We normalized the obtained point spectra to a reference spectrum $E_{s,Au}$, recorded on gold. A complex-valued division yields the normalized near-field point spectra of the sample (Fig. 3.4c).

The acquisition time of an individual interferogram was 10 min. The length of one interferogram is $2 \cdot d_{max} = 800\ \mu m$, resulting in a spectral resolution of 6.25 cm^{-1}. To obtain the spectral line scan shown in Section 3.4.1, we recorded 34 point spectra along the antenna axis, with a smaller step size at the center (40 nm) than at the extremities (80 nm) of the antenna.

3.4 Nanospectroscopy of a single antenna

3.4.1 Experimental results

We start by performing nano-FTIR spectroscopy (Fig. 3.5) of a representative, 1.8 μm long h-BN rod antenna (a SEM image is shown in Fig. 3.3) at its extremity and center (positions marked by red and blue dots respectively in the topography image shown in Fig. 3.5). Within the upper Reststrahlen band we observe several spectrally sharp and closely spaced peaks (denoted by $n = 1,\ldots,6$ in Fig. 3.5) at frequencies ω_n, indicating antenna resonances. From the width of the peaks we estimate quality factors (Q) in the range of Q_n ~ 80-120. They are comparable to the previously reported Q-factors of h-BN nanocones[145] and SiC nanopillars[8], and are higher than the Q-factors reported for metal (plasmonic) antennas in the mid-IR spectral range[146]. The corresponding lifetimes of the resonances ($\tau_n = 2Q_n/\omega_n$) are in the order of half a picosecond.

To identify the origin of the resonances, we performed a spectral line scan (Fig. 3.5d) along the axis of the antenna (marked by dashed line in Fig. 3.5c). For each peak n we find strong near-field signal oscillations along the antenna. The number of the near-field signal maxima and minima is steadily growing with increasing frequency, while the distance between them (along the antenna) decreases. Such behavior is a clear indication of a spectrally evolving standing wave pattern, i.e. longitudinal Fabry-Pèrot resonances in the h-BN rod, similar to plasmon resonances in metal rods[131,132]. We can clearly distinguish the first six longitudinal resonances in Fig. 3.5d, corresponding to the $n = 1, \ldots,6$ peaks in Fig. 3.5a. The first-order dipolar resonance ($n = 1$) manifests at 1370 cm^{-1} by the two near-field signal maxima close to the rod extremities, while the second-order ($n = 2$) resonance (ω = 1395 cm^{-1}) exhibits a strong near-field signal maxima in the center of the rod and two less pronounced near-field signal maxima at the rod extremities. The third-order ($n = 3$) resonance at 1411 cm^{-1} clearly shows the four typical near-field signal maxima along the antenna axis. The trend continues up to the sixth order. However, the peaks become less pronounced, which we attribute to the increase of losses for higher-order longitudinal antenna modes (analogous to plasmonic antennas[110]).

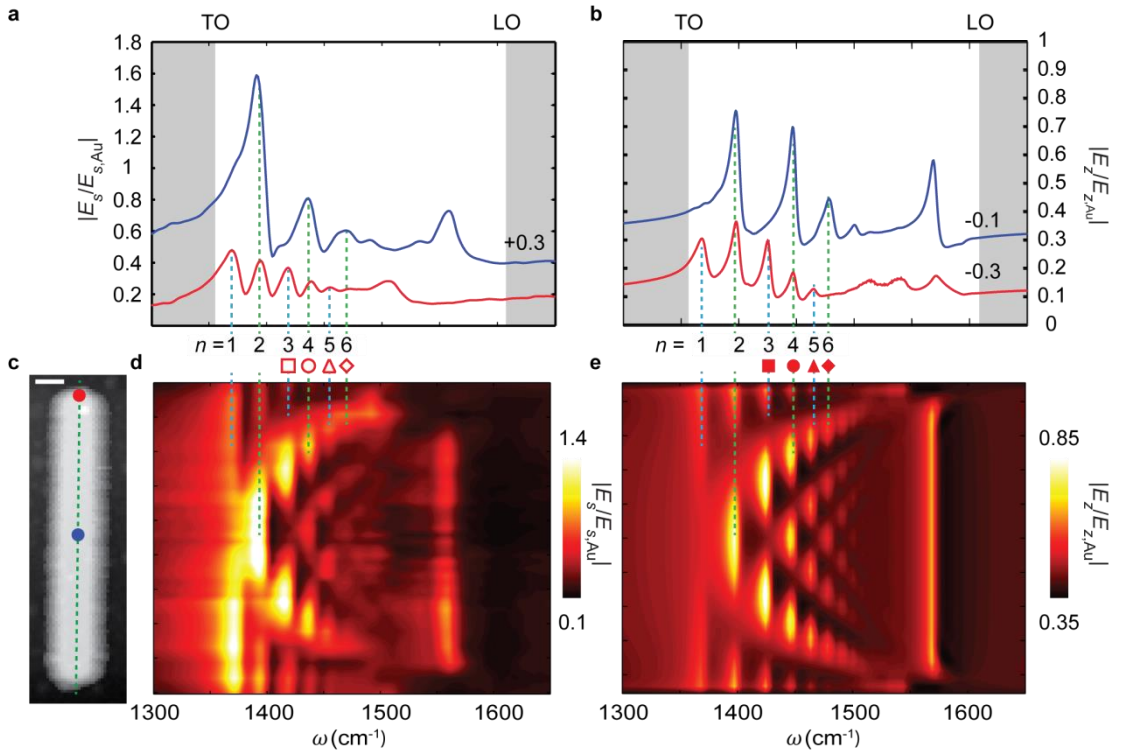

Figure 3.5: Nano-FTIR study of a 1.723 nm long h-BN antenna on SiO_2. (a) Experimental and **(b)** simulated nano-FTIR amplitude spectra. They were obtained at the two position marked by the red and blue dots in **(c)**, and normalized to the nano-FTIR spectrum of a gold film. For clarity, the spectra has been vertically shifted by the indicated values. The white background colour indicates the upper Reststrahlen band. **(c)** AFM topography image of the antenna. The antenna has a thickness of 74 nm (measured from the AFM image). Its average width and height were measured by electron microscopy and amount for 190 nm and 1.723 nm, respectively (See Section 3.2). Scale bar, 200 nm. **(d)** Experimental and **(e)** simulated spectral line scan along the dashed green line in **(c)**. Open and solid symbols mark the resonances analyzed in Fig. 3.6.

3.4.2 Simulations

To corroborate our experimental data we perform full-wave simulations of the near-field spectra. To that end, we used a model where the metallic tip is approximated by a dipole source located above the antenna[70]. This model has been shown to reliably reproduce the experimental near-field images in graphene nanoresonators[70]. By plotting the normalized near field below the dipole as a function of frequency, ω (for a fixed dipole position), we obtain near-field spectra,

$\left|\frac{E_z}{E_{z,Au}}\right|$. By plotting near-field spectra as a function of the lateral dipole position, we obtain spectral near-field line scans. The simulated point spectra at the rod extremity and center are shown in Fig. 3.5b (red and blue points in Fig. 3.5c, respectively), while the spectral line scan along the antenna axis is displayed along the antenna axis is displayed in Fig. 3.5a,d. Our model can thus be applied for a combined experimental and theoretical in-depth analysis of FP resonances in linear-h-BN antennas.

Simulation details

We performed the numerical calculations using a finite element method (COMSOL). The AFM tip as modelled by a vertically oriented point dipole source. Such an approximation takes into account that the elongated tip in the experiment is oriented perpendicular (vertical) to the sample and is illuminated by *p*-polarized light. We approximate the signal detected in the far field by the vertical component of the electric field, E_z, below the dipole. By scanning the dipole parallel to the substrate and above the h-BN resonators at a fixed frequency and recording E_z below the dipole, we simulate the near-field images. In contrast, the near-field spectra are calculated by changing the frequency and maintaining the dipole at the same position. The simulated near-field spectra are normalized to the spectra above the gold substrate, $\frac{E_z}{E_{z,Au}}$, analogously to the experimental data treatment. For calculations of the spectral line scan shown in Fig. 3.5e, the electric field below the dipole is recorded as a function of both frequency and position of the dipole. In all simulations, the height of the dipole above the antenna was fixed to 300 nm, and the vertical component of the electric field was recorded 15 nm above the antenna surface.

3.5.1 Results

For studying the dispersion $\omega(q)$ of the HP mode yielding the longitudinal Fabry-Perot resonances, we extracted from both the experimental (Fig. 3.5d) and simulated spectral line scans (Fig. 3.5e) the HP wavevector q_n at the resonance frequency ω_n of the longitudinal n-th order mode. The wavevectors q_n are parallel to the longitudinal axis of the antenna (y-axis) and to the atomic layers of

3.5 Dispersion analysis of the resonating mode

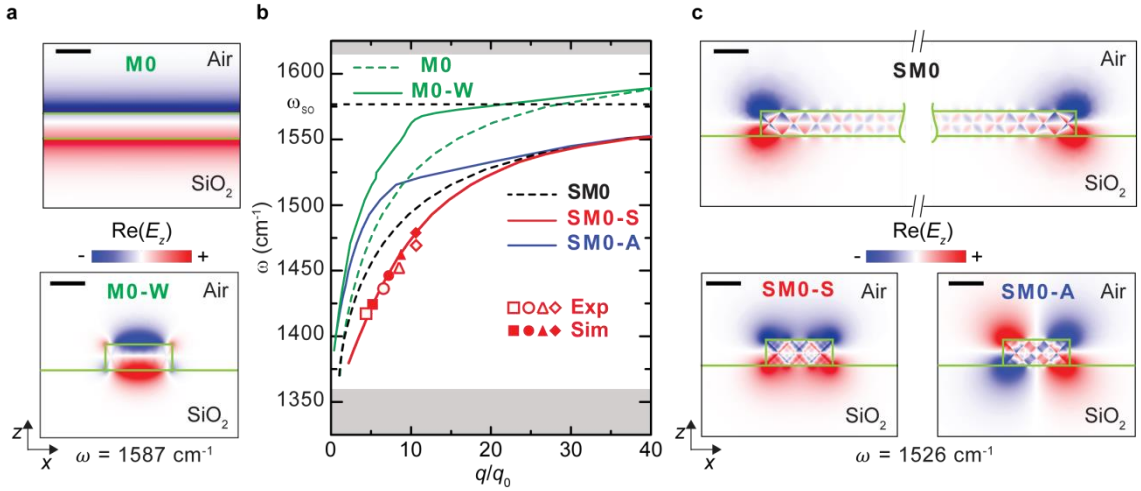

Figure 3.6: Dispersion and near-field distribution of hyperbolic phonon polaritons in h-BN slabs and waveguides. (a) Near-field distribution of the HVM mode of a slab (M0), and of a rectangular waveguide (M0-W). **(b)** Dispersion curves of HVMs (green solid and dashed lines) and HSMs (black dashed line (SM0), and red and blue solid lines (SM0-S and SM0-A)). The experimental (open symbols) and calculated (solid symbols) data points (q_n, ω_n) were extracted from Fig. 3.5d,e, respectively. The different symbols represent the data obtained from the different resonance orders n. The horizontal axis is normalized to the momentum of light in free space, q_0. The white area marks the Reststrahlen band. The horizontal black dashed line indicates the asymptote for surface modes (ω_{SO}). **(c)** Near-field distribution of the fundamental surface mode of a semi-infinite slab (SM0), the symmetric surface mode (SM0-S) and the antisymmetric surface mode (SM0-A) of a rectangular waveguide. The width and height of the rectangular waveguide are 190 nm and 74 nm, respectively. The height of the slab is 74 nm. Scale bars, 100 nm **(a,c).**

the h-BN slab out of which the antennas were fabricated. They are calculated using the relation $q_n = \pi/L_n$, where L_n is the distance between the adjacent maxima in the central part of the antenna (for each resonance order $n > 2$). Fig. 3.6b shows the dispersion obtained from experiment (filled symbols) and simulation (open symbols). We observe that (i) the wavevector q is significantly increased compared to that of free-space photons of the same energy, q_0, and (ii) strongly increases with frequency. Both findings indicate that highly confined waveguide polaritons are the cause of the longitudinal Fabry-Perot resonances. To identify the waveguide mode, we performed a numerical quasi-eigenmode analysis of an infinitely long h-BN waveguide (as described in Section 3.5.2) which has a cross-section that is

identical to that of the antenna (using the same dimensions as in Section 3.4). As expected for hyperbolic material waveguides[147], we found a variety of coexisting waveguide modes. The mode with the smallest wavevectors (mode profile M0-W in Fig. 3.6a; green solid line in Fig. 3.6b) can be identified as the fundamental volume-confined HP mode. Indeed, at large wavevectors its dispersion curve converges to that of volume-confined HPs in an infinite h-BN slab of the same thickness (mode profile M0 in Fig. 3.6a, green dashed line in Fig. 3.6b). Because of the strong discrepancy of the M0-W dispersion curve with the data points (symbols), we can exclude that this mode is observed in the h-BN antennas. Our mode analysis also reveals modes with larger wavevectors and symmetric and antisymmetric spatial distribution of the vertical component of the electric field, $\mathrm{Re}(E_z)$ (mode profiles SM0-S and the SM0-A in Fig. 3.6c; solid red and blue dispersion curves in Fig. 3.6b). Interestingly, the dispersion curve of the SM0-S mode matches perfectly the measured data points (symbols), which let us conclude that this mode is the root cause of the observed Fabry-Perot resonances in the h-BN antennas.

To elucidate the physical nature of the SM0-S mode, we calculated its dispersion $\omega(q)$ up to wavevectors $q \approx 120\, q_0$. We find that $\omega(q)$ asymptotically approaches the frequency ω_{SO} = 1576 cm^{-1} (horizontal black dashed line in Fig. 3.7b). Interestingly at ω_{SO} the condition $\epsilon_\perp = -1$ is fulfilled, which typically determines the dispersion limit of surface polaritons[140] (see Sections 2.4 and 2.5). We thus conclude that the SM0-S mode is a hyperbolic surface polariton mode (HSM), rather than a hyperbolic volume polariton mode (HVM). Indeed, a uniaxial (layered) material can support surface waves (also called Dyakonov surface waves[133,134]) at the surfaces that are perpendicular to its layers. Particularly, when the material exhibits hyperbolic dispersion, the supported modes are HSPs (or Dyakonov polaritons[108,125,126,134]). This condition is fulfilled at the edges of h-BN antennas (see Section 2.4 and 2.5). Because of the finite thickness of the slabs, however, the hyperbolic surface polaritons propagate along the edges as guided modes (HSM), as we confirmed by s-SNOM imaging of the edges of large h-BN flakes[137]. The dispersion of the lowest guided surface mode in a thin semi-infinite h-BN slab (mode profiles SM0 in Fig. 3.6c) is shown by the dashed black line in Fig. 3.6b. It lies between the SM0-S and SM0-A modes, while sharing the same asymptote at 1576 cm^{-1} (horizontal orange dashed line in Fig. 3.6b). We conclude that the SM0-S and SM0-A modes of the h-BN waveguide are hybridized surface modes (exhibiting symmetric and antisymmetric field distributions, respectively), which result from the electromagnetic coupling of the SM0 mode propagating at the two opposing edges of the h-BN waveguide (see Fig. 3.6c). From the spectral near-field analysis, which is consistent with the full-wave simulations, we can

finally conclude that our h-BN antennas exhibit Fabry-Perot resonances of the SM0-S mode.

We note that the near fields at the tip apex, in principle, can excite any of the modes found in Fig. 3.6. However, in the spectral line scans of Figs. 3.5d,e we only observe the SM0-S mode. We explain this finding by the strong damping of the M0-W mode, which propagates less than one polariton wavelength (see Section 3.7). On the other hand, the SM0-A mode cannot be excited when the tip is scanned along the longitudinal antenna axis, where the field of the SM0-A mode is zero. This mode, however, might be excited and observed in the future by scanning the tip, for example, along one of the long antenna edges.

The spectral line scan has allowed us to observe the resonance peaks giving rise to the Fabry-Perot resonances. However, a single spectral line scan does not provide information about the complete structure of the fields induced in the antenna. To obtain that information we perform, in Section 3.6, single-frequency near-field imaging experiments on the antennas at different frequencies.

3.5.2 Method for mode calculation

To identify the mode giving rise to the resonances of the h-BN antenna (Fig. 3.5), we performed a quasi-normal mode analysis of infinitely long h-BN waveguides. The quasi-normal mode analysis takes into account that hyperbolic phonon polaritons in h-BN are damped and have a strong dispersion. It was performed with the COMSOL mode solver. We consider infinitely long waveguides, which offers two advantages. First, finding the modes in an infinitely long waveguide require only 2D simulations (instead of 3D calculations required for truncated waveguides), which are computationally much less demanding and much less time consuming. Second, analyzing the modes in an infinite waveguide provides a simple and intuitive physical interpretation of the resonances in our antennas (in terms of Fabry-Pèrot resonances of a waveguide mode). Our approach is justified by the excellent agreement between the calculated and experimental dispersion (that we show in Fig. 3.6) as well as between the calculated and experimental mode profiles (that are shown in Fig. 3.8c,d, respectively).

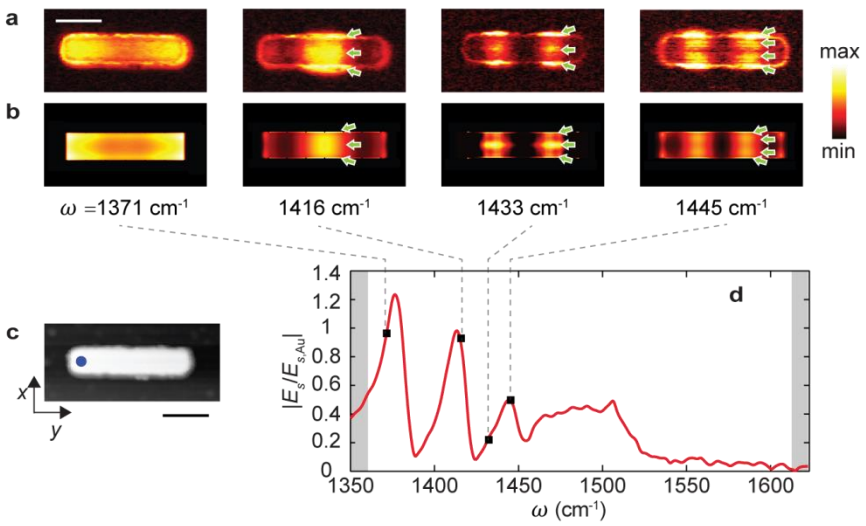

Figure 3.7: Mode mapping of a linear h-BN antenna of 1,220 nm in length. **(a)** Experimental s-SNOM images recorded at frequencies marked by black squares in d. Scale bar, 0.4 μm. **(b)** Simulated s-SNOM images. Green arrows in **a,b** indicate the position of the near-field maxima along the transverse direction. **(c)** AFM topography image of the antenna. Scale bar, 0.4 μm. **(d)** Nano-FTIR spectrum recorded at the position marked by the blue dot in **c**. The white background color indicates the Reststrahlen band. The height of the antenna measured in the AFM was 65 nm, and the average width obtained from the AFM topography was 250 nm.

We further assumed a rectangular cross-section for the h-BN waveguide and thus neglected the slight tilting of the fabricated antenna edges, which is seen in Figure 3.3a. It is justified for the following reasons: (i) we obtained mode dispersions and mode profiles in good agreement with the experimental results, (ii) in Ref. [148] it has been shown that tilted edges have no significant influence in the optical response of hyperbolic structures and (iii) the rectangular cross-section facilitates the discussion, interpretation and understanding of the modes.

3.6 Near-Field imaging of h-BN antennas

In the previous section we have demonstrated that, among the many modes sustained by a hyperbolic waveguide, the measured Fabry-Perot resonances arise

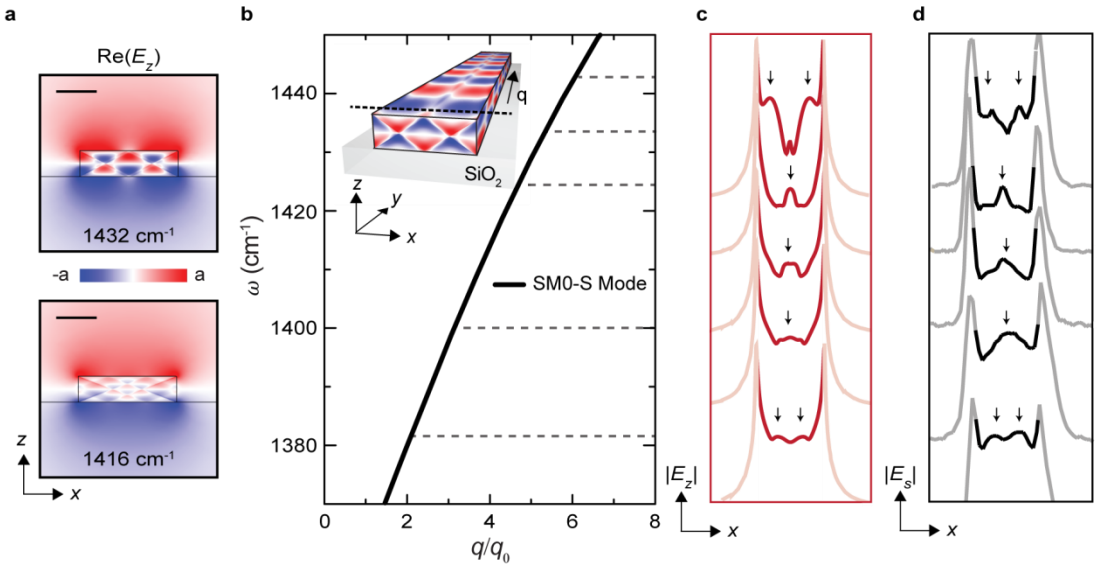

Figure 3.8: Analysis of the SM0-S mode of a rectangular waveguide of 250nm width and 65 nm thickness. (a) Simulated near-field distribution, Re(E_z), of the SM0-S mode at 1,445cm^{-1} (top) and 1,416 cm^{-1} (bottom). Scale bar, 100nm **(a)**. **(b)** Calculated dispersion of the SM0-S mode. The inset shows the schematics of the waveguide and the near-field distribution of the SM0-S mode at 1,445 cm^{-1}. The dashed line indicates the direction of the near-field profiles in c,d**. (c)** Calculated near-field profile of |E_z| in a height of 5 nm above the waveguide surface of the waveguide at 1,445, 1,432, 1,424, 1,400 and 1,381 cm^{-1} (from top to bottom) **(d)** Experimental near-field profiles measured at 1,443, 1,432, 1,424, 1,416 and 1,408 cm^{-1} (from top to bottom). For better visibility of the near-field variations, we plot the central part of the near-field profiles in **b,c** in darker color. For a better comparison of calculated and experimental near-field profiles in **c,d**, we mark local near-field maxima by black arrows.

due to a single hyperbolic surface mode, the SM0-S mode. We gain further insights into the Fabry-Perot resonances by studying both near-field spectrum and near-field images of a shorter h-BN rod antenna (Fig. 3.7). The topography of the rod with the length of 1220 nm is shown in Fig. 3.7c.

The near-field spectrum (recorded at the position marked by a dot in Fig. 3.7c) again reveals several peaks (Fig. 3.7d). They correspond to the different longitudinal resonance orders, which are readily identified with the help of the experimental (Fig. 3.7a) and simulated(Fig. 3.7b, matching well the experiment) near-field images. With increasing frequency, we clearly observe an increasing number n of near-field signal maxima along the antenna, corresponding to the

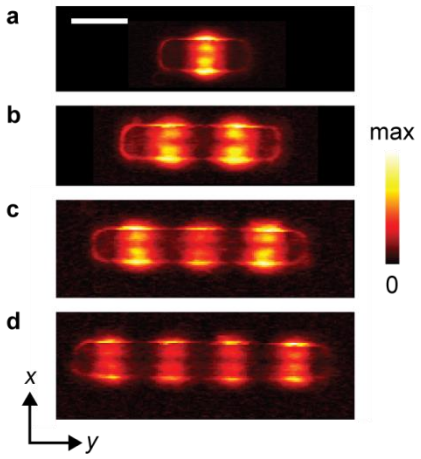

Figure 3.9: s-SNOM images of a set of linear h-BN antennas of a different length, L. Imaging frequency $\omega = 1{,}432$ cm^{-1}. The width and thickness of each antenna (according to the AFM topography images) are 230 nm and 64 nm, respectively. **(a)** L = 746 nm. **(b)** L = 1,327 nm. **(c)** L = 1,713 nm. **(d)** L = 2,210 nm. Scale bar, 500 nm.

$(n-1)$-th resonance order of the SM0-S mode (note that the maxima at the rod extremities are weak, similar to electron energy loss spectroscopy images[132,135]). Surprisingly, we also observe near-field signal oscillations in the transversal direction (marked by green arrows in Fig. 3.7a and 3.7b), which have no analogue in conventional plasmonic antennas. Their periodicity is much shorter than the wavelength of the SM0-S mode, which lets us exclude transverse polariton resonances. We further note that the number of transverse near-field signal maxima does not match the number of near-field signal maxima in longitudinal direction. For example, the third-order longitudinal antenna resonance exhibits both three and four transverse near-field signal maxima at 1433 and 1445 cm^{-1}, respectively.

In Fig. 3.8 we elucidate the origin of the transverse structure of the antenna mode by numerically analyzing the SM0-S mode of the corresponding h-BN waveguide (dispersion shown in Fig. 3.8b). To that end, we plot the calculated transverse near-field profiles (5 nm above the surface of the waveguide) at different frequencies (Fig. 3.8c) and compare them with experimental s-SNOM profiles (Fig. 3.8d, extracted from near-field images such as the ones shown in Fig. 3.7a). The calculations of the line profiles were made at frequencies slightly different from those corresponding to the experimental line scans (the frequencies are indicated in the corresponding figure caption) to match the experiment and theory due to the

uncertainty in the width and height of the antenna, which strongly affects the profile of the mode. An excellent agreement is observed. Particularly, we find that the number of transverse near-field signal maxima does not monotonously increase with increasing frequency. We clarify this observation by plotting in Fig. 3.8a the simulated near-field profile of the SM0-S mode, $\mathrm{Re}(E_z)$, at two different frequencies. Inside the h-BN waveguide, we recognize "zig-zag" patterns. They manifest HP rays that emerge from corners[83,121,136] and reflect at the top and bottom h-BN waveguide surfaces[149], as explained in detail in Section 2.3. As the propagation angle θ of the hyperbolic rays depends on the frequency ω (given by[145] $\tan\theta\,(\omega) = i\sqrt{(\epsilon_\perp\,(\omega)}/\sqrt{\epsilon_\parallel\,(\omega)}$), the multiple reflections yield complex and frequency-dependent field distributions inside the waveguide, which extend several nanometers above the top waveguide surface. Scanning the tip in close proximity across the top waveguide surface (perpendicular to the longitudinal waveguide axis) thus leads to the transversal near-field oscillations observed in Fig. 3.7c (marked by green arrows). On the other hand, in Fig. 3.8a we observe a rather homogeneous near-field distribution at distances larger than 100 nm both above the top waveguide surface and below the bottom surface. Its structure (opposite sign of the vertical component of the electric field above and below the waveguide) does not change with frequency, thus revealing that the different near-field profiles shown in Figs. 3.8ca belong to one and the same waveguide mode. Strikingly, our results demonstrate that the transverse near-field structure of one specific hyperbolic waveguide mode (here the SM0-S mode) can exhibit significant variations upon frequency change.

Finally, we performed near-field imaging of differently long antennas of the same width and height (Fig. 3.9). With increasing antenna length *L*, the images (all recorded at $\omega = 1432$ cm^{-1}) exhibit an increasing number of near-field signal maxima along the antenna, revealing the different resonance orders. Importantly, the transverse near-field profile is identical for all antennas (up to 2.25 μm in length), confirming that the exotic transverse near-field profile of the SM0-S mode is a robust and intrinsic feature of the waveguide mode, and not affected by the antenna length.

3.7 Conclusions

We have employed real-space infrared nanoimaging and nanospectroscopy for studying Fabry-Perot resonances of hyperbolic phonon polaritons in h-BN linear antennas. We found resonances exhibiting Q-factors up to 100, which make the antennas interesting building blocks for the development of infrared molecular sensors, narrowband thermal emitters or metasurfaces for flat infrared photonic elements. By a detailed mode analysis we demonstrate that the waveguide mode exhibiting Fabry-Perot resonances originates from the hybridization of hyperbolic surface modes that propagate along the edges of the h-BN antennas (respectively the h-BN waveguides). This mode exhibits a stronger field confinement (i.e. larger wavevector) compared to the waveguides′ volume modes (of the same order). We have also analyzed the properties of the volume modes, and presented a general overview of the modes present in h-BN waveguides and antennas. From a general perspective, our results provide valuable insights into the fundamental properties of polariton modes in deeply subwavelength-scale linear waveguides based on naturally or artificially layered materials, such as van der Waals materials and vdW heterostructures or metal-dielectric metamaterials. The knowledge about the mode properties will be of critical importance for the development of photonic circuits based on hyperbolic polaritons in linear waveguides and antennas.

4. Deeply subwavelength photonic crystal made of a van der Waals material

In this chapter, we study and engineer a nanoscale hole array in a van der Waals material (h-BN) supporting ultra-confined phonon polaritons (PhPs) – atomic lattice vibrations coupled to electromagnetic fields. Such a hole array represents a polaritonic crystal for mid-infrared frequencies having a unit cell volume of $10^{-5}\ \lambda_0^3$*, with* λ_0 *being the free-space wavelength, where PhPs form ultra-confined Bloch modes, with a remarkably flat dispersion band. The latter leads to both angle- and polarization-independent sharp Bragg resonances, as verified by both far-field spectroscopy and near-field optical microscopy. Our findings could lead to novel miniaturized angle- and polarization-independent infrared narrow-band couplers, absorbers and thermal emitters based on van der Waals materials. This chapter essentially presents the results published in the article "Deeply subwavelength photonic crystal made of a van der Waals material" F.J. Alfaro-Mozaz et al, Nat. Comms. (2019) 10 (1), 42.*

4.1 Introduction

Photonic crystals (PCs) offer the possibility to manipulate the optical modes with small volumes for enhancing light-matter interactions in numerous opto-electronic technologies and quantum optical devices, and for controlling the spontaneous emission rate of local emitters[150,151]. At mid-infrared frequencies PCs find uses as thermal emitters and optical couplers[152] for chemical and biological spectroscopy applications[153] and environmental monitoring (e.g., gas sensing)[154]. They are normally fabricated by either patterning Si slabs[155] or metal layers[156] that are combined with quantum wells operating at the desired wavelength. In both cases the value of the refractive index of the supported electromagnetic modes, n, is rather low (e.g. n~3 for Si) thus, restricting the confinement of light and putting limitations to the dimension of PCs and potential PC-based integrated circuits (for example, room-temperature IR subwavelength photodetectors[157,158]).

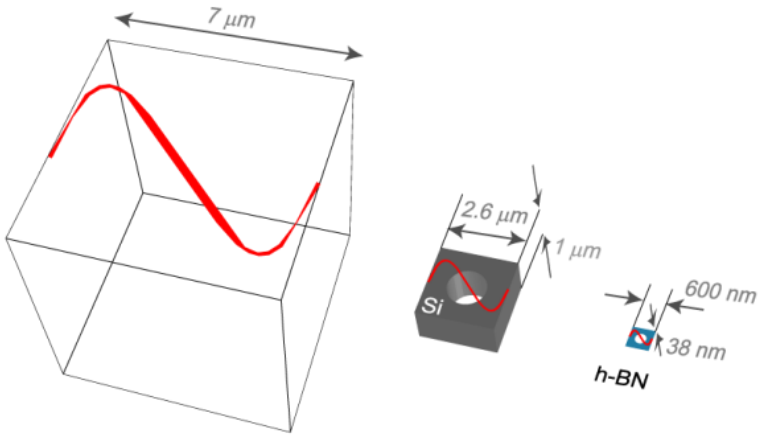

Figure 4.1: Comparison of unit cells sizes. From left to right, the free-space wavelength cube, the typical dimensions of a photonic crystal made of silicon in the mid-IR, and the dimensions of the h-BN polaritonic crystal studied in this chapter.

Low n also implies a steep dispersion of the PC modes (close to the light cone), leading to a broadening of the resonances in IR PCs and an angle-dependent absorption/emission[156]. The confinement of the electromagnetic modes can be improved by means of polaritons –dipolar excitations coupled to electromagnetic fields[140].

Structured thin films of doped semiconductors[28,159] and graphene[16,17], supporting plasmon polaritons, or polar dielectrics (such as SiO_2, Al_2O_3 or SiC[16,150-153]), supporting phonon polaritons (PhPs) can be seen as *polaritonic crystals*[117] – lattices with a spatial period comparable to the polariton wavelength. However, the intrinsic losses of these materials are relatively high (the quality factor Q of the resonances are limited to 30), with the exception of SiC slabs (where PhPs have long lifetimes)[151-153], whose fabrication face substantial practical difficulties.

Promising alternative materials for IR polaritonic crystals can be found among many newly emerging low-dimensional van der Waals (vdW) crystals that support a diversity of polaritons with unique properties (enormous confinement, tunability, low losses, or negative phase velocity, among others), having a large interest for nanophotonics[154,155]. Particularly, as discussed in Chapters 2 and 3 of this thesis, in the mid-infrared frequency range, hexagonal boron nitride crystals present anisotropic phonon resonances and support Type I ($\mathrm{Re}(\varepsilon_z) < 0$, $\mathrm{Re}(\varepsilon_{x,y}) > 0$) and Type II ($\mathrm{Re}(\varepsilon_z) > 0$, $\mathrm{Re}(\varepsilon_{x,y}) < 0$) hyperbolic phonon polaritons (HPhPs)

inside the lower and upper Reststrahlen bands, respectively[28,120]. In h-BN slabs, HPhPs propagate in the form of waveguide modes (HVM) Mn, with $n = 0,1,2,...$,[28,87,110,120] with both their wavelength and propagation length decreasing with n. Due to their remarkably long lifetimes[87,96], HPhPs in h-BN can be used for molecular vibration spectroscopy and strong coupling[160]. Moreover, the preparation of thin h-BN films is a well-established process as well as its structuring into cones[145], rods[97] and stripes[160], in which HPhPs exhibit sharp Fabry-Perot –cavity- resonances. Despite these promising initial works, periodically structured h-BN films in which HPhPs can built collective modes have not been considered yet, so that until now the concept of a h-BN PhP crystal has remained unexplored (although h-BN-based conventional PC have been demonstrated at the visible frequencies, where HPhPs are not supported[161]).

In this chapter we propose, design, and fabricate a mid-infrared polaritonic crystal formed by a rectangular hole array (HA) in a thin h-BN flake (See Fig. 4.1). The chapter is organized as follows. In section 2, we describe the fabrication process of the hole arrays. In section 3 we perform mid-infrared spectroscopy and we reveal narrow geometrically-tunable Bragg resonances. In section 4, we perform nanoimaging experiments on the polaritonic array at the resonance peak to visualize the highly confined Bloch modes. We calculate the band structure of the polaritonic crystal in section 5 finding that the first Bragg resonance is associated with an extremely flat polaritonic band formed by highly confined (deeply subwavelength) Bloch modes. The findings in section 5 are confirmed by the analytical description of the polaritonic array made in section 6 and lead us to prove experimentally and numerically that the Bragg resonances in the polaritonic crystal are angle (and polarization) independent in section 7. The characteristics of the first Bragg resonance are further studied as a function of the structural parameters in section 8. Finally, the long lifetime of the Bragg resonances is discussed in section 9.

The smallness of our vdW polaritonic crystal –the whole polaritonic crystal can fit in a single period of a wave on free space (Figure 4.1)– goes far beyond the original concept by Yablonovich[162] and enables generalization of all the PC-based photonics to a deeply subwavelength scale.

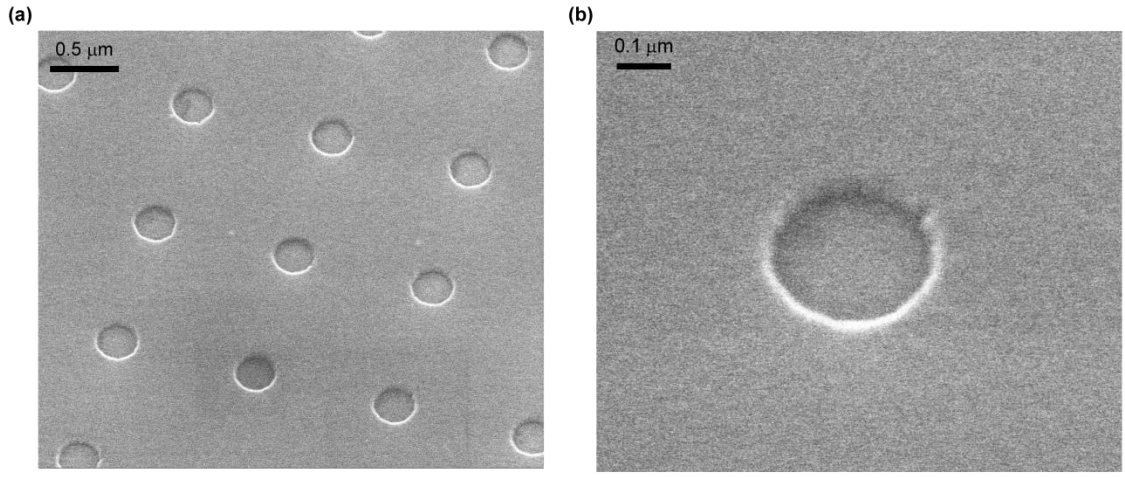

Figure 4.2: **Environmental scanning electron microscope (eSEM) images of a hole array with period L = 1050 nm.** The images show **(a)** the regularity of the fabricated array and **(b)** the precise lithography of a single hole.

4.2 Fabrication of the polaritonic crystals

The fabrication of the antennas were performed by Irene Dolado and Saül Vélez at CIC NanoGUNE BRTA.

The polaritonic crystal consists in a square array of holes patterned in an h-BN thin film flake. We fabricated hole arrays by patterning h-BN flakes via electron beam lithography. In order to obtain large and homogenous h-BN crystals flakes, we first performed mechanical exfoliation of commercially available h-BN crystals (HQ graphene Co, N2A1) using blue Nitto tape (Nitto Denko Co., SPV 224P). Afterwards, the flakes attached to the tape were exfoliated onto several polydimethylsiloxane stamps. The stamps were inspected using an optical microscope and large and homogeneous h-BN flakes (with a thickness of t = 38 nm) were identified and transferred onto a transparent CaF_2 substrate using the deterministic dry transfer technique[163].

We patterned the arrays of holes using high resolution electron beam lithography. The sizes of the arrays were 15 x 15 μm, with a fixed hole diameter (300 nm) and periodicities L between 0.6 and 1.2 μm, being thus about one order of magnitude smaller than the illuminating wavelength and consequently exhibiting an ultra-small volume of the unit ell of about $10^{-5}\lambda_0^3$.

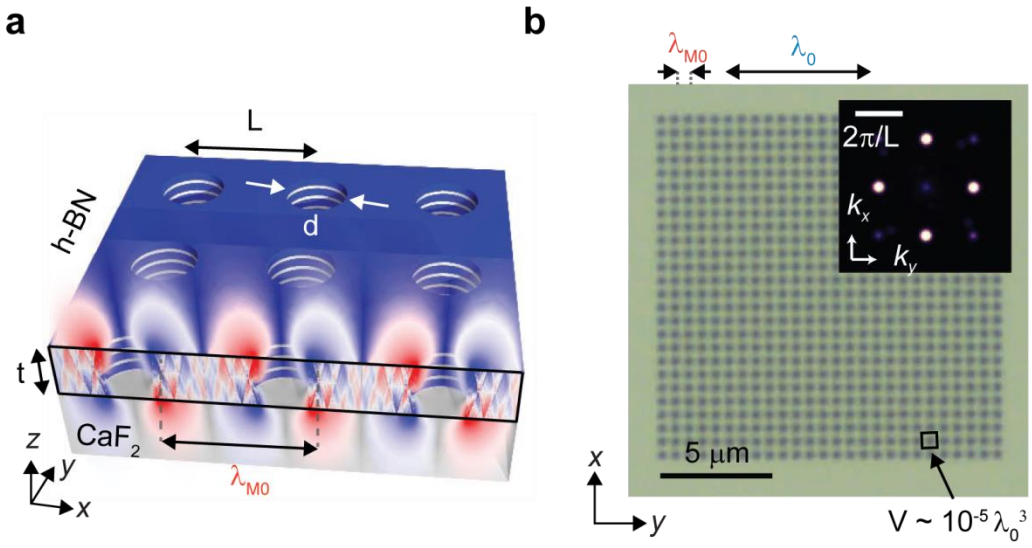

Figure 4.3: Geometry of the polaritonic crystals. (a) Schematics of a hole array in a h-BN slab with thickness t = 38 nm on CaF_2 substrate. **(b)** Optical image of a hole array with period L = 600 nm. The arrows represent the wavelength of light in free space, λ_0, and that of the M0 mode, λ_{M0}, respectively. The inset shows the Fourier transform of the optical image.

To that end, we used a single layer polymethyl methacrylate (PMMA) 495 A4 resist as an electron sensitive resist. The desired holes were written with the electron beam and developed in MIBK:IPA 1:3, resulting in a patterned PMMA layer that is used as a mask to protect the h-BN areas underneath during the etching process. The uncovered h-BN areas were chemically etched in a SF6/Ar 1:1 plasma mixture at 20 sccm flow, 100 mTorr pressure and 100 W power for 60 s (RIE OXFORD PLASMALAB 80 PLUS reactive ion etcher). Finally, the sample was immersed in acetone for several hours for removing the PMMA mask, rinsed in IPA and dried with a N_2 gun.

To ensure the proper fabrication quality of the hole arrays, we imaged them by means of atomic force microscope (AFM) (performed simultaneously with the optical near-field imaging). environmental scanning electron microscopy (eSEM, Fig. 4.2), and optical microscopy (Fig. 4.3b). The Fourier transform (FT, inset of Fig. 4.3b) has prominent sharp peaks at $\vec{k} = (\pm G, 0)$ and $\vec{k} = (0, \pm G)$ with $G = 2\pi/L$, as expected for a square lattice.

4.3 Spectroscopic analysis of the polaritonic crystals

The schematic of the polaritonic crystal (square array of circular holes with diameter $d = 300\,\text{nm}$) considered in this chapter is shown in Fig. 4.3a. The polaritonic crystals are designed to exhibit HPhP resonances at mid-IR frequencies (1360-1480 cm^{-1}). To optically characterize the polaritonic crystals, we performed Fourier-transform infrared spectroscopy (FTIR) experiments using non-polarized thermal radiation, under normal incidence, as described in details in section 4.3.1.

4.3.1 FTIR Setup

Microspectroscopy transmission spectra of the h-BN polaritonic crystals are recorded with a Bruker Hyperion 2000 infrared microscope coupled to a Bruker Vertex 70 FTIR spectrometer. The polarized infrared beam from the interferometer is focused through the Swartzchild lens 1 providing waves with incident angles ranging from $\theta_1 = 9.8º$ to $\theta_2 = 23.8º$. Albeit there is a range of incidence angles, it can be approximated by a normal incidence beam in our experiments. The beam is focused onto the h-BN hole array. The transmitted light is then refocused by the Swartzchild lens 2 that sends the beam to the detector. The spectral resolution was 1 cm^{-1}. The area covered by the IR beam was around 10x10 μm^2. By using a stage we can rotate the sample along the XY and XZ axis. The stage can rotate the sample from -40º to 40º in the XZ axis. It allowed recording transmission spectra of linearly polarized light.

4.3.2 Spectroscopic analysis

The transmission spectra, T/T_{CaF_2}, are shown in Fig. 4.5a (color curves) together with the spectrum obtained for a bare h-BN slab (black curve). Apart of a strong dip corresponding to the h-BN TO phonon ($\omega_{TO} = 1366\ \text{cm}^{-1}$), the spectra of the

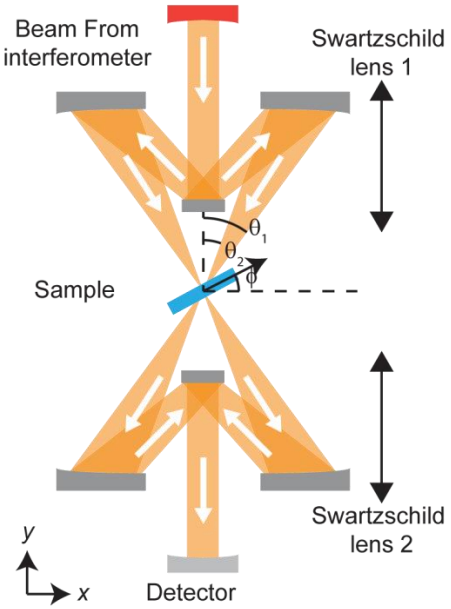

Figure 4.4: Schematics of the FTIR spectrometer in transmission mode.

polaritonic crystals show sharp dips (with an estimated Q-factor of 190) at larger frequencies, revealing a clear dependence upon L. To better analyze this result, the spectral positions of both the TO phonon dip (squares) and period-dependent dip (circles), together with the numerically simulated transmission spectra $T/T_{\mathrm{CaF_2}}$ as a function of both L and ω, are plotted in Fig. 4.5b. The experimental results are corroborated with full-wave simulations of the transmission spectra, made by a finite element method (COMSOL). In both experiment and theory, we observe that while the minima at the h-BN TO dip is not affected by the periodic structuring, the frequency of the second dip strongly decreases with increasing L. Remarkably, according to the simulations, the value of the absorption in the second peak (Fig. 4.5c) is comparable to that of the TO phonon absorption peak, revealing the high coupling efficiency provided by the HA. These results demonstrate that the transmission dips in the spectra of our deeply subwavelength polaritonic crystals can be tuned by L, in a similar fashion to the *geometrical* plasmonic resonances in metallic hole arrays at visible frequencies[117], the latter however having significantly lower Q-factors (by a factor of 10).

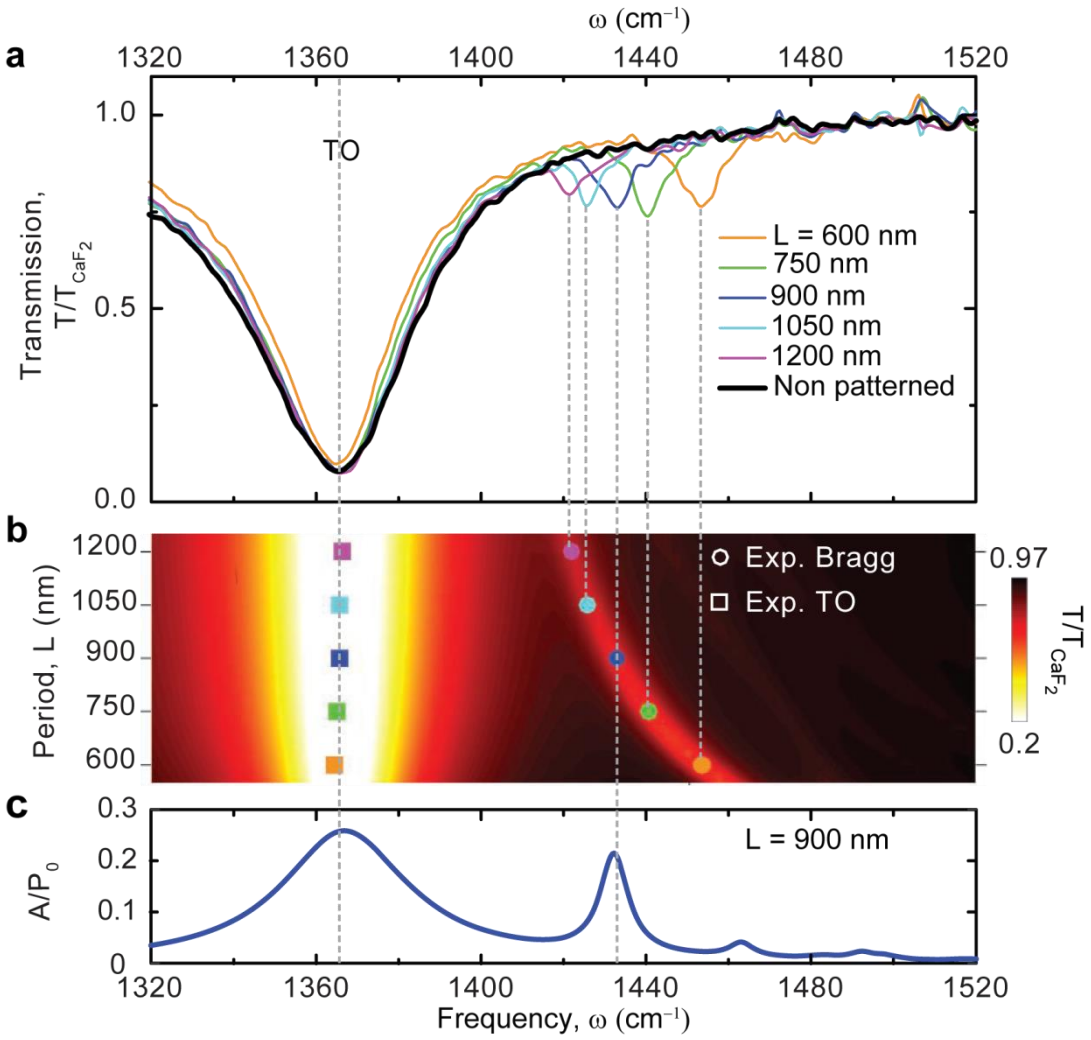

Figure 4.5: Spectroscopic analysis of h-BN polaritonic crystals **(a)** Experimental normalized transmission spectra for the hole arrays with L ranging from 600 to 1200 nm. **(b)** Simulated transmission as a function of frequency and L (colormap). The points indicate the position of the dips from the experimental spectra. **(c)** Simulated absorption spectra of the hole array with $L = 900$ nm [-1].

To understand the origin of period-dependent transmission dips in our polaritonic crystals, we simulated the field snapshot, $\mathrm{Re}[E_z(x,z)]$ (Fig. 4.3a) at the wavelength of the dip minimum for $L = 900$ nm. A *zigzag* ray pattern in the slab region (x-z plane) is observed, evidencing the excitation of many HVM modes with different wavelengths at the edges of the holes[82,87,160]. However, the field distribution outside of the slab is very different, as we see field oscillations with a single period (alternating red and blue lobes). The period of the oscillations

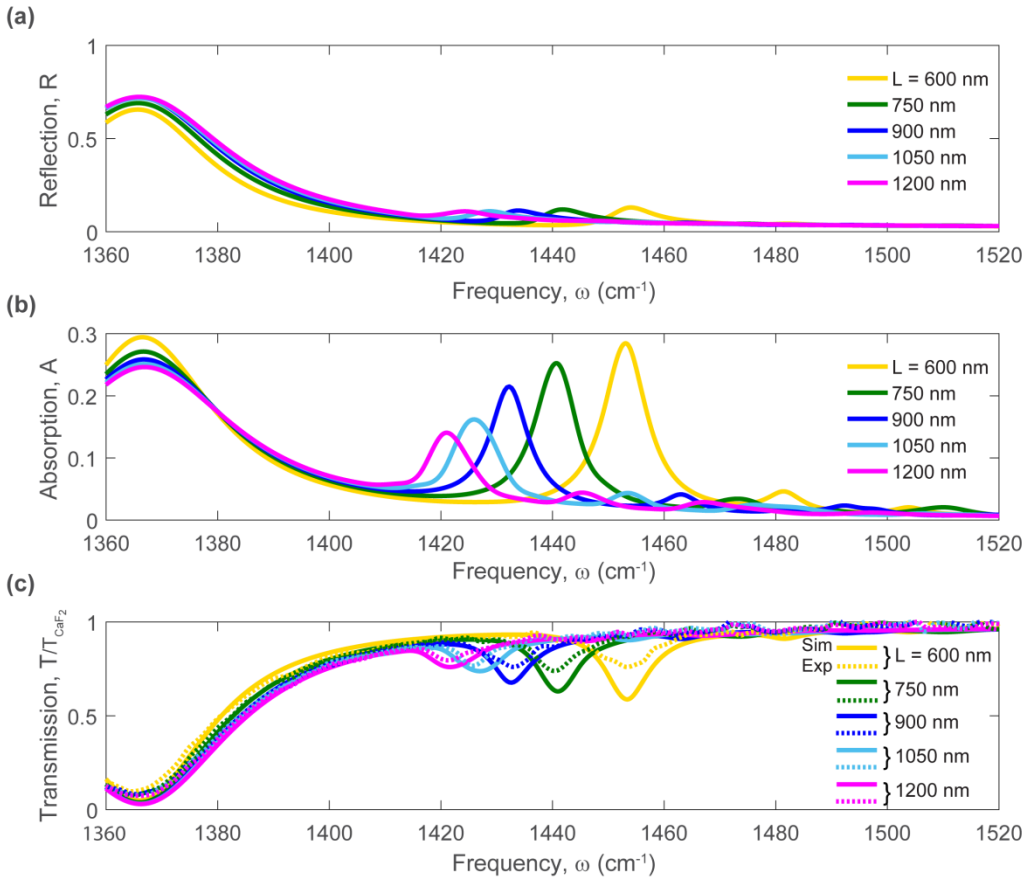

Figure 4.6: Transmission, absorption and reflection coefficients. (a) Reflection, **(b)** absorption and **(c)** transmission coefficients for the fabricated hole arrays shown in the main manuscript. The dashed (solid) lines correspond to the experiment (simulations).

matches with the wavelength of the HVM M0 mode (found from the mode dispersion[5]), and the nodes are located at the center of the holes. The field distribution thus resembles that of a standing wave, which permits us to identify the period-dependent dip in the polaritonic crystal transmission spectra as the first-order Bragg resonance of a HVM M0 mode.

We complete the spectroscopic analysis by a detailed study of the transmission, absorption and reflection coefficients of the considered hole arrays. The data is shown in Figure 4.6. The calculated reflection coefficient is about 10% at frequencies close to the first Bragg resonance for all the fabricated hole arrays. On

the other hand, the absorption at the first Bragg resonance frequency, that is comparable to that of the TO phonon (at ω = 1366 cm^{-1}), increases with decreasing the period, L, of the hole array. The simulated transmission spectra show an excellent agreement with the experiment in terms of spectral position, while the depth of the experimental peaks is slightly smaller than in the calculated ones. The latter discrepancy can be explained by the small aperture used in the spectrometer and the finite size of the hole array in the experiment.

4.4. Near-field imaging at the resonance peak

We employ near-field imaging to experimentally observe the electric field distribution in the polaritonic crystal at the measured (Figure 4.5) resonance peak. The near-field distribution, corroborated by with full-wave simulations, corresponds to that of the first order Bloch resonance.

4.4.1 Experimental setup

We used an s-SNOM microscope from Neaspec Gmbh (Munich). It is based on an atomic force microscope (AFM). Conventional dielectric (silicon) tips acted as scattering near-field probes. In contrast to a metallic tip (typically acting as both polariton launcher and near-field scatterer[71,72]) a dielectric tip acts as a weak scatterer. It does not launch any polaritonic mode, but only scatters the near-fields that are generated on the sample by the incident laser beam[161,162]. The laser beam was generated by a Quantum Cascade Laser (QCL, tunable ω =1,295–1,445 cm^{-1}, Daylight Solutions, USA) and focused to the tip apex using a parabolic mirror. The polarization of the illuminating beam in the presented experiments was parallel to the h-BN surface (s-polarization) and we recorded the out-of-plane near-field component, E_z (p-polarization)[164]. The near fields scattered by the silicon tip were collected with the same parabolic mirror and recorded simultaneously with the sample topography. Background contributions were suppressed by vertical tip oscillation at frequency $\Omega \approx 300$ kHz (tapping-mode AFM) and by subsequent higher harmonic demodulation of the detector signal at 4Ω. The modulation amplitude of the tip was around 100 nm.

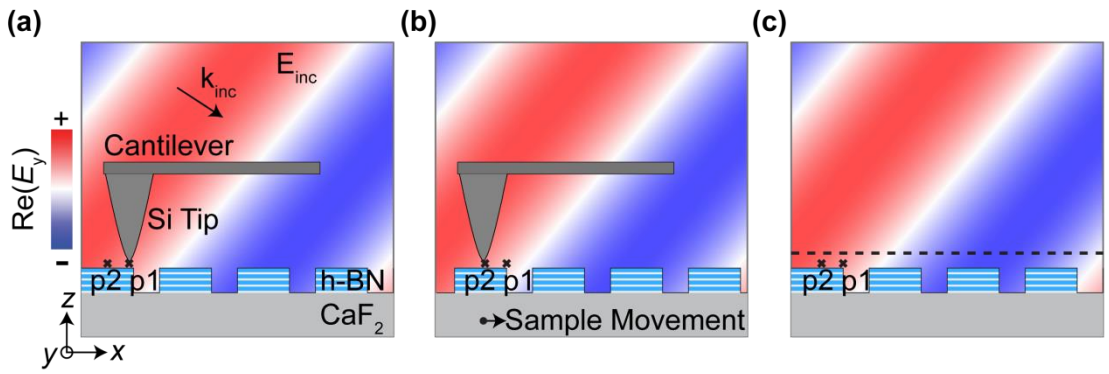

Figure 4.7: Schematics of the illumination of the sample in the s-SNOM. (a) The tip probes the point p1, and the phase of the illuminating wave is ϕ_{back}. **(b)** The tip probes the point p2, and the phase of the illuminating wave is ϕ_{back}. **(c)** In the simulation, the illuminating phase of points p1 and p2 is different $\phi_{back,p1} \neq \phi_{back,p2}$. The dashed line indicates the height at which the field is calculated in the simulation.

The amplitude and phase of the near-field components were measured with a pseudo-heterodyne detection module[165]. In the s-SNOM used in the experiment, the tip (the probe point) does not move relative to the illuminating field. Instead, the stage in which the sample is located moves relative to the background field (see Figure 4.7), in such a way that, at the measuring position, the phase of the background field is fixed.

4.4.2 Simulation of the near-field images

We model the near-field images by using a finite element method (COMSOL). The simulations were performed within one unit cell, with periodic conditions matching the illuminating wavelength wavevector. We illuminate the hole array with a plane wave at a 50º angle with respect to the normal, similar to the near-field imaging experiment, and then extract the simulated near-field distribution above the hole. In the simulation, given that the incident field is oblique, there is field retardation between each point of the sample: every point of the polaritonic crystal surface is illuminated with an electric field with a different phase (Figure 4.7c). However, as explained in Section 4.4.1, in the experiment, the tip position (the point where the near-field is probed) does not move with respect to the background (see Figure 4.7a,b where the tip position and illuminating background are fixed while the sample moves in the x-

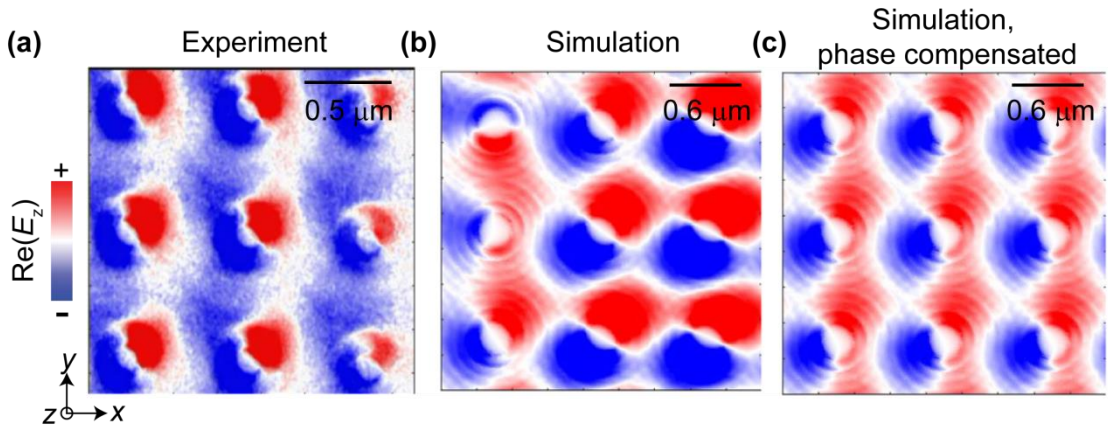

Figure 4.8: Comparison of **(a)** the experimental image with the simulated near-field distributions, **(b)** without, and **(c)** with phase compensation.

direction). Due to that, the experimental image is different from the simulated image (Figure 4.8 a and b, respectively). We compensate this difference between the images by doing the following transformation on the simulated map of the vertical component of the electric field, $E_{\mathrm{z,com}}(x,y)$:

$$E_{\mathrm{z,com}}(x,y) = E_{\mathrm{z,sim}}(x,y) \cdot \exp\left(k_{\mathrm{x,inc}} \cdot x + k_{\mathrm{y,inc}} \cdot y\right). \qquad (4.1)$$

Here, $E_{\mathrm{z,com}}(\mathrm{x,y})$ is the vertical component of the simulated near field accounting for the phase compensation. $E_{\mathrm{z,sim}}(\mathrm{x,y})$ is the vertical component of the simulated near field, and $k_{\mathrm{x,inc}}$ and $k_{\mathrm{y,inc}}$ are the wavevector in-plane components of the background field. By using equation (4.1), we transform the simulated near-field distribution in Figure 4.8b and obtain an excellent agreement (Figure 4.8c) with the experimental near-field image (Figure 4.8a).

4.4.3 Near-field analysis

In Section 4.3 we identified that the resonances in the transmission spectra are due to the first order Bragg resonance of the M0 mode. To provide more insight into the field structure at the resonance, we image the near-field distribution on top of the hole array by s-SNOM, using a weakly scattering Si tip illuminated by an *s*-polarized obliquely incident light (see schematics in Fig. 4.9a) as a probe and recording the scattered *p*-pol radiation, E_s, (as explained in Section 4.4.1). The near-field image (the real part of the signal, E_s) obtained at the frequency of the transmission dip (1428 cm^{-1}, dark blue curvein Fig. 4.5a) is shown in Fig. 4.9b. We

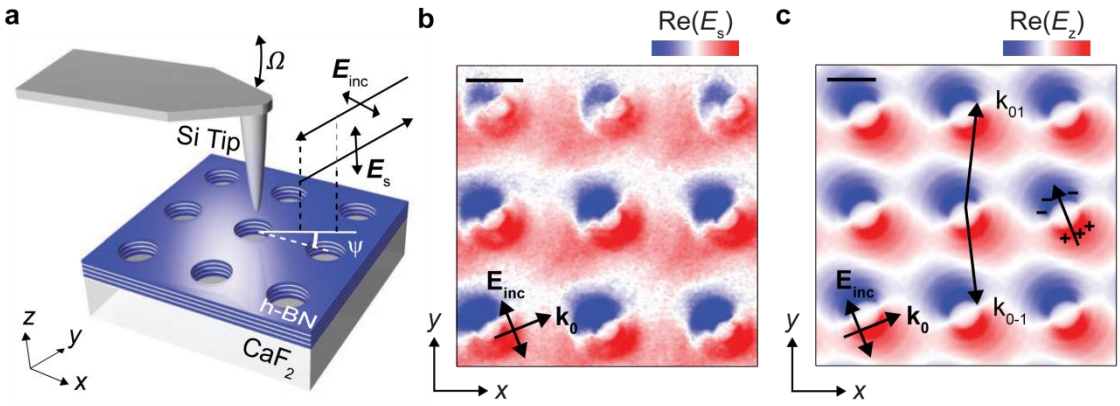

Figure 4.9: Near-field imaging of a Bloch mode in the h-BN polaritonic crystal. (**a**), Schematics of the experiment. (**b**), experimental near-field image. (**c**) Simulated field snapshot of the polaritonic crystal with L = 900 nm at the resonant frequency 1428 cm^{-1}. Black arrows indicate the direction of the electric field, E_{inc}, and in-plane wave vector of the incident wave, $\mathbf{k}_0$. The effective induced dipole and the k-vectors of (0,1) and (0,-1) diffraction orders constituting the Bloch mode are indicated in (c) by the black arrows. Scale bars in **(b,c)**: 450 nm.

see field oscillations with the opposite polarities (red and blue colors) that match the period L of the polaritonic crystal, thus revealing the spatial field structure of the HPhP M0 Bloch mode in the y-direction.

The slight rotation of the observed field pattern is attributed to the illumination used in our experiment (the plane of incidence is rotated by the angle ψ with respect to one of the HA's translation vectors), which together with the effective electric dipoles induced by the holes also allows for exciting a Bloch mode in the x-direction. We corroborate this experimental result by simulating a snapshot of $\mathrm{Re}[E_z(x,y)]$ (Fig. 4.9c) assuming a similar illumination scheme (both angle and polarization) as in the experiment. A perfect matching between experiment and simulation validates our near-field characterization using a Si tip, which permits to identify the deeply subwavelength Bloch mode excited in the first-order Bragg resonance of the polaritonic crystal. Notice that the imaging of the Bloch modes outside of the light cone (not excited via the far-field) with the Si tip is not possible. Alternatively, these modes can be accessed via polariton interferometry with s-SNOM[34], which uses metallic tips and allows for the *local* excitation of the highly-confined fields. However, the polaritonic interferometric s-SNOM imaging would require the back-reflection of the Bloch mode from edges or other discontinuities in

the polaritonic crystal and thus would strongly complicate the interpretation of the near-field images.

4.5 Band structure of the polaritonic crystal

In this section we study the excitation of the Bloch modes in the polaritonic crystal for large wave vectors, thus extending the scope of previous sections –focused on the normal or near-normal incidence–. For that, we obtain the band structure of the M0 HPhP Bloch modes in the hole array with a period L = 0.9 μm using Finite Difference in Time Domain (FDTD) simulations. We also calculate the isofrequency contours at the frequencies of interest using a Finite Element Method, and we compare it with the transmission spectra of the crystal to identify the polaritonic branch giving rise to the transmission dips in the spectra.

4.5.1 Methods for band structure calculations

We used the FDTD method to simulate the HPhP band structure of the polaritonic crystal. We set up periodic Bloch conditions at the boundaries of the unit cell. Uniaxial perfect matched layers were imposed at surfaces of the cell parallel to the h-BN film. We use mesh element sizes ranging from 2 to 5 nm. The dielectric constant in cells at the h-BN-substrate and h-BN-superstrate interfaces is taken as that of the medium with the largest volume inside that particular cell. The band structure is calculated by exciting the system with a superposition of randomly placed and oriented electric dipoles (to allow the excitation of modes with all possible symmetries), and imposing Bloch's theorem at the boundaries of the unit cell. Then the value of the amplitude of the electric fields for different Bloch phase factors (wave-vector) and frequencies is calculated, revealing the band-structure of the HA. By changing the position of the dipoles, either outside of the HA (Fig. 4.10a) or inside the holes of the HA (Fig. 4.10b), we are able to efficiently excite bands with lower energy (Fig. 4.10c) or higher energy (Fig. 4.10d) allowing to track the modes of the hole array.

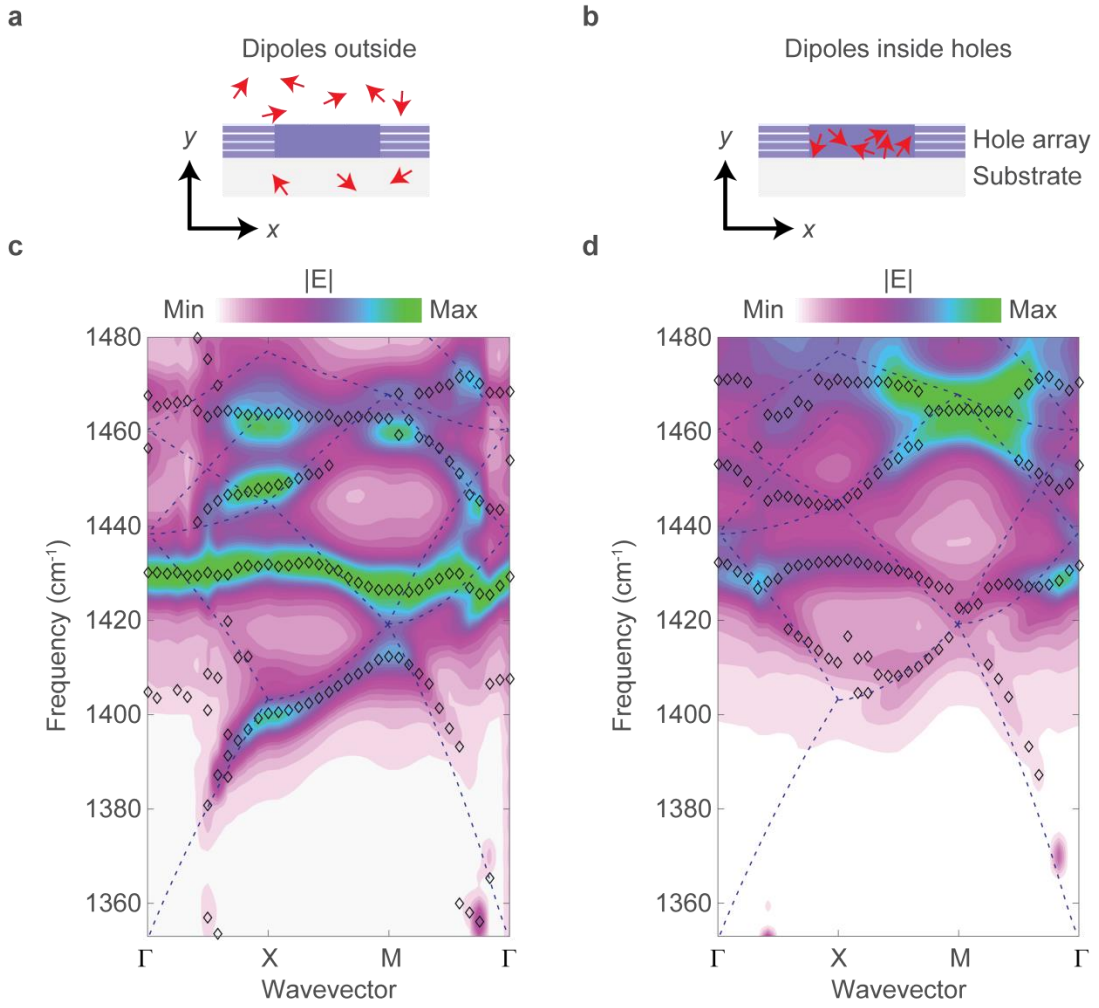

Figure 4.10: Calculated polaritonic band structure of the polaritonic crystal by different illumination distribution. L = 900 nm. Sketch of a unit cell of the hole array illuminated with the dipole sources placed in: **(a)** outside of the hole array, and **(b)** inside the holes. The electric field probes are similarly distributed in **(a)** and **(b)**. **(c)** and **(d)** shows the band structure obtained by measuring the intensity of the electric field (colorplot) when the sources are placed according to **(a)** and **(b)**, respectively. The dashed lines in **(c,d)** correspond to the dispersion of the M0 mode in the h-BN layer. The rhomb symbols in **(c)** and **(d)** represent the position of maxima in the field intensity averaged over the h-BN unit cell.

We calculated the isofrequency surfaces of the hole array by FEM calculations. We placed a single dipole over the structure and calculated the radial electric field induced by the dipole in the hole array, $E_{\rho,\mathrm{h-BN}}(x,y)$. The same calculation was done removing the h-BN film from the structure, obtaining the distribution of the

field above the substrate, $E_{\rho,\mathrm{sub}}(x,y)$. Then, Fourier transform of the subtracted fields, $\mathrm{E}_{\rho,\mathrm{h-BN}}(x,y) - E_{\rho,\mathrm{sub}}(x,y)$, was performed, obtaining $E_\rho(k_\mathrm{x},k_\mathrm{y})$. To mimic the source with the electric field fulfilling the Bloch's theorem, the following summation over different Brillouin Zones have been performed: $\sum_{\mathrm{n,m}} E_\rho(k_\mathrm{x} + \mathrm{n}\cdot \mathrm{G}, k_\mathrm{y} + \mathrm{m}\cdot \mathrm{G})$. This procedure is equivalent to the monitoring the field (satisfying the Bloch's theorem) at the position $(x = 0, y = 0)$. The isofrequency surfaces $E_\rho(k_\mathrm{x},k_\mathrm{y})$ allow us to see, at a given frequency ω, the wavevector of the modes sustained by the polaritonic crystal.

4.5.2 Band structure results

Fig. 4.11a shows the calculated band structure of the polaritonic crystal with $L = 900$ nm, along the main directions $\Gamma - X - M - \Gamma$ in the first Brillouin zone. One can recognize features reminiscent to the folded dispersion curves for M0 HPhP in a continuous h-BN slab[5] (Fig. 4.11a, the blue dashed lines). At momenta, where the folded dispersion curves for the continuous slab intersect (*e.g.* in the vicinity of the M-point at $\omega = 1420$ cm^{-1}), partial band gaps open, prohibiting the propagation of the M0 mode in the polaritonic crystal. Note that in conventional photonic crystals, the band structure is mainly formed in the region of propagating waves, $k \leq \omega/c$. Conversely, the major part of the band structure in our polaritonic crystal is formed outside of the light cone, $k > \omega/c$ (Fig. 4.11a, vertical dashed vertical lines), thus covering mainly the region of the evanescent waves in free space with high in-plane momenta. We complement the band structure by the Fourier transforms (FTs) of the simulated fields emitted by a vertical point dipole above the HA – counterparts of the isofrequency contours (ICs), see Section 4.5.1 –, illustrated in Fig. 4.11c. Such FTs implicitly provide the information on the density of polaritonic modes in the k-space. At low frequencies the ICs show a circular shape (Fig. 4.11c, bottom), similar to the bare ICs of the continuous slab, $k_x^2 + k_y^2 = k_{M0}^2$ (Fig. 4.11d, bottom), so that at low momenta the density of Bloch polaritonic modes is zero and the light does not couple to the polaritonic crystal (no maxima in the difference transmission signal, ΔT, Fig. 4.11b). Oppositely, at the frequency of the Bragg resonance, the ICs show a high density of Bloch modes in a large area of the Brillouin zone (Fig. 4.11c, top), and particularly in the whole area of the light cone (black circle, Fig. 4.11c,d). The high density of modes is consistent with

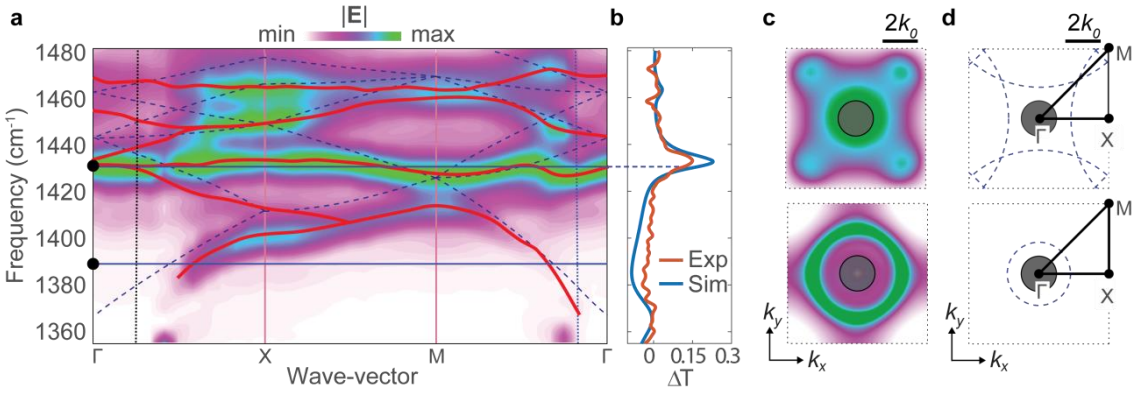

Figure 4.11: Band structure of hyperbolic phonon polaritons in the h-BN polaritonic crystal. (**a**) Simulated band structure of the polaritonic crystal. The colorplot renders the amplitude of the electric field generated by the dipoles, averaged over the unit cell of the array (Section 4.5.1). The blue dashed lines trace the folded dispersion curve of the HVM M0 mode in a continuous h-BN slab. The horizontal blue lines mark the frequencies of the plots in (**c,d**). The red curves trace the maxima in various colorplots (generated for different positions and orientations of the dipole sources). (**b**) Experimental (blue) and calculated (red) normalized transmission spectra. (**c),** Calculated isofrequency plot at ω = 1388.8 cm^{-1} (top) and 1432 cm^{-1} (bottom) for the HA with $L = 900$ nm. **(d)** Bare isofrequency contours (dashed blue lines). In (**c,d**) the black circles represent the light cone, while the dotted black squares represent the first Brillouin zone. Scale bars in **(c,d)**: $2k_0$.

the band-structure of Fig. 4.11a, where a nearly k-independent band for the whole range of momenta is formed around $\omega = 1428\ \mathrm{cm}^{-1}$. Such flat polaritonic band can find uses in ultraslow light[166,167] and near-field radiative thermal transport[167,168] at deeply subwavelength scale. Remarkably, the flat band indicates that the coupling to the polaritonic crystal by an incident plane wave can happen for *any in-plane momenta* (see the maximum in the difference transmission spectra, ΔT, Fig. 4.11b), and thus for any incident angle, θ (related to the momentum as $k_x = k_0 \sin\theta$). This finding will be further explored analytically and experimentally in next sections.

4.6 Analytical analysis of the polaritonic Bloch modes and Bragg resonances

The band structure calculations have unveiled the angle-independent HPhP Bragg resonance of the polaritonic crystal. In this section, we provide an analytical

description of the resonances, based on the resonance perturbation theory[64-66], which allows us to link the angle-independent absorption peaks with the field structure of the modes, and to further predict the properties of the crystal upon variation of the geometric parameters.

In order to simplify the analysis, we approximate the thin h-BN film by a 2D conductivity layer (Appendix A). Furthermore, we will approximate the hole array by a 1D periodic structure modulation, considering that the excited HPhP modes correspond to the standing waves along one direction. We discuss the general formulation of the problem (Section 4.6.1) as well as an analytical derivation of the amplitudes of the modes excited by a normal incident plane wave in Section 4.6.2. Finally, in Section 4.6.3 we compare the results of the analytical model with the full-wave simulations.

4.6.1 General Formulation

To analytically treat the diffraction of the electromagnetic wave by the polaritonic crystal, we approximate the thin h-BN slab by a 2D conductivity layer, following Appendix A. We assume that the conductivity layer is placed between two dielectric half-spaces with the dielectric permittivities ε_1 (for $z > 0$) and ε_2 (for $z < 0$), respectively, as depicted in Figure 4.12. The hole array can be seen as spatially (and periodically) modulated[74] effective conductivity, α, and thus we will consider a general periodic structure with an arbitrary spatial Fourier spectrum. For simplicity, we restrict ourselves to considering the incident plane wave with the in-plane electric field component parallel to one of the translation vectors of the hole array (aligned along x- and y-axes, according to the chosen system of coordinates). In this case the excited Bloch modes will be predominantly standing waves along x- or y-directions. Neglecting the weak interaction between the standing waves excited in the perpendicular directions[118], we can approximate the hole array by two perpendicular one-dimensional (1D) periodic gratings and consider each grating independently. Without loss of generality, let us study the 1D periodic modulation of the conductivity along the x-direction (Figure 4.12).

The periodically modulated effective conductivity can be written as (for convenience of the equations writing, we introduce the normalized conductivity[74], α, as $\alpha = 2\pi\sigma_{\mathrm{eff}}/c$)

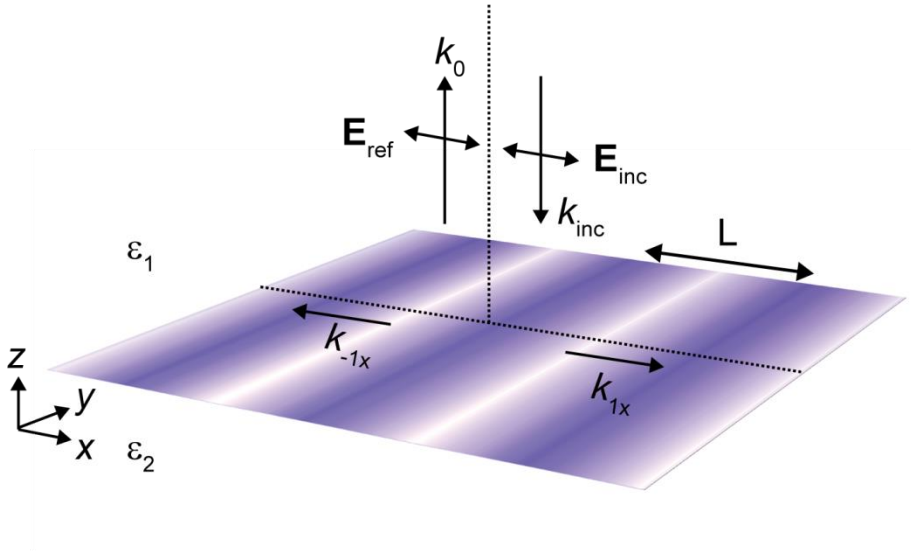

Figure 4.12: Sketch of a periodically-modulated conductivity layer. The conductivity varies in the x-direction. The linearly-polarized incident plane wave impinges the layer at normal incidence, exciting mainly field harmonics with the k-vectors k_{-1x} and k_{1x} (first-order diffracted waves).

$$\alpha(x) = \alpha(x + L) = \sum_n \alpha_n e^{inGx}, \qquad (4.2)$$

with $G = \frac{2\pi}{L}$ being the reciprocal grating vector, n an integer and α_n the n-th Fourier harmonic of the normalized effective conductivity. The in-plane component of the electric fields in the superstrate (labelled as "1") and substrate (labelled as "2") can be taken in the form of the Fourier-Floquet expansion:

$$\mathrm{E_{1x}} = \mathrm{e^{ik_x x - ik_z z}} + \sum_n \mathrm{r_n e^{ik_{nx} x + ik_{1nz} z}}, \qquad (4.3)$$

$$\mathrm{E_{2x}} = \sum_n \mathrm{t_n e^{ik_{nx} x - ik_{2nz} z}}, \qquad (4.4)$$

where $k_{nx} = k_x + nG$ and $k_{1,2nz} = \sqrt{\varepsilon_{1,2} k_0^2 - k_{nx}^2}$ are the x- and z-components of the wave-vectors for the diffracted (scattered) plane waves and $k_0 = \omega/c$ is the k-vector in free space. The coefficients $\mathrm{r_n}$ and $\mathrm{t_n}$ are the amplitudes of the spatial Fourier harmonics (waves diffracted in the nth order) in the upper and lower half-spaces, respectively.

4. Deeply subwavelength photonic crystal made of a van der Waals material

Using Maxwell's equations, $\boldsymbol{H} = (1/ik_0)\nabla \times \boldsymbol{E}$, we can find the y-component of the magnetic fields in the substrate and superstrate. Then, we match the fields at the conductivity layer (z = 0) according to the boundary conditions

$$\mathbf{e}_z \times [\mathbf{H}_1 - \mathbf{H}_2] = 2\alpha \cdot \mathbf{e}_z \times [\mathbf{e}_z \times \mathbf{E}_1],$$

$$\mathbf{e}_z \times [\mathbf{E}_1 - \mathbf{E}_2] = 0. \qquad (4.5)$$

Using the Fourier series for α(x) in Eq. (4.2), we obtain the linear system of equations for the amplitudes r_n and t_n.

$$e^{ik_x x} + \sum_n (r_n - t_n) e^{ik_{nx} x} = 0,$$

$$-Y_i e^{ik_x x} + \sum_n \left(r_n Y_{1|n} - t_n Y_{2|n}\right) e^{ik_{nx} x} = -2 \sum_{n,m} \overline{\alpha}_m t_n e^{ik_{nx} x}, \qquad (4.6)$$

where $Y_i = \varepsilon_1 k_0 / k_z$ is the admittance (the inverse of the wave impedance[9]) of the incident wave and $Y_{1,2|n} = \varepsilon_{1,2} k_0 / k_{1,2nz}$ are the admittances of the diffracted waves. Taking into account that Eq. (4.6) must hold for any value of x, we have to equal the coefficients at different exponentials. Then we obtain a compact system of equations for the amplitudes t_n:

$$\sum_m D_{nm} t_m = V_n,$$

$$D_{nm} = \delta_{nm}\left(Y_{1|n} + Y_{2|n} + 2\alpha_0\right) + 2\overline{\alpha}_{n-m}, \quad V_n = 2Y_i \delta_{n0}, \quad (4.7)$$

where with δ_{nm} we mean the Kronecker symbol, and $\overline{\alpha}_n$ represents the Fourier harmonic of $\alpha(x)$, given by Eq. (4.2), but with the excluded zero harmonic ($\overline{\alpha}_0 = 0$) The amplitudes, r_n, are related to the amplitudes, t_n, as follows:

$$r_n = -\delta_{n0} + t_n. \qquad (4.8)$$

The *infinite* linear system of equations (4.7) can be solved numerically for any type of periodic function α(x). For each type of modulation, an appropriate *finite* number N of he diffraction orders, n, must be taken into account in order to achieve the convergence of the solution (truncation of the infinite system). In some cases, however (particularly, for periodic modulations with abrupt changes of $\alpha(x)$ as, for example, for a layer structured into ribbons), the convergence with N can be very slow and the system of equations (4.6) becomes unpractical. On the other hand, smooth profiles of $\alpha(x)$, provide a good convergence and the number of required diffraction order is not large, so that even an analytical treatment of the system of equations is possible.

The solution of the system of equations (4.7) can be found also analytically. Assuming small modulation amplitude, we can use the resonance perturbation theory. The main idea of the resonance perturbation theory consists in the retention in the system of equation (4.7) all the resonant field harmonics (harmonics with high amplitudes compared to that of the incident wave), and then the minimal number of non-resonant field harmonics (originating from the lowest-order scattering of the resonant field harmonics by the diffraction grating). The number of the non-resonant field harmonics (and the contributing scattering processes) is selected with respect to the desired precision of the final solution (for more detailed description of the resonance perturbation theory in diffraction problems see Refs. 64,66,169). In the lowest-order approximation, the reduced system for the resonant field harmonics (whose diffraction orders we label by "r") has the following form:

$$\sum_{r'} \widetilde{D}_{rr'} t_{r'} = \widetilde{V}_r,$$

$$\widetilde{D}_{rr'} = \delta_{rr'} b_r + 2\overline{\alpha}_{r-r'} - 4\sum_N \frac{\overline{\alpha}_{r-N}\overline{\alpha}_{N-r'}}{b_N} \quad (4.9),$$

$$\widetilde{V}_r = -4\overline{\alpha}_r \frac{Y_i}{b_0},$$

where, for brevity, we have used the following notation: $b_N = Y_{1|N} + Y_{2|N} + 2\alpha_0$. In the sums of Eq. (4.9) only non-resonant diffraction order harmonics are included (that is the resonant field harmonics with indices r are excluded).

4.6.2 Field distribution of the Bloch modes

Under normal incidence (the incident plane wave has no in-plane momentum component, i.e. $k_x = 0$), and in case of a *symmetric grating profile*, $\overline{\alpha}_m = \overline{\alpha}_{-m}$ the unknown amplitudes in the system of equations (4.7) are symmetric with respect to the diffraction order m, i.e. $r_m = r_{-m}$ and $t_m = t_{-m}$. According to the field representation, Eqs. (4.3) and (4.4), the above symmetry results in the excitation of only cos-like spatial field distributions (for the in-plane electric field) of the Bloch modes: $r_m e^{ik_{mx}x} + r_{-m} e^{-ik_{mx}x} = 2r_m \cos k_{mx}x$. This property of the inhomogeneous system of equations does not however mean that the corresponding homogeneous system of equations (with zero right-hand side) does not have solutions (eigenmodes) with other field distributions.

Let us consider the Bloch wave excited in the First-Order Bragg resonance, experimentally visualized in Section 4.3 and 4.4. To study the Bloch (eigen-) modes, we should consider the system (4.9), but with the right hand side set to 0 (no incident wave). In the latter system we have only two spatial field harmonics with the amplitudes t_1, t_{-1}. It reads as

$$D\mathrm{t}_1 + d\mathrm{t}_{-1} = 0,$$

$$d\mathrm{t}_1 + D\mathrm{t}_{-1} = 0. \quad (4.10)$$

where, for compactness, we have defined $D = \widetilde{\mathrm{D}}_{11} = \widetilde{\mathrm{D}}_{-1-1}$ and $d = \widetilde{\mathrm{D}}_{1-1} = \widetilde{\mathrm{D}}_{-11}$. The eigenfrequencies can be defined by the dispersion relation (when the determinant is set to 0)

$$D^2 - d^2 = 0. \quad (4.11).$$

The roots of Eq. (4.11) (which we label as S and A) can be symbolically written as $D_A = d$, and $D_S = -d$, from which the eigenfrequencies $\omega_{A,S}$ can be found. Substituting the roots back into the system (4.10), we find two solutions for the eigenvectors:

$$\begin{matrix} t_1^{\mathrm{S}} = 1, & t_{-1}^{\mathrm{S}} = 1 \\ t_1^{\mathrm{A}} = 1, & t_{-1}^{\mathrm{A}} = -1, \end{matrix} \quad (4.12)$$

By inserting the two solutions, S and A, in Eqs. (4.3) and (4.4), yield the following in-plane electric field distributions on top of the modulated conductivity layer:

$$E_{\mathrm{x},1}^{\mathrm{S}} \sim \cos(\mathrm{G}x) \quad , \quad E_{\mathrm{x},1}^{\mathrm{A}} \sim \sin(\mathrm{G}x). \quad (4.13)$$

For the out-of-plane electric field component (z-component), we have (consistently with the Maxwell´s equation $\nabla \cdot \boldsymbol{E} = 0$):

$$E_{\mathrm{z},1}^{\mathrm{S}} \sim \sin(\mathrm{G}x), \quad E_{\mathrm{z},1}^{\mathrm{A}} \sim \cos(\mathrm{G}x). \quad (4.14)$$

Therefore, according to the correspondence between Eqs. (4.13) and (4.14), the z-component of the mode excited under the normal incidence (the so-called *bright mode*) is distributed according to $\sin(\mathrm{G}x)$. The other mode, with the vertical electric field distributed according to $\cos(\mathrm{G}x)$ is the so-called *dark mode*.

Notice that this result is confirmed by the near-field experiments (Section 4.4), where the observed standing wave pattern has a zero at the center of the hole, confirming that we indeed excite the *bright mode* of the system.

Interestingly, depending upon the geometrical parameters of the grating (its spatial Fourier spectrum) ω_A can be either larger or smaller than ω_S, so that A is either higher- or lower-frequency mode (with respect to S). This will be explored in Section 4.8.

4.6.3 Comparison of the analytical solution with full-wave simulations

To further corroborate the validity of our analytical approximation developed in Section 4.6.1, we compare the absorption in the polaritonic crystal calculated with the help of full-wave simulations (COMSOL) and the linear system of equations (4.6). For the solution of the system of equations 4.6 we use the expression for the amplitudes of the Fourier harmonics, α_n, corresponding to the holes. As before, we assume that the polaritonic crystal is placed on the CaF_2 substrate. The results of the full-wave simulations and calculations according to Eq. (4.6) are shown in Figure 4.13, demonstrating an excellent agreement between the two approaches (color plots in Figure 4.13c and Figure 4.13d). Apart from the absorption, in Fig. 4.13c,d we also show the dispersion branches of both modes A and S (green and blue curves, respectively). The dispersion curves were obtaining by analyzing the zeros of the determinant of the system of equations (4.6). The mode S (lower frequency branch) perfectly matches with the bright maximum in the colorplots, and shows an almost constant frequency with respect of the angle of incidence.

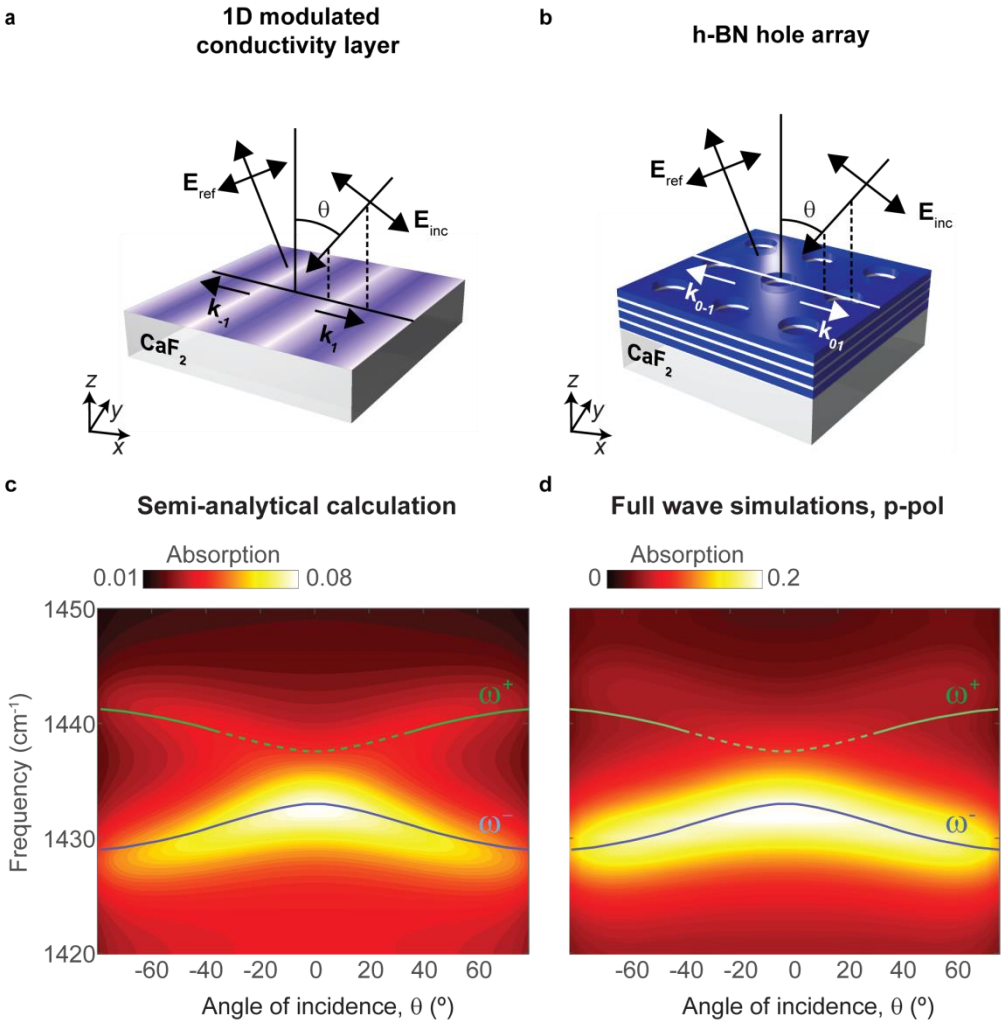

Figure 4.13: Absorption of a *p*-polarized incident plane wave by the h-BN polaritonic crystal, as a function of the angle of incidence and frequency. (a) Schematics of the conductivity layer periodically modulated in one direction, placed on top of a CaF_2 substrate. The incident wave excites the Bloch mode formed by the field harmonics with the *k*-vectors k_{-1} and k_1 (first-order diffracted waves), giving rise to the first-order Bragg resonance. **(b)** Schematics of the polaritonic crystal. The excited Bloch mode is formed by the field harmonics with the *k*-vectors k_{0-1} and k_{01} . The period of both the hole array and the 1D periodic lattice is L = 900 nm. The plane of incidence (marked by white solid line) is parallel to the lattice vector in **(a)** and the rows of holes in **(b)**, respectively. **(c)** and **(d)** show the absorption as the function of θ and ω (colorplots), with the help of the system of equations (4.6) and full-wave simulations, respectively. The blue and green curves represent the dispersion of the modes S and A, respectively.

4.7 Omnidirectional and polarization independent absorption peaks

The band structure calculations provided us hints that the absorption on the system is nearly angle-independent. Moreover, the analytical description of the HPhPs in the hole array further corroborated this observation and allowed us to describe the Bloch modes measured by near-field microscopy (in terms of *symmetric* or *antisymmetric* electric field distributions). In this section, we experimentally prove the omnidirectional absorption of the polaritonic crystal (originating from the almost frequency-independent momenta of the first order Bloch mode). We carry out optical transmission measurements at oblique incidence for both *p*- and *s*-polarization, schematically shown in Figs. 4.14a,d. The measured normalized extinction, $1 - T/T_{\mathrm{CaF_2}}$, as a function of the incident angle, θ, and frequency, ω, is represented in Figs. 4.14b,e. Strikingly, for both polarizations, the extinction maximum is clearly independent upon θ in the whole measured range, thus finding an excellent agreement with the calculated absorption (Figs. 4.14c,f).

The theoretical analysis carried out in Section 4.6 of both symmetric, S, and antisymmetric, A, Bloch modes, allows us to unambiguously attribute such angle-independent Bragg resonance to the excitation of S Bloch modes (Figs. 4.14a,d). Namely, the excited modes S_{y} (*p*-polarization) and S_{x} (*s*-polarization) have a symmetric vertical electric field distribution with respect to the hole centers, $E_{\mathrm{z,S_y}} \sim \sin \mathrm{G}y$ and $E_{\mathrm{z,S_x}} \sim \sin \mathrm{G}x$, respectively. The field distribution of the modes is derived in Section 4.6. This result is also corroborated by the field distribution revealed by our near-field measurements (Fig. 4.9) and is consistent with the previous studies of the plasmonic resonances in metallic hole arrays and gratings[2,37,38], thus generalizing the coupling to the symmetric Bloch modes to a deeply subwavelength polaritonic crystal. Our findings demonstrate both angle and polarization independence of the narrow Bragg resonances in a h-BN polaritonic crystal, making the latter attractive candidates for narrow-band omnidirectional infrared absorbers, couplers and thermal emitters, significantly smaller than those based on conventional bulk materials[46-48].

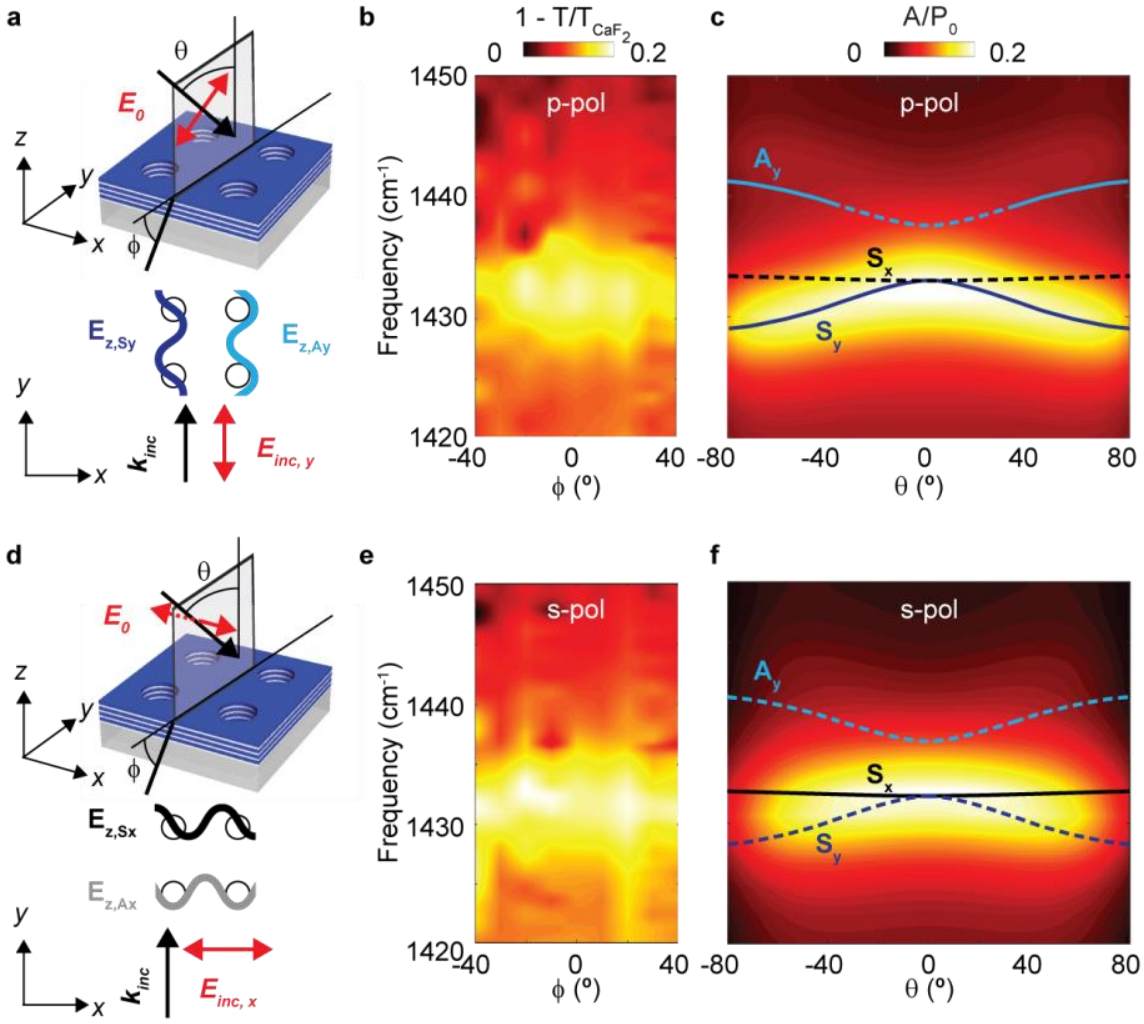

Figure 4.14: Angle- and polarization-independent HPhP Bragg resonance in the h-BN polaritonic crystal. a,d, Top: schematics of the angle-dependent transmission experiments for *p*- and *s*-polarization. Bottom: spatial distribution of the vertical electric field of the Bloch modes in the vicinity of the resonance frequency. **b,e,** Measured normalized extinction, $1 - T/T_{CaF_2}$, as a function of the stage rotation angle, ϕ, and frequency. **c,f,** Calculated normalized absorption as a function of the incident angle, θ, and frequency.

4.8 Tuning the bright and dark Bloch modes

In the previous sections we have derived the dark and bright modes that occur at the first Bragg resonance (Section 4.5 and 4.6) of the polaritonic array, and identified the emerging Bragg resonance by the coupling of the incident wave to the bright mode (Section 4.4). In this section we explore the variation of the polaritonic crystal parameters. We determine which of the two modes (S or A, according to Section 4.6) appears at lower frequencies and quantify the band gap between both modes.

In an explicit form, the Eq. (4.11) can be rewritten as:

$$(\mathrm{b} - 4\Gamma_1)^2 - (2\overline{\alpha}_2 - 4\Gamma_2)^2 = 0, \qquad (4.15)$$

where we have introduced the following notations:

$$b = b_1 = b_{-1},$$

$$\Gamma_1 = \sum_{\mathrm{N}} \frac{\overline{\alpha}_{1-\mathrm{N}}\overline{\alpha}_{\mathrm{N}-1}}{\mathrm{b}_{\mathrm{N}}}, \qquad \Gamma_2 = \sum_{\mathrm{N}} \frac{\overline{\alpha}_{1-\mathrm{N}}\overline{\alpha}_{\mathrm{N}+1}}{\mathrm{b}_{\mathrm{N}}}, \qquad (4.16)$$

where the summation is realized in all the diffraction orders, except 1 and -1, and b is defined as in Section 4.6.1. Let us write the solutions of Eq. (4.15) as $\omega = \omega_0 + \delta\omega$, by introducing a small deviation from the frequency of the polaritons in the unmodulated conductivity layer (with the normalized conductivity α_0), ω_0. The latter frequency follows from the dispersion relation $b(\omega_0) = 0$. This equation (in the large momentum/short lattice period approximation, $G \gg \varepsilon_{1,2}\mathrm{k}_0$, providing under the normal incidence $\mathrm{Y}_{1,2|1} \simeq \varepsilon_{1,2}\mathrm{k}_0/\mathrm{iG}$) yields $\omega_0 = -i\alpha_0 \cdot \frac{2Gc}{\varepsilon_1+\varepsilon_2}$. To explicitly find $\delta\omega$ from Eq. (4.15), we will assume that all the quantities in Eq. (4.16) are taken at $\omega = \omega_0$, except $b(\omega) = b(\omega_0 + \delta\omega)$. By expanding $b(\omega)$, we have:

$$b(\omega) \simeq \mathrm{b}(\omega_0) + \frac{\varepsilon_1+\varepsilon_2}{i\mathrm{Gc}}\delta\omega. \qquad (4.17)$$

From Eq. (4.17) we find the two values for $\delta\omega$:

$$\delta\omega_{A,B} = \frac{i\mathrm{Gc}}{\varepsilon_1+\varepsilon_2}[4\Gamma_1 \pm (2\overline{\alpha}_2 - 4\Gamma_2)]. \quad (4.18)$$

Then the expressions for the eigenfrequencies of the modes A and S become

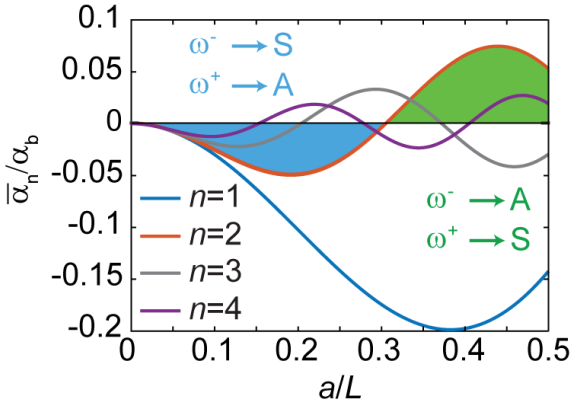

Figure 4.15: Amplitude of the first four Fourier harmonics of the rectangular hole array as a function of the ratio between radius and array period, a/L. The sign of the second harmonic approximately dictates the position of the eigenfrequencies relative to each other.

$$\omega_A = \omega_0 + \frac{4i\mathrm{Gc}}{\varepsilon_1+\varepsilon_2}\Gamma_1 + \Delta\omega,$$

$$\omega_S = \omega_0 + \frac{4i\mathrm{Gc}}{\varepsilon_1+\varepsilon_2}\Gamma_1 - \Delta\omega. \qquad (4.19)$$

with

$$\Delta\omega = \frac{2i\mathrm{Gc}}{\varepsilon_1+\varepsilon_2}(\bar{\alpha}_2 - 2\Gamma_2). \qquad (4.20)$$

We see that both eigenfrequencies are shifted with respect to ω_0 by the term proportional to Γ_1 (the shift of the center of the bandgap). This term is contributed from the second-order scattering processes (*via* non-resonant diffraction orders) between the bare HPhPs given by the resonant diffraction orders 1 and -1. The splitting, defined by $\Delta\omega$, is contributed from both second-order processes (term proportional to Γ_2) and the linear interaction between the bare HPhPs (term proportional to $\bar{\alpha}_2$).

To simplify the analysis of $\Delta\omega$ we neglect the ohmic losses, assuming that the effective conductivity (and its Fourier harmonics) is purely imaginary. We also assume that for a weak modulation, the second-order lattice harmonic, $\bar{\alpha}_2$, exceeds the term $2\Gamma_2$ so that the linear interaction between the bare HPhPs dominates over the second-order scattering. Then according to Eq. (4.20) the sign

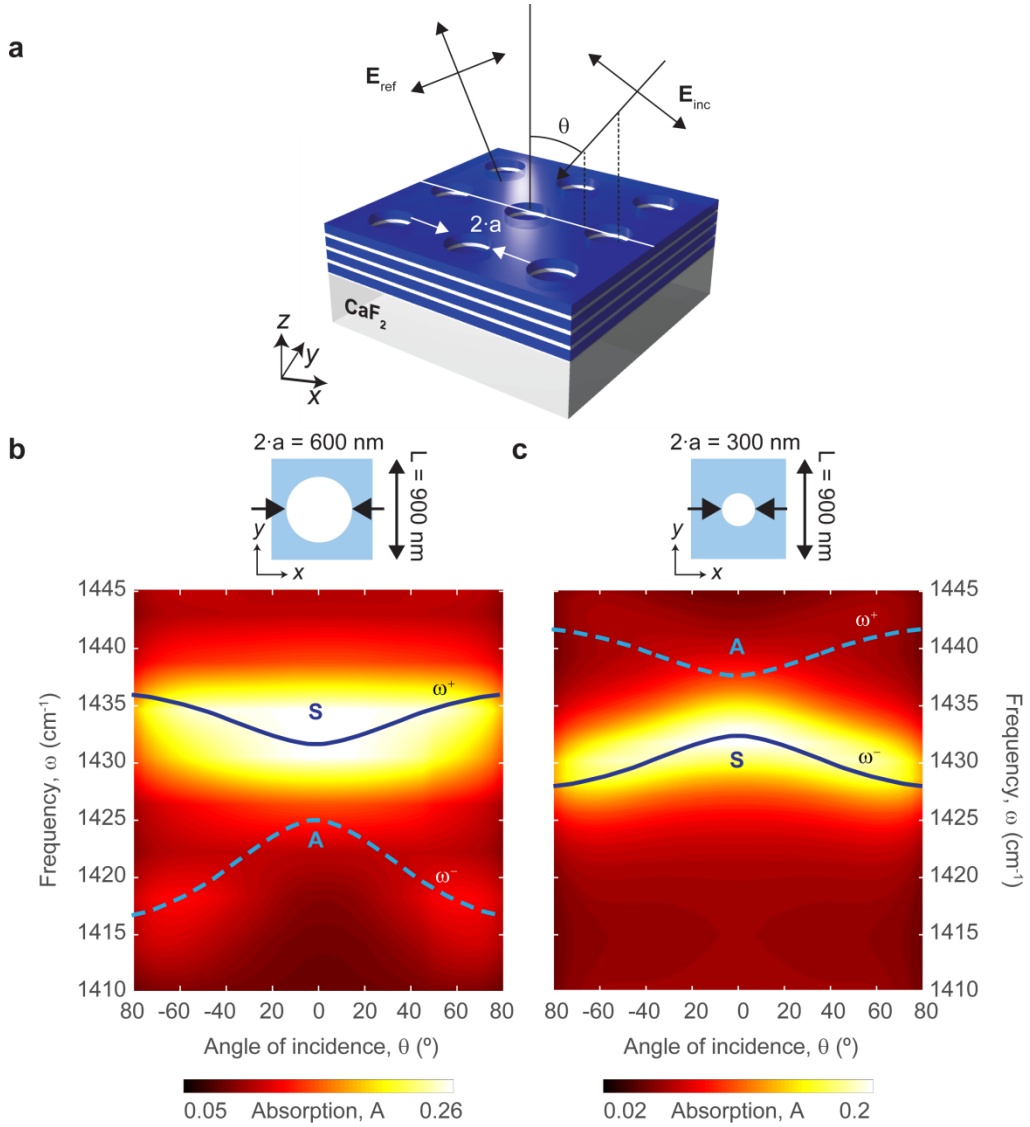

Figure 4.16: Calculated normalized absorption as a function of angle for two different radii of the holes. (a) Sketch of the polaritonic crystal (L = 900 nm) on a CaF_2 substrate. A p-polarized wave impinges the hole arrays with an angle θ with respect to the normal. **(b,c)** Calculated absorption in the hole arrays (colorplot) as a function of θ and ω.The sketches show the relative size of the hole with respect to the unit cell. The solid and dashed lines are guides to the eye, highlighting the position of the bright (S) and dark (A) modes, respectively.

of $\Delta\omega$ is mainly determined by the sign of the second Fourier harmonic of the grating, $\bar{\alpha}_2$, multiplied by the imaginary unit. Namely, when $\text{sign}(i\bar{\alpha}_2) < 0$, the S mode (bright mode) has a higher frequency, "ω^+", while the A mode (dark mode) has a lower frequency, "ω^-". In contrast, when $\text{sign}(i\bar{\alpha}_2) > 0$, the S mode (bright

mode) has a lower frequency, "ω^-", while the A mode (dark mode) has a higher frequency, "ω^+". Taking into account that the imaginary part of the normalized effective conductivity of the unmodulated layer, α_b, is positive, the condition of $\text{sign}(i\bar{\alpha}_2) > 0$ ($\text{sign}(i\bar{\alpha}_2) < 0$) is equivalent to $\text{sign}(\bar{\alpha}_2/\alpha_b) < 0$ ($\text{sign}(\bar{\alpha}_2/\alpha_b) > 0$), respectively (we remind here that we are neglecting the losses).

In order to apply the results of our approximate analysis directly to the case of the hole array, let us write the modulation of the normalized effective conductivity of the hole array as $\alpha(x,y) = [1 - f(x,y)] \cdot \alpha_b$, where f takes 1 (0) value inside (outside) of the holes, respectively. The Fourier transform of $f(x,y)$ in case of a rectangular array (with period L) of circular holes (with radius a) is $f_{n,m} = \frac{a}{L}\frac{1}{\sqrt{n^2+m^2}}J_1(2\pi\frac{a}{L}\sqrt{n^2+m^2})$, with J_1

being the Bessel Function of the first kind. The spectrum of the 1D grating, equivalent to the hole array can be obtained from the 2D Fourier harmonics of the normalized effective conductivity, $\bar{\alpha}_{n,m}$, by setting $\bar{\alpha}_n = \bar{\alpha}_{n,0}$. It reads:

$$\frac{\bar{\alpha}_n}{\alpha_b} = -\frac{a}{L}\frac{1}{n}J_1(2\pi\frac{a}{L}n). \qquad (4.21)$$

When the diameter of the hole changes, the weight of the second harmonic of the Fourier decomposition of the hole array varies (see Figure 4.16). According to our approximation, in the range of $a/L < 0.3$ (where $\text{sign}(\bar{\alpha}_2/\alpha_b) < 0$), the modes S and A are expected to have low (ω^-) and high (ω^+) frequencies, respectively (blue region in Figure 4.15). In contrast, for $a/L > 0.3$ ($\text{sign}(\bar{\alpha}_2/\alpha_b) > 0$), the modes S and A should have high (ω^+) and low (ω^-) frequencies, respectively (green region in Figure 4.16).

We verify the results of our analytical analysis by performing the full-wave simulations (COMSOL) for the two hole arrays (placed on CaF_2 substrate) with radii of holes $a = 300$, and 150 nm (Figs. 4.16a,b), and period $L = 900$ nm. The parameters of the arrays have been chosen in such a way that the arrays with the smallest and largest a correspond to the blue and green areas in 4.15. The simulated absorption, as a function of frequency, ω, and angle of incidence, θ, is shown in Figure 4.16. For the hole array with $a = 300$ nm ($a/L = 0.33$) we have $\text{sign}(\bar{\alpha}_2/\alpha_b) > 0$ (blue region in Fig. 4.15) and as predicted above, the bright mode S has a higher frequency than the dark mode A. In contrast, for the hole array with $a = 150$ nm ($a/L = 0.167$) we have $\text{sign}(\bar{\alpha}_2/\alpha_b) < 0$ (blue region in 4.15) and the bright mode S has a lower frequency than the dark mode A. As seen in the colorplots of Fig 4.16b and c, for the oblique incidence the incident wave breaks the symmetry and both A and S modes are excited (this is clearly seen for angles

$\theta > 20^o$). Thus, the numeric simulations corroborate our analytical results, revealing the key role of the second harmonic of the hole array in the relative frequency position of the Bloch modes in the first-order Bragg resonance.

The results of our analysis are consistent with previous studies for one- and two-dimensional metallic diffraction gratings and hole arrays in metal films, although these studies were limited to the periods comparable to the free-space wavelength in both cases[170-172].

4.9 Lifetime of the Bloch modes excited in the first-order Bragg resonance

By spectroscopic measurements (reported in Section 4.3) we have found that the Bragg resonances at normal incidence are spectrally narrow, with quality factors around 200. In this section, we analyze these long-lived HPhPs corresponding to these resonances, and the ohmic and radiative loss channels.

In our analysis, we will take into account only the first-order Fourier harmonic of the modulated conductivity. We assume that this harmonic plays the dominating role in both the excitation of the first-order polaritonic Bloch modes and their radiative coupling. Thus, the conductivity profile is given by the following relation:

$$\alpha(x) = \alpha_B + \Delta\alpha \cos(Gx), \quad (4.22)$$

so that only the first-order Fourier harmonic $\overline{\alpha}_1 = \Delta\alpha/2$ is different from zero. In Eq. (4.22) $\Delta\alpha$ is the modulation amplitude. For the conductivity profile given by Eq. (4.22), the dispersion relation of the S mode (given by Eq. (4.7)) simplifies to:

$$\mathrm{b}_1 - \Delta\alpha^2 \left(\frac{2}{\mathrm{b}_0} + \frac{1}{\mathrm{b}_2}\right) = 0. \quad (4.23)$$

The imaginary part of the complex root of Eq. (4.23), $\mathrm{Im}(\omega_S)$, represents the inverse lifetime, from which both the radiative and ohmic contributions can be extracted.

Aiming on the qualitative description of the results, we will assume that the dielectric permittivity of the substrate is 1 (so that the conductivity layer is free-standing). This assumption simplifies the writing of equations, but does not affect

the generality of the lifetime dependence upon the lattice parameters. The admittances Y_n appearing in Eq. (4.22) can be explicitly written as $Y_{1,2|0} = 1$; $Y_{1,2|1} \simeq \frac{-i\omega}{Gc}$; $Y_{1,2|2} \simeq \frac{-i\omega}{2Gc}$, where we assume that the reciprocal lattice vector, G, is much larger than the wavevector of light in free space, k_0.

The dispersion relation of polaritons in the unmodulated conductivity layer reads as $b_1 = 0$. This equation simplifies to $\omega_0 = -i\alpha_B(\omega_0) \cdot Gc$ (see Section 4.6.2) and determines the frequency of the bare polaritons in the unmodulated layer, ω_0.

Let us find the explicit expression for the effective normalized conductivity. We take the perpendicular dielectric permittivity of h-BN according to Ref. [145]:

$$\varepsilon_\perp = \varepsilon_{\perp,\infty} + \varepsilon_{\perp,\infty}\left(\frac{\omega_{\perp,LO}^2 - \omega_{\perp,TO}^2}{\omega_{\perp,TO}^2 - \omega^2 - i\gamma_\perp\omega}\right). \quad (4.24)$$

Then, following the procedure developed in Appendix A, the effective normalized conductivity of the layer can be written as

$$\alpha_B(\omega) = A\frac{i\omega}{\omega^2 - \omega_{\perp,TO}^2 + i\gamma_\perp\omega}, \quad (4.25)$$

where $A = \frac{t}{2c}(\omega_{\perp,LO}^2 - \omega_{\perp,TO}^2)\varepsilon_{\perp,\infty}$, with t being the h-BN thickness. In Eq. (4.25) we neglect the frequency-independent term $\varepsilon_{\perp,\infty}$ that appears in eq. (4.24), since the Lorentzian contribution has a large negative value in the region of interest.

Assuming that $\gamma \ll \omega$, the real part of the conductivity (responsible for the ohmic losses) is small compared to the imaginary part, $\mathrm{Re}(\alpha) \ll |\mathrm{Im}(\alpha)|$. Additionally, we assume the modulation amplitude is small, $|\Delta\alpha| < \alpha_B$. Therefore, we can consider the imaginary part of the frequency as a perturbation to $\omega = \omega_0$. Let us take into account both the perturbation due to the ohmic losses and lattice as $\delta\omega$, so that the frequency of the mode S can be written as $\omega_S = \omega_0 - i\delta\omega$. Then we can expand Eq. (4.22) into the Taylor series (considering $\delta\omega$, γ and $\Delta\alpha$ to be the small parameters):

$$-2\frac{i(\omega_0 - i\delta\omega)}{Gc} + 2\alpha|_{\substack{\omega=\omega_0\\ \gamma_\perp=0}} - 2\frac{\partial\alpha}{\partial\omega}\Big|_{\substack{\omega=\omega_0\\ \gamma_\perp=0}} i\delta\omega + 2\frac{\partial\alpha}{\partial\gamma_\perp}\Big|_{\substack{\omega=\omega_0\\ \gamma_\perp=0}} \gamma_\perp - \Delta\alpha^2\left(1 + \frac{iGc}{2\omega_0}\right) = 0, \quad (4.26)$$

where due to small value of α, we have replaced b_0 and b_2 (defined in Eq. 4.9) by $2Y_{1|0}$ and $2Y_{1|2}$, respectively. Taking into account the dispersion relation for the bare polaritons in the unmodulated slab, the correction to the frequency, $\delta\omega$, can be explicitly found from Eq. (4.26):

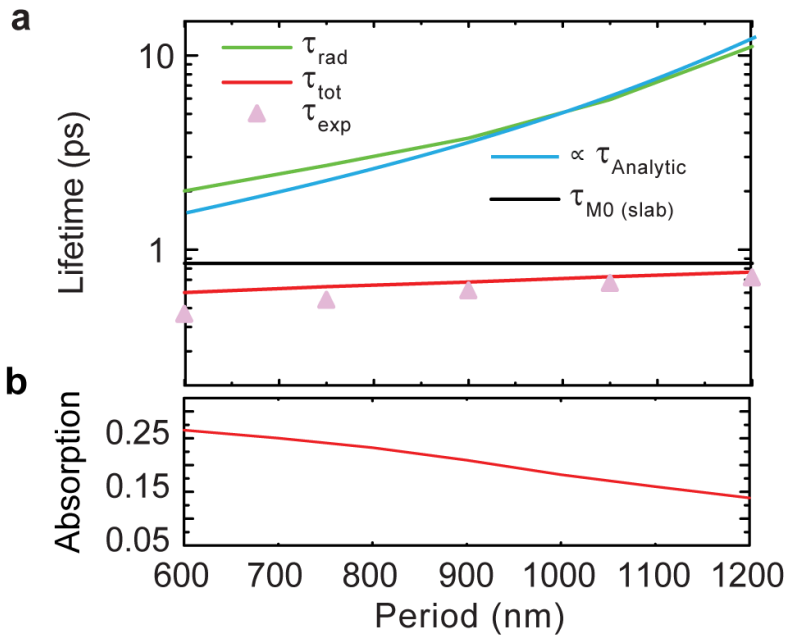

Figure 4.17: Radiative and ohmic lifetimes of the Bloch mode as a function of the period of the polaritonic crystal. **(a)** Total (experimental, triangle symbols, calculated, red line), radiative (calculated, green line; analytical, blue line), and ohmic (black line) lifetime of the polaritonic Bloch mode excited in the hole array as a function of its period. **(b)** Absorption as a function of period, *L*.

$$\delta\omega = -\frac{\Delta\alpha^2\left(1+\frac{iGc}{2\omega_0}\right)-2\frac{\partial\alpha}{\partial\gamma_\perp}\Big|_{\substack{\omega=\omega_0\\ \gamma_\perp=0}}\gamma_\perp}{\frac{2}{Gc}+2i\frac{\partial\alpha}{\partial\omega}\Big|_{\substack{\omega=\omega_0\\ \gamma_\perp=0}}}. \qquad (4.27)$$

This equation can be written in the form of the sum of the two terms: $\delta\omega_0$ (independent upon $\Delta\alpha$) and $\delta\omega_{rad}$ (independent upon $\gamma_\perp$), these being the inverse ohmic and radiative lifetimes, τ_0 and τ_{rad}, respectively:

$$\delta\omega = \delta\omega_0 + \delta\omega_{rad} = \tau_0^{-1} + \tau_{rad}^{-1}. \quad (4.28)$$

Taking the derivatives $\frac{\partial\alpha}{\partial\omega}$ and $\frac{\partial\alpha}{\partial\gamma_\perp}$ from Eq. (4.25), the correction related to the ohmic losses becomes

$$\delta\omega_0 = \tau_0^{-1} = \frac{\gamma_\perp}{2}. \qquad (4.29)$$

The polariton lifetime due to the intrinsic losses in a thin h-BN slab is thus independent upon the film thickness and frequency.

The radiative correction to the resonant frequency is given by (we use the explicit expression for α_B from Eq. (4.25) at $\gamma = 0$ and $\omega = \omega_0$)

$$\delta\omega_{rad} = -\frac{1}{4A} \cdot \Delta\alpha^2 \cdot \frac{(\omega_0^2 - \omega_{TO}^2)^2}{\omega_0^2}. \qquad (4.30)$$

In this expression we do not include the term proportional to $\frac{iGc}{2\omega_0}$ (coming from the denominator of Eq. (4.27)), since the latter contributes to the frequency shift (contributes to the real part of frequency). As we see from Eq. (4.30), the radiative correction to the frequency is proportional to the squared modulation amplitude, $\Delta\alpha^2$. This correction originates from the forward and back-scattering of the 1st diffraction orders (mainly composing the Bloch polariton) via the 0th order field harmonic.

According to Eqs. (4.21), the amplitude of the first Fourier harmonic of the hole array is $\alpha_1 = \frac{\Delta\alpha}{2} = -\alpha_B \frac{a}{L} J_1(2\pi\frac{a}{L})$. Substituting $\Delta\alpha$ into Eq. (4.29) (we use α_B given by Eq. (4.26) at $\gamma = 0$ and $\omega = \omega_0$), we have the following explicit expression for the radiative lifetime, as a function of the parameters of the hole array:

$$\delta\omega_{rad} = \tau_{rad}^{-1} = A \cdot \left(\frac{a}{L}\right)^2 \cdot J_1^2\left(2\pi\frac{a}{L}\right). \qquad (4.31)$$

Notice that in contrast to the ohmic lifetime, the radiation lifetime is thickness-dependent (via the factor $A \propto t$, introduced in Eq. (4.25)).

To corroborate our analytical results, we calculate the total lifetime of the polaritons, τ_{tot}, in the hole array with the help of the full-wave simulations and experimental data. We extract the lifetime from both the simulated and experimental transmission spectra of several hole arrays (with different periods *L*) by fitting them to Lorentzian profiles. The extracted experimental values for τ_{tot} (triangles) are plotted in Fig. 4.17 as a function of period, L, finding a very good agreement with the simulations (red curve). Both red curve and the triangular symbols show a clear dependence upon *L*, deviating from the constant value of the ohmic lifetime, τ_0, (calculated according to Eq. 4.29), traced by the black solid curve. This deviation is due to the finite radiative lifetime, which can be extracted

from the total lifetime as $\tau_{rad}^{-1} = \tau_{tot}^{-1} - \tau_0^{-1}$. In the shown interval in Fig. 4.18) , the radiative lifetime, τ_{rad}, is larger than τ_0 up to one order of magnitude (10 ps vs 1 ps for L= 1200 nm), indicating that the polaritons require significantly more time to couple to the free-space radiation than to be dissipated into the heat.

The result of Eq. (4.31) (corrected by a constant factor) is shown in Figure 4.14 by the blue continuous curve. The tendency provided by Eq. (4.31) finds a good agreement with τ_{rad} extracted from the full-wave simulations (Figure 4.17a, green curve). This agreement indicates that the mechanism of the radiative losses of the polaritonic Bloch mode (excited in the first-order Bragg resonance) is consistent with the scattering of the Bloch mode via the first-order harmonic of the hole array into the diffracted wave of 0th order. As τ_{rad} approaches τ_0 (with decreasing L), the polariton-induced absorption of light by the hole array increases (Figure 4.17b). In fact, the optimal absorption is expected under the general condition of the equality between the radiative and ohmic losses, $\tau_{rad} = \tau_0$, which can be achieved by optimizing the aspect ratio a/L, and the symmetry of the array (e.g. considering the hole arrays of triangular or hexagonal symmetries).

4.10 Conclusions

In summary, we have introduced and experimentally realized IR deeply subwavelength polaritonic crystals based on hyperbolic phonon polaritons in nanostructured van der Waals crystal slabs. Such crystals –being the counterpart of the structured artificial hyperbolic metamaterials (demonstrated at visible frequencies[168])– support highly-confined Bloch modes with flat bands, giving rise to angle- and polarization-independent geometrically-tunable resonances, even in case of the simplest square symmetry. Apart of their potential usage for the subwavelength omnidirectional IR absorbers, couplers and reflectors, h-BN polaritonic crystals can be utilized for inhibiting spontaneous emission (the latter, in contrast, being enhanced/accelerated by h-BN optical antennas[120,157,174]). The suppression of spontaneous emission can be achieved by tuning the parameters of the polaritonic crystal (particularly, its symmetry) to open up the full polaritonic bandgap. From a different perspective, the h-BN hole arrays can be also used as polaritonic hypercrystals (possessing extremely high density of optical states)[175-177], where several HPhP slab modes are simultaneously explored by superimposing several hole arrays with different periods in the same slab. Furthermore, the

combination of h-BN polaritonic crystals/hypercrystals with other low-dimensional materials (such as e.g. h-BN-encapsulated graphene[158]) can open the door to integrable hybrid metamaterials with unique opto-electronic properties on the nanoscale.

A.1 Analytical Approximation of an h-BN thin slab as a 2D conductivity layer

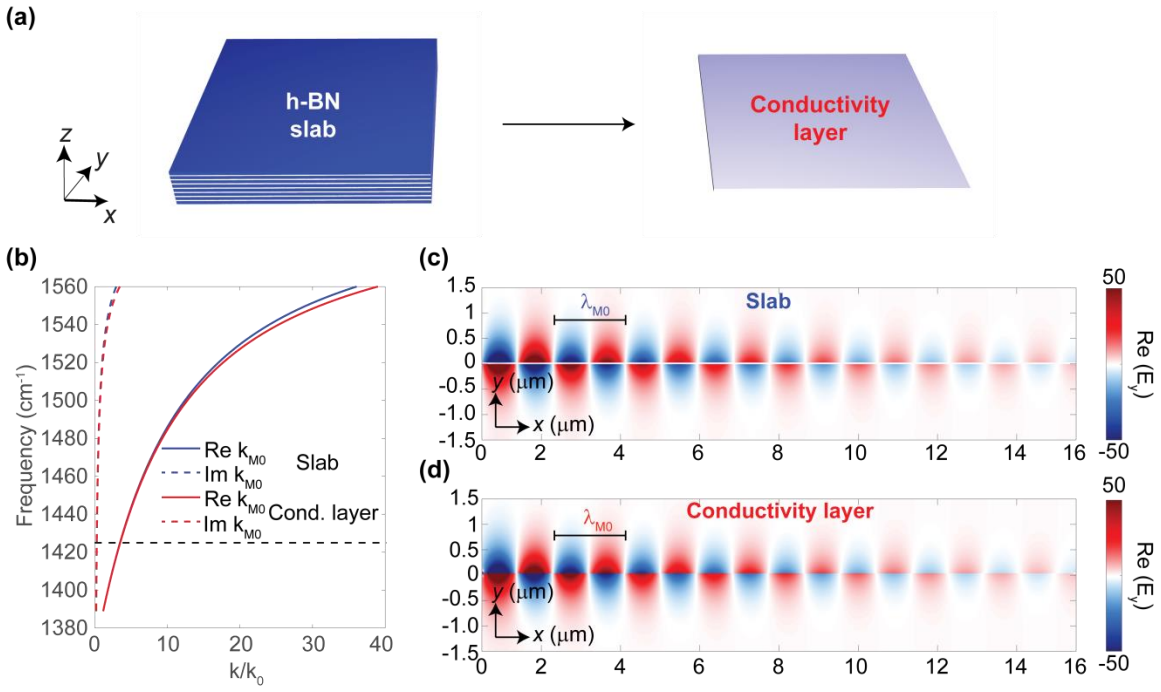

Figure A.1: Dispersion and field distribution of the M0 mode in an h-BN slab and the polaritonic mode in an equivalent conductivity layer. (a) The h-BN flake is approximated as a conductivity layer. **(b)** Wavevector, k, of the M0 mode in a slab of $t = 38$ nm surrounded by air as a function of frequency. Solid blue line renders the real part, while the dashed blue line represents the imaginary part, respectively. Both real and imaginary parts of k are normalized to that of the free space light $k_0 = \frac{\omega}{c}$. **(c)** Simulated vertical component of the electric field, E_z (at $\omega = 1428$ cm^{-1}) of the M0 mode propagating along the x -axis (from left to right). **(d)** The same as in (c), but for the polaritonic mode propagating along the conductivity sheet.

The calculations of the electromagnetic fields in thin films and nanostructures are sometimes simplified if they are modelled as 2D conductivity layers instead of structures with certain thickness. In this appendix, we demonstrate that the M0 mode of a thin layer of h-BN (see Section 2.3) can be well described by modelling the h-BN thin film as a conductivity layer with zero thickness (see Figure A.1a).

A.1 Analytical Approximation of an h-BN thin slab as a 2D conductivity layer

This approximation avoids the calculation of the fields inside the slab, and has been proven valid for in-plane isotropic 2D materials (*e.g.*, graphene[74], silicon carbide[169], and transition layer polaritons[100]) with a layer thickness, t, much smaller than the polariton wavelength ($t \ll \lambda_{M0}$). Using this approximation, the effective conductivity is given by $\sigma_{\text{eff}} = (ct/2i\lambda_0)\epsilon$, where ϵ is the dielectric permittivity of the slab. Analogously, we model the h-BN layer by an isotropic in-plane conducting layer with zero thickness and an effective two-dimensional conductivity $\sigma_{\text{eff}} = (ct/2i\lambda_0)\varepsilon_{\perp}$, neglecting the contribution of the in-plane part of the dielectric permittivity of h-BN, $\varepsilon_{||}$. It is important to note that σ_{eff} scales linearly with t, thus taking into account the effect of the slab thickness.

We justify the validity of our model by Figure A.1, showing an excellent agreement between the dispersions (Figure A.1b), and between the spatial electric field distributions (Figure A.1c,d) of the M0 mode in the h-BN slab (obtained from the quasistatic approximation Eq. 2.18) and a polaritonic mode in the equivalent 2D conductivity layer.

List of Publications

The thesis is mainly based in the following publications:

P. Li, I. Dolado**, F.J. Alfaro-Mozaz**, A.Y. Nikitin, F. Casanova, L.E. Hueso, S. Vélez, R. Hillenbrand, "Optical nanoimaging of hyperbolic surface polaritons at the edges of van der Waals materials"

Nano letters, 17, 1, 228-235 (2016),

Chapter 2

F.J. Alfaro-Mozaz, P. Alonso-González, S. Vélez, I. Dolado, M. Autore, S. Mastel, F. Casanova, L.E. Hueso, P. Li, A. Yu Nikitin, R. Hillenbrand, "Nanoimaging of resonating hyperbolic polaritons in linear boron nitride antennas"

Nature Communications, 9, 15624 (2017)

Chapter 3

FJ Alfaro-Mozaz, S. G. Rodrigo, P. Alonso-González, S. Vélez, I. Dolado, F. Casanova, L. E. Hueso, L. Martín-Moreno, R. Hillenbrand, A. Y. Nikitin, "Deeply subwavelength phonon-polaritonic crystal made of a van der Waals material"

Nature Communications, 10, 1, 42 (2019)

Chapter 4

Other Publications

M. Autore, P. Li, I. Dolado, **F.J. Alfaro-Mozaz**, R. Esteban, A. Atxabal, F. Casanova, L. E. Hueso, P. Alonso-González, J. Aizpurúa, A. Y. Nikitin, S. Vélez, R. Hillenbrand, "Boron nitride nanoresonators for phonon-enhanced molecular vibrational spectroscopy at the strong coupling limit"

Light: Science & Applications, 7, 4, 17172 (2018)

P. Li, I. Dolado, **F.J. Alfaro-Mozaz**, F. Casanova, L. E. Hueso, S. Liu, J. H. Edgar, A. Y. Nikitin, S. Vélez, R. Hillenbrand, "Infrared hyperbolic metasurface based on nanostructured van der Waals materials"

Science, 359, 6378, 892-896 (2018)

P. Pons-Valencia*, **F.J. Alfaro-Mozaz***, M.M. Wiecha, V. Biolek, I. Dolado, S. Vélez, P. Li, P. Alonso-González, F. Casanova, L.E. Hueso, L. Martín-Moreno, R. Hillenbrand, A.Y. Nikitin, "Launching of hyperbolic phonon-polaritons in h-BN slabs by resonant metal plasmonic antennas"

Nature Communications, 10, 324 (2019)

*Equally contributed

I. Dolado, **F.J. Alfaro-Mozaz**, P. Li, E. Nikulina, A. Bylinkin, S. Liu, J. H. Edgar, F. Casanova, L.E. Hueso, P. Alonso-González, S. Vélez, A.Y. Nikitin, R. Hillenbrand "Nanoscale guiding of infrared light with hyperbolic volume and surface polaritons in van der Waals material ribbons"

Advanced Materials, 1906530 (2020)

Acknowledgements

I would like to express my deepest gratitude to both my supervisors, Alexey Nikitin and Rainer Hillenbrand. Their patient and careful guidance has been fundamental during my years as PhD student. I consider myself very fortunate learning from them, from both a theoretical and experimental point of view. I owe a huge thank to Prof. Pablo Alonso, my former Master's thesis supervisor. His passion about nanooptics surely was contagious!

I am thankful to many research colleagues of the Nanooptics group. Especially to Irene Dolado and Peining Li, with whom I shared many inspiring and insightful discussions. I would like to send my special thanks to Sergio Gutierrez Rodrigo, Pablo Pons and Luis Martin Moreno. It has been a pleasure to collaborate with them.

My special thanks to many people, Maura, Maite, Pepe, Ana, Marta, among many others. To Bárbara, thanks for sharing with me the best part of these years. To my parents, for their unconditional support and love, to which I am hugely indebt.

Bibliography

1. Barnes, W.L., Dereux, A. & Ebbesen, T.W. Surface plasmon subwavelength optics. *Nature* **424**, 824-830 (2003).
2. Hartstein, A., Kirtley, J.R. & Tsang, J.C. Enhancement of the Infrared Absorption from Molecular Monolayers with Thin Metal Overlayers. *Physical Review Letters* **45**, 201-204 (1980).
3. Aroca, R. *Surface-Enhanced Vibrational Spectroscopy*, (Wiley and Sons, 2006).
4. Hertzog, M., Wang, M., Mony, J. & Börjesson, K. Strong light–matter interactions: a new direction within chemistry. *Chemical Society Reviews* **48**, 937-961 (2019).
5. Senior, J.M. *Optical Fiber Communications, Principles and Practice*, (Pearson Education Limited, 2009).
6. Malitson, I.H. Interspecimen Comparison of the Refractive Index of Fused Silica*,†. *Journal of the Optical Society of America* **55**, 1205-1209 (1965).
7. Jackson, J.D. *Classical Electrodynamics*, (Wiley, 1975).
8. Marcuse, D. *Theory of Dielectric Optical Waveguides*, (Academic Press, 1974).
9. Balanis, C. *Advanced Engineering Electromagnetics*, (John Wiley & Sons, Inc, 1989).
10. Landau, L.D. & Lifshitz, E.M. *Electrodynamics of Continuous Media*, (Pergamon Press, 1960).
11. Gramotnev, D.K. & Bozhevolnyi, S.I. Plasmonics beyond the diffraction limit. *Nature Photonics* **4**, 83 (2010).
12. Palik, E. *Handbook of Optical Constants of Solids*, (1997).
13. Novotny, L. & Hecht., B. *Principles of Nano-Optics*, (Cambridge University Press, 2012).
14. Thèye, M.-L. Investigation of the Optical Properties of Au by Means of Thin Semitransparent Films. *Physical Review B* **2**, 3060-3078 (1970).
15. Olmon, R.L. et al. Optical dielectric function of gold. *Physical Review B* **86**, 235147 (2012).
16. Maier, S.A. *Plasmonics: Fundamentals and Applications*, (2007).
17. Born, M. & Wolf, E. *Principles of Optics*, (2002).
18. McPeak, K.M. et al. Plasmonic Films Can Easily Be Better: Rules and Recipes. *ACS Photonics* **2**, 326-333 (2015).
19. Adato, R. & Guo, J. Characteristics of ultra-long range surface plasmon waves at optical frequencies. *Optics Express* **15**, 5008-5017 (2007).

20. Dionne, J.A., Sweatlock, L.A., Atwater, H.A. & Polman, A. Planar metal plasmon waveguides: frequency-dependent dispersion, propagation, localization, and loss beyond the free electron model. *Physical Review B* **72**, 075405 (2005).

21. Berini, P. Long-range surface plasmon polaritons. *Advances in Optics and Photonics* **1**, 484-588 (2009).

22. Degiron, A. & Smith, D.R. Numerical simulations of long-range plasmons. *Optics Express* **14**, 1611-1625 (2006).

23. Agrawal, G.P. *Fiber-Optic Communication Systems*, (2010).

24. Liu, X., Wang, L. & Zhang, Z.M. Near-Field Thermal Radiation: Recent Progress and Outlook. *Nanoscale and Microscale Thermophysical Engineering* **19**, 98-126 (2015).

25. Law, S., Podolskiy, V. & Wasserman, D. Towards nano-scale photonics with micro-scale photons: the opportunities and challenges of mid-infrared plasmonics. in *Nanophotonics* Vol. 2 103 (2013).

26. Sai, H. & Kanamori, Y. SPECTRALLY SELECTIVE THERMAL RADIATORS AND ABSORBERS WITH PERIODIC MICROSTRUCTURED SURFACE FOR HIGH-TEMPERATURE APPLICATIONS. *Microscale Thermophysical Engineering* **7**, 101-115 (2003).

27. Hendrickson, J., Guo, J., Zhang, B., Buchwald, W. & Soref, R. Wideband perfect light absorber at midwave infrared using multiplexed metal structures. *Optics Letters* **37**, 371-373 (2012).

28. Zhong, Y., Malagari, S.D., Hamilton, T. & Wasserman, D.M. Review of mid-infrared plasmonic materials. Vol. 9 21 (SPIE, 2015).

29. Salihoglu, O. et al. Graphene-Based Adaptive Thermal Camouflage. *Nano Letters* **18**, 4541-4548 (2018).

30. Greffet, J.-J. et al. Coherent emission of light by thermal sources. *Nature* **416**, 61-64 (2002).

31. Mason, J.A. et al. Strong absorption and selective thermal emission from a midinfrared metamaterial. *Applied Physics Letters* **98**, 241105 (2011).

32. Saxler, J. et al. Time-domain measurements of surface plasmon polaritons in the terahertz frequency range. *Physical Review B* **69**, 155427 (2004).

33. Dionne, J.A., Sweatlock, L.A., Atwater, H.A. & Polman, A. Plasmon slot waveguides: Towards chip-scale propagation with subwavelength-scale localization. *Physical Review B* **73**, 035407 (2006).

34. Kusunoki, F., Yotsuya, T., Takahara, J. & Kobayashi, T. Propagation properties of guided waves in index-guided two-dimensional optical waveguides. *Applied Physics Letters* **86**, 211101 (2005).

35. Economou, E.N. Surface Plasmons in Thin Films. *Physical Review* **182**, 539-554 (1969).

36. Zia, R., Selker, M.D., Catrysse, P.B. & Brongersma, M.L. Geometries and materials for subwavelength surface plasmon modes. *Journal of the Optical Society of America A* **21**, 2442-2446 (2004).

37. Sarriugarte, P. et al. Propagation and nanofocusing of infrared surface plasmons on tapered transmission lines: Influence of the substrate. *Optics Communications* **285**, 3378-3382 (2012).

38. Schnell M. et al. Nanofocusing of mid-infrared energy with tapered transmission lines. *Nat Photon* **5**, 283-287 (2011).

39. Schwarz, B. et al. Monolithically integrated mid-infrared lab-on-a-chip using plasmonics and quantum cascade structures. *Nature Communications* **5**, 4085 (2014).

40. Taliercio, T. & Biagioni, P. Semiconductor infrared plasmonics. in *Nanophotonics* Vol. 8 949 (2019).

41. Prucnal, S. et al. Ultra-doped n-type germanium thin films for sensing in the mid-infrared. *Scientific Reports* **6**, 27643 (2016).

42. Soref, R., Peale, R.E. & Buchwald, W. Longwave plasmonics on doped silicon and silicides. *Optics Express* **16**, 6507-6514 (2008).

43. Khurgin Jacob, B. Relative merits of phononics vs. plasmonics: the energy balance approach. in *Nanophotonics* Vol. 7 305 (2018).

44. Frigerio, J. et al. Tunability of the dielectric function of heavily doped germanium thin films for mid-infrared plasmonics. *Physical Review B* **94**, 085202 (2016).

45. West, P.R. et al. Searching for better plasmonic materials. *Laser & Photonics Reviews* **4**, 795-808 (2010).

46. Boltasseva, A. & Atwater, H.A. Low-Loss Plasmonic Metamaterials. *Science* **331**, 290-291 (2011).

47. Caldwell Joshua, D. et al. Low-loss, infrared and terahertz nanophotonics using surface phonon polaritons. **4**, 44 (2015).

48. Hillenbrand, R., Taubner, T. & Keilmann, F. Phonon-enhanced light-matter interaction at the nanometre scale. *Nature* **418**, 159-162 (2002).

49. Evans, D.J., Ushioda, S. & McMullen, J.D. Raman Scattering from Surface Polaritons in a GaAs Film. *Physical Review Letters* **31**, 369-372 (1973).

50. Kischkat, J. et al. Mid-infrared optical properties of thin films of aluminum oxide, titanium dioxide, silicon dioxide, aluminum nitride, and silicon nitride. *Applied Optics* **51**, 6789-6798 (2012).

51. Stroscio, M.A. & Dutta, M. *Phonons in nanostructures*, (2001).

52. Ashcroft, N.W. & Mermin, N.D. *Solid state physics*, xxi, 826 p. (Holt, New York,, 1976).

53. Bohren, C.F. & Huffman, D.R. *Absorption and Scattering of Light by Small Particles*, 331 (2004).

54. Wang, T. et al. Phonon-Polaritonic Bowtie Nanoantennas: Controlling Infrared Thermal Radiation at the Nanoscale. *ACS Photonics* **4**, 1753-1760 (2017).

55. Zollner, S. et al. Dielectric functions of bulk 4H and 6H SiC and spectroscopic ellipsometry studies of thin SiC films on Si. *Journal of Applied Physics* **85**, 8353-8361 (1999).

56. Caldwell, J.D. et al. Low-Loss, Extreme Subdiffraction Photon Confinement via Silicon Carbide Localized Surface Phonon Polariton Resonators. *Nano Letters* **13**, 3690-3697 (2013).

57. Basov, D.N., Fogler, M.M. & García de Abajo, F.J. Polaritons in van der Waals materials. *Science* **354**(2016).

58. Novoselov, K.S. et al. Electric Field Effect in Atomically Thin Carbon Films. *Science* **306**, 666-669 (2004).

59. Jones, A.M. et al. Spin–layer locking effects in optical orientation of exciton spin in bilayer WSe2. *Nature Physics* **10**, 130-134 (2014).

60. Xia, F., Wang, H. & Jia, Y. Rediscovering black phosphorus as an anisotropic layered material for optoelectronics and electronics. *Nature Communications* **5**, 4458 (2014).

61. Mak, K.F., Lee, C., Hone, J., Shan, J. & Heinz, T.F. Atomically Thin MoS2: A New Direct-Gap Semiconductor. *Phys. Rev. Lett.* **105**, 136805 (2010).

62. Geim, A.K. & Grigorieva, I.V. Van der Waals heterostructures. *Nature* **499**, 419-425 (2013).

63. Duong, D.L., Yun, S.J. & Lee, Y.H. van der Waals Layered Materials: Opportunities and Challenges. *ACS Nano* **11**, 11803-11830 (2017).

64. Novoselov, K.S. et al. Two-Dimensional Atomic Crystals. *Proc. Natl. Acad. Sci. U. S. A.* **102**, 10451 (2005).

65. Castro Neto, A.H., Guinea, F., Peres, N.M.R., Novoselov, K.S. & Geim, A.K. The electronic properties of graphene. *Reviews of Modern Physics* **81**, 109-162 (2009).

66. Morozov, S.V. et al. Giant Intrinsic Carrier Mobilities in Graphene and Its Bilayer. *Physical Review Letters* **100**, 016602 (2008).

67. Geim, A.K. Graphene: Status and Prospects. *Science* **324**, 1530-1534 (2009).

68. Wunsch, B., Stauber, T., Sols, F. & Guinea, F. Dynamical polarization of graphene at finite doping. *New Journal of Physics* **8**, 318-318 (2006).

69. Hwang, E.H. & Das Sarma, S. Dielectric function, screening, and plasmons in two-dimensional graphene. *Physical Review B* **75**, 205418 (2007).

70. Nikitin, A.Y. et al. Real-space mapping of tailored sheet and edge plasmons in graphene nanoresonators. *Nat Photon* **10**, 239-243 (2016).

71. Chen, J. et al. Optical nano-imaging of gate-tunable graphene plasmons. *Nature* **487**, 77-81 (2012).

72. Fei, Z. et al. Gate-tuning of graphene plasmons revealed by infrared nano-imaging. *Nature* **487**, 82-85 (2012).

73. García de Abajo, F.J. Graphene Plasmonics: Challenges and Opportunities. *ACS Photonics* **1**, 135-152 (2014).

74. Nikitin, A.Y. Graphene Plasmonics. in *World Scientific Handbook of Metamaterials and Plasmonics* Vol. 4: Recent Progress in the Field of Nanoplasmonics (ed. Aizpurua, J.) (World Scientific, 2017).

75. Caldwell, J.D. et al. Photonics with hexagonal boron nitride. *Nature Reviews Materials* **4**, 552-567 (2019).

76. Kildishev, A.V., Boltasseva, A. & Shalaev, V.M. Planar Photonics with Metasurfaces. *Science* **339**, 1232009 (2013).

77. Woessner, A. et al. Highly confined low-loss plasmons in graphene–boron nitride heterostructures. *Nature Materials* **14**, 421 (2014).

78. Rodrigo, D. et al. Mid-infrared plasmonic biosensing with graphene. *Science* **349**, 165-168 (2015).

79. Liu, M. et al. A graphene-based broadband optical modulator. *Nature* **474**, 64 (2011).

80. Dai, S. et al. Tunable Phonon Polaritons in Atomically Thin van der Waals Crystals of Boron Nitride. *Science* **343**, 1125-1129 (2014).

81. Wang, Q.H., Kalantar-Zadeh, K., Kis, A., Coleman, J.N. & Strano, M.S. Electronics and optoelectronics of two-dimensional transition metal dichalcogenides. *Nature Nanotechnology* **7**, 699 (2012).

82. Chhowalla, M. et al. The Chemistry of Two-Dimensional Layered Transition Metal Dichalcogenide Nanosheets. *Nat. Chem.* **5**, 263 (2013).

83. van Veen, E. et al. Tuning Two-Dimensional Hyperbolic Plasmons in Black Phosphorus. *Physical Review Applied* **12**, 014011 (2019).

84. Low, T. et al. Plasmons and Screening in Monolayer and Multilayer Black Phosphorus. *Physical Review Letters* **113**, 106802 (2014).

85. Geick, R., Perry, C.H. & Rupprecht, G. Normal Modes in Hexagonal Boron Nitride. *Physical Review* **146**, 543-547 (1966).

86. Zheng, Z. et al. A mid-infrared biaxial hyperbolic van der Waals crystal. *Science Advances* **5**, eaav8690 (2019).

87. Ma, W. et al. In-plane anisotropic and ultra-low-loss polaritons in a natural van der Waals crystal. *Nature* **562**, 557-562 (2018).

88. Ramasubramaniam, A. Large excitonic effects in monolayers of molybdenum and tungsten dichalcogenides. *Physical Review B* **86**, 115409 (2012).

89. Tsiatmas, A., Fedotov, V.A., García de Abajo, F.J. & Zheludev, N.I. Low-loss terahertz superconducting plasmonics. *New Journal of Physics* **14**, 115006 (2012).

90. Hartstein, A., Burstein, E., Maradudin, A.A., Brewer, R. & Wallis, R.F. Surface polaritons on semi-infinite gyromagnetic media. *Journal of Physics C: Solid State Physics* **6**, 1266-1276 (1973).

91. Gjerding, M.N., Petersen, R., Pedersen, T.G., Mortensen, N.A. & Thygesen, K.S. Layered van der Waals crystals with hyperbolic light dispersion. *Nature Communications* **8**, 320 (2017).

92. Narimanov, E.E. & Kildishev, A.V. Naturally hyperbolic. *Nature Photonics* **9**, 214 (2015).

93. Hu, D. et al. Probing optical anisotropy of nanometer-thin van der waals microcrystals by near-field imaging. *Nature Communications* **8**, 1471 (2017).

94. Oxtoby, D.W., Pat Gillis, H. & Nachtrieb, N.H. *Principles of Modern Chemistry*, 876 (1998).

95. Li, K. & Xue, D. Estimation of Electronegativity Values of Elements in Different Valence States. *The Journal of Physical Chemistry A* **110**, 11332-11337 (2006).

96. Mohr, M. et al. Phonon dispersion of graphite by inelastic x-ray scattering. *Physical Review B* **76**, 035439 (2007).

97. Alfaro-Mozaz, F.J. et al. Nanoimaging of resonating hyperbolic polaritons in linear boron nitride antennas. *Nature Communications* **8**, 15624 (2017).

98. Poddubny, A., Iorsh, I., Belov, P. & Kivshar, Y. Hyperbolic metamaterials. *Nat Photon* **7**, 948-957 (2013).

99. Bharadwaj, P., Deutsch, B. & Novotny, L. Optical Antennas. *Advances in Optics and Photonics* **1**, 438-483 (2009).

100. Novotny, L. & Stranick, S.J. NEAR-FIELD OPTICAL MICROSCOPY AND SPECTROSCOPY WITH POINTED PROBES. *Annual Review of Physical Chemistry* **57**, 303-331 (2006).

101. Curto, A.G. et al. Unidirectional Emission of a Quantum Dot Coupled to a Nanoantenna. *Science* **329**, 930-933 (2010).

102. Chong, Y.D., Ge, L., Cao, H. & Stone, A.D. Coherent Perfect Absorbers: Time-Reversed Lasers. *Physical Review Letters* **105**, 053901 (2010).

103. Zhang, X., Chen, Y.L., Liu, R.-S. & Tsai, D.P. Plasmonic photocatalysis. *Reports on Progress in Physics* **76**, 046401 (2013).

104. Novotny, L. & van Hulst, N. Antennas for light. *Nature Photonics* **5**, 83 (2011).

105. Aizpurua, J. et al. Optical properties of coupled metallic nanorods for field-enhanced spectroscopy. *Physical Review B* **71**, 235420 (2005).

106. Schnell, M. et al. Controlling the near-field oscillations of loaded plasmonic nanoantennas. *Nature Photonics* **3**, 287-291 (2009).

107. Neubrech, F. et al. Resonant Plasmonic and Vibrational Coupling in a Tailored Nanoantenna for Infrared Detection. *Physical Review Letters* **101**, 157403 (2008).

108. Taminiau, T.H., Stefani, F.D. & van Hulst, N.F. Optical Nanorod Antennas Modeled as Cavities for Dipolar Emitters: Evolution of Sub- and Super-Radiant Modes. *Nano Letters* **11**, 1020-1024 (2011).

109. Curto, A.G. et al. Multipolar radiation of quantum emitters with nanowire optical antennas. *Nature Communications* **4**, 1750 (2013).

110. Dorfmüller, J. et al. Fabry-Pérot Resonances in One-Dimensional Plasmonic Nanostructures. *Nano Letters* **9**, 2372-2377 (2009).

111. Park, K., Biswas, S., Kanel, S., Nepal, D. & Vaia, R.A. Engineering the Optical Properties of Gold Nanorods: Independent Tuning of Surface Plasmon Energy, Extinction Coefficient, and Scattering Cross Section. *The Journal of Physical Chemistry C* **118**, 5918-5926 (2014).

112. Aizpurua, J. et al. Optical Properties of Gold Nanorings. *Physical Review Letters* **90**, 057401 (2003).

113. Neubrech, F. et al. Resonances of individual metal nanowires in the infrared. *Applied Physics Letters* **89**, 253104 (2006).

114. Joannopoulos, J.D., Johnson, S.G., Winn, J.N. & Meade, R.D. *Photonic Crystals: Molding the Flow of Light*, 304 (Princeton University Press, 2008).

115. Noda, S., Tomoda, K., Yamamoto, N. & Chutinan, A. Full Three-Dimensional Photonic Bandgap Crystals at Near-Infrared Wavelengths. *Science* **289**, 604-606 (2000).

116. Slipchenko, T.M., Nesterov, M.L., Martin-Moreno, L. & Nikitin, A.Y. Analytical solution for the diffraction of an electromagnetic wave by a graphene grating. *Journal of Optics* **15**, 114008 (2013).

117. Garcia-Vidal, F.J., Martin-Moreno, L., Ebbesen, T.W. & Kuipers, L. Light passing through subwavelength apertures. *Reviews of Modern Physics* **82**, 729-787 (2010).

118. Kats, A.V., Nesterov, M.L. & Nikitin, A.Y. Excitation of surface plasmon-polaritons in metal films with double periodic modulation: Anomalous optical effects. *Physical Review B* **76**, 045413 (2007).

119. García de Abajo, F.J. Colloquium: Light scattering by particle and hole arrays. *Reviews of Modern Physics* **79**, 1267-1290 (2007).

120. Feng, L., Lu, M.-H., Lomakin, V. & Fainman, Y. Plasmonic photonic crystal with a complete band gap for surface plasmon polariton waves. *Applied Physics Letters* **93**, 231105 (2008).

121. Newman, W.D. et al. Observation of long-range dipole-dipole interactions in hyperbolic metamaterials. *Science Advances* **4**, eaar5278 (2018).

122. Maier, M., Nemilentsau, A., Low, T. & Luskin, M. Ultracompact Amplitude Modulator by Coupling Hyperbolic Polaritons over a Graphene-Covered Gap. *ACS Photonics* **5**, 544-551 (2018).

123. Dai, S. et al. Subdiffractional focusing and guiding of polaritonic rays in a natural hyperbolic material. *Nat Commun* **6**(2015).

124. Caldwell, J.D. & Novoselov, K.S. Van der Waals heterostructures: Mid-infrared nanophotonics. *Nat Mater* **14**, 364-366 (2015).

125. Álvarez-Pérez, G., Voronin, K., Volkov, V., Alonso-González, P. & Nikitin, A.Y. Analytical analysis of the electromagnetic modes in slabs of biaxial crystals. *ArXiv e-prints* (2019).

126. Narimanov, E.E. Dyakonov waves in biaxial anisotropic crystals. *Physical Review A* **98**, 013818 (2018).

127. Yoxall, E. et al. Direct observation of ultraslow hyperbolic polariton propagation with negative phase velocity. *Nat Photon* **9**, 674-678 (2015).

128. Keilmann, F. & Hillenbrand, R. Near-field microscopy by elastic light scattering from a tip. *Philosophical Transactions of the Royal Society of London. series A:* **362**, 787-805 (2004).

129. Pons-Valencia, P. et al. Launching of hyperbolic phonon-polaritons in h-BN slabs by resonant metal plasmonic antennas. *Nature Communications* **10**, 3242 (2019).

130. Gilburd, L. et al. Hexagonal Boron Nitride Self-Launches Hyperbolic Phonon Polaritons. *The Journal of Physical Chemistry Letters* **8**, 2158-2162 (2017).

131. Nikitin, A.Y. et al. Nanofocusing of Hyperbolic Phonon Polaritons in a Tapered Boron Nitride Slab. *ACS Photonics* **3**, 924-929 (2016).

132. Giles, A.J. et al. Ultralow-loss polaritons in isotopically pure boron nitride. *Nature Materials* **17**, 134 (2017).

133. D'yakonov:, M.I. New type of electromagnetic wave propagating at an interface,. *Sov. Phys. JETP* **67**, 714-716 (1988).

134. Takayama, O., Artigas, D. & Torner, L. Lossless directional guiding of light in dielectric nanosheets using Dyakonov surface waves. *Nat Nano* **9**, 419-424 (2014).

135. Cojocaru, E. Comparative analysis of Dyakonov hybrid surface waves at dielectric/elliptic and dielectric/hyperbolic media interfaces. *Journal of the Optical Society of America B* **31**, 2558-2564 (2014).

136. Gomez-Diaz, J.S. & Alù, A. Flatland Optics with Hyperbolic Metasurfaces. *ACS Photonics* **3**, 2211-2224 (2016).

137. Li, P. et al. Optical Nanoimaging of Hyperbolic Surface Polaritons at the Edges of van der Waals Materials. *Nano Letters* **17**, 228-235 (2017).

138. Li, P. et al. Infrared hyperbolic metasurface based on nanostructured van der Waals materials. *Science* **359**, 892-896 (2018).

139. Huber, A.J., Keilmann, F., Wittborn, J., Aizpurua, J. & Hillenbrand, R. Terahertz Near-Field Nanoscopy of Mobile Carriers in Single Semiconductor Nanodevices. *Nano Letters* **8**, 3766-3770 (2008).

140. Agranovich, V.M. & Mills, D.L. *Surface Polaritons: Electromagnetic Waves at Surfaces and Interfaces*, (1982).

141. Schuller, J.A. et al. Plasmonics for extreme light concentration and manipulation. *Nat Mater* **9**, 193-204 (2010).

142. Li, P. et al. Reversible optical switching of highly confined phonon-polaritons with an ultrathin phase-change material. *Nat Mater* **15**, 870-875 (2016).

143. Jacob, Z. Nanophotonics: Hyperbolic phonon-polaritons. *Nat Mater* **13**, 1081-1083 (2014).

144. Xu, X.G. et al. One-dimensional surface phonon polaritons in boron nitride nanotubes. *Nat Commun* **5**(2014).

145. Caldwell, J.D. et al. Sub-diffractional volume-confined polaritons in the natural hyperbolic material hexagonal boron nitride. *Nat Commun* **5**(2014).

146. Khurgin, J.B. & Sun, G. Scaling of losses with size and wavelength in nanoplasmonics and metamaterials. *Applied Physics Letters* **99**, 211106 (2011).

147. He, Y., He, S., Gao, J. & Yang, X. Nanoscale metamaterial optical waveguides with ultrahigh refractive indices. *Journal of the Optical Society of America B* **29**, 2559-2566 (2012).

148. Yang, X., Yao, J., Rho, J., Yin, X. & Zhang, X. Experimental realization of three-dimensional indefinite cavities at the nanoscale with anomalous scaling laws. *Nat Photon* **6**, 450-454 (2012).

149. Giles, A.J. et al. Imaging of Anomalous Internal Reflections of Hyperbolic Phonon-Polaritons in Hexagonal Boron Nitride. *Nano Letters* **16**, 3858-3865 (2016).

150. Noda, S., Fujita, M. & Asano, T. Spontaneous-emission control by photonic crystals and nanocavities. *Nature Photonics* **1**, 449 (2007).

151. Joannopoulos, J.D., Villeneuve, P.R. & Fan, S. Photonic crystals: putting a new twist on light. *Nature* **386**, 143 (1997).

152. Zou, Y., Chakravarty, S., Chung, C.-J., Xu, X. & Chen, R.T. Mid-infrared silicon photonic waveguides and devices [Invited]. *Photonics Research* **6**, 254-276 (2018).

153. Christoph, F., Thomas, H. & S., W.O. Photonic Crystals for Chemical Sensing and Biosensing. *Angewandte Chemie International Edition* **53**, 3318-3335 (2014).

154. Lochbaum, A. et al. On-Chip Narrowband Thermal Emitter for Mid-IR Optical Gas Sensing. *ACS Photonics* **4**, 1371-1380 (2017).

155. Weng, B., Qiu, J. & Shi, Z. Continuous-wave mid-infrared photonic crystal light emitters at room temperature. *Applied Physics B* **123**, 29 (2016).

156. Wasserman, D., Shaner, E.A. & Cederberg, J.G. Midinfrared doping-tunable extraordinary transmission from sub-wavelength Gratings. *Applied Physics Letters* **90**, 191102 (2007).

157. Kalchmair, S. et al. Photonic crystal slab quantum well infrared photodetector. *Applied Physics Letters* **98**, 011105 (2011).

158. Lundeberg, Mark B. et al. Thermoelectric detection and imaging of propagating graphene plasmons. *Nature Materials* **16**, 204 (2016).

159. D'apuzzo, F. et al. Mid-Infrared Plasmonic Excitation in Indium Tin Oxide Microhole Arrays. *ACS Photonics* **5**, 2431-2436 (2018).

160. Autore, M. et al. Boron nitride nanoresonators for phonon-enhanced molecular vibrational spectroscopy at the strong coupling limit. *Light: Science &Amp; Applications* **7**, 17172 (2018).

161. Kim, S. et al. Photonic crystal cavities from hexagonal boron nitride. *Nature Communications* **9**, 2623 (2018).

162. Yablonovitch, E. Inhibited Spontaneous Emission in Solid-State Physics and Electronics. *Physical Review Letters* **58**, 2059-2062 (1987).

163. Andres, C.-G. et al. Deterministic transfer of two-dimensional materials by all-dry viscoelastic stamping. *2D Materials* **1**, 011002 (2014).

164. Alonso-González, P. et al. *Science* **344**, 1369 (2014).

165. Ocelic, N., Huber, A. & Hillenbrand, R. Pseudoheterodyne detection for background-free near-field spectroscopy. *Applied Physics Letters* **89**, 101124 (2006).

166. Tsakmakidis, K.L., Hess, O., Boyd, R.W. & Zhang, X. Ultraslow waves on the nanoscale. *Science* **358**(2017).

167. Baba, T. Slow light in photonic crystals. *Nature Photonics* **2**, 465 (2008).

168. Wayne, D. et al. Hyperbolic Polaritonic Crystals Based on Nanostructured Nanorod Metamaterials. *Advanced Materials* **27**, 5974-5980 (2015).

169. Nikitin, A.Y., Alonso-González, P. & Hillenbrand, R. Efficient Coupling of Light to Graphene Plasmons by Compressing Surface Polaritons with Tapered Bulk Materials. *Nano Letters* **14**, 2896-2901 (2014).